N-63-4-6

TR-1103

THE STAGNATION-POINT LANGMUIR PROBE IN A SHOCK TUBE -- THEORY AND MEASUREMENTS

Irvin Pollin

28 June 1963

HARRY DIAMOND LABORATORIES
FORMERLY: DIAMOND ORDNANCE FUZE LABORATORIES
ARMY MATERIEL COMMAND
WASHINGTON 25, D.C.

HARRY DIAMOND LABORATORIES

Robert W. McEvoy
LtCol, Ord Corps
Commanding

B. M. Horton
Technical Director

MISSION

The mission of the Harry Diamond Laboratories is:

(1) To perform research and engineering on systems for detecting, locating, and evaluating targets; for accomplishing safing, arming, and munition control functions; and for providing initiation signals: these systems include, but are not limited to, radio and non-radio proximity fuzes, predictor-computer fuzes, electronic timers, electrically-initiated fuzes, and related items.

(2) To perform research and engineering in fluid amplification and fluid-actuated control systems.

(3) To perform research and engineering in instrumentation and measurement in support of the above.

(4) To perform research and engineering in order to achieve maximum immunity of systems to adverse influences, including countermeasures, nuclear radiation, battlefield conditions, and high-altitude and space environments.

(5) To perform research and engineering on materials, components, and subsystems in support of above.

(6) To conduct basic research in the physical sciences in support of the above.

(7) To provide consultative services to other Government agencies when requested.

(8) To carry out special projects lying within installation competence upon approval by the Director of Research and Development, Army Materiel Command.

(9) To maintain a high degree of competence in the application of the physical sciences to the solution of military problems.

UNITED STATES ARMY MATERIEL COMMAND
HARRY DIAMOND LABORATORIES
WASHINGTON 25, D.C.

AMCMS Code 5900.21.83021
HDL Proj 23800 28 June 1963

TR-1103

THE STAGNATION-POINT LANGMUIR PROBE IN A SHOCK TUBE— THEORY AND MEASUREMENTS

Irvin Pollin

FOR THE COMMANDER:
Approved by

H. Sommer
Chief, Laboratory 200

Thesis submitted to the Faculty of the Graduate School of the University of Maryland in partial fulfillment of the requirements for the degree of Doctor of Philosophy
1963

QUALIFIED REQUESTERS MAY OBTAIN COPIES OF THIS REPORT FROM

DEFENSE DOCUMENTATION CENTER

5010 Duke Street
Alexandria, Virginia

PREFACE

Our primary objective is to determine the space charge distribution surrounding a high-speed vehicle at high altitudes following an atomic burst. To date, this problem remains unsolved. Indeed, no procedure, theoretical or experimental, is available for the simpler problem of flight not involving an atomic burst. Although references 1, 2, and 3 describe an instrument to measure the undisturbed free stream ionization for argon gas in a low-density supersonic plasma jet stream, the assumptions of this theory do not appear valid for our use in air.

To begin a solution of the above problem, we decided to analyze in exact detail a much simpler problem--one from which we could begin to build a theory and readily confirm experimentally as we proceeded. Such a problem is presented in this report. Here, we show a theoretical procedure for solving the ion-electron distribution in the stagnation-point boundary layer of a blunt body and confirm this procedure with measurements in a shock tube. This problem is solved exactly with the use of electronic computers by simultaneously solving the gasdynamic and electric field equations.

The neutral gas equations for a dissociated gas cannot be solved in a general way. At best, solutions can be obtained for the stagnation region of a blunt body behind the detached shock and for conical and flat plate bodies. This limits the type of body shapes for which we can expect to obtain solutions. In addition, we will be limited by the precision to which we can describe the ionization and dissociation effects on the neutral gas equations, and these will be dependent on the special conditions for the case considered.

The solution of the blunt body stagnation-point problem is of special interest in its application as a device for the determination of the space charge distribution about bodies of an arbitrary shape. That is, we propose to mount such a probe or probes on a vehicle. The probe measurements will then be interpreted in terms of the space charge at a point in a region undisturbed by the probe. In this way, the blunt body stagnation-point probes can be used as instruments to map the space charge distribution about a vehicle of arbitrary shape. In turn, this procedure may have direct application to our primary problem involving an atomic burst.

To investigate the above possibilities further, our immediate plan includes the extension of the theory and measurements for the blunt body stagnation-point region given in the present paper to higher flow Mach numbers, gas velocities, and altitudes. For these experimental measurements, we plan the use of a shock tunnel. Then, depending on the success of this preliminary shock tunnel work, we will consider the insertion of simple body shapes in the shock tunnel and

attempt to interpret our measurements on blunt body probes in terms of the ion-electron density at a point in the neighborhood of the body. Then, by a point-by-point determination, we hope to map the charge distribution about a vehicle.

CONTENTS

ABSTRACT

A model of the ion-electron flow in the stagnation region between the detached shock and the wall of a Langmuir-type probe is proposed for ionized air in a shock tube at ion mass fractions less than 10^{-4}. Based on the close agreement between numerical calculations and measurements of the probe wall ion current density, the proposed model gives an accurate description of the ion-electron flow in the stagnation-point boundary layer when negative potentials are applied at the stagnation point of the probe. The procedure is indicated to be applicable also in the region between the detached probe shock and the edge of the boundary layer. The ion and electron densities in the boundary layer are shown to be strongly dependent on the equilibrium conditions for the high-temperature gas behind the shock. Hence, the ion and electron number densities in the undisturbed incident flow ahead of the detached shock cannot be obtained unless it is possible to calculate the changes in the number densities across the shock.

The measurements were made using bottled dry air as the test gas for shock tube Mach numbers from 7.2 to 11.0, electrode potentials (referred to the plasma potential) of -6.1, -11.5 and -22.3 v, initial shock tube pressure of 1 cm Hg, and initial shock tube temperatures between 295 and 300°K. The ion number density distribution through the boundary layer including the sheath is calculated for an electrode potential of -11.5 v at shock tube Mach numbers of 7.43, 9.88, and 10.43. Additional calculations are presented for the determination of the electric field, wall ion current density, and sheath thickness for potentials in the range -2 to -24 v. The effects of some of the lesser-known parameters on the ion current density calculations are also indicated. These parameters include the Lewis number for the nitric oxide ion-electron pair in the partially ionized boundary layer flow, initial ion number density at the edge of the boundary layer, stagnation-point velocity gradient, and the ion-electron formation-recombination rates in the boundary layer.

LIST OF SYMBOLS

a sound speed, cm/sec

$\bar{c}$ average random thermal velocity, cm/sec

c_j mass fraction of component j

c_{pj} specific heat per unit mass at constant pressure of component j

c_p $\Sigma c_j c_{pj}$

D diffusion coefficient for gas mixture, cm^2/sec

D_a ambipolar diffusion coefficient for NO^+ ion-electron pair, cm^2/sec

D_i diffusion coefficient for NO^+ ion, cm^2/sec

D_j diffusion coefficient for component j, cm^2/sec

D_o probe diameter, cm

e electron charge = 1.60 (10^{-19}) coulomb = 4.80 (10^{-10}) esu

f Blasius function

g enthalpy ratio = $(h + u^2/2)/h_e$

h enthalpy per unit mass of mixture

h_j perfect gas enthalpy per unit mass of component j

h_j^o heat evolved in the formation of component j at 0 ^oK per unit mass

j ion current, amp

J y component of ion current density, amp/cm^2

k coefficient of thermal conductivity, $cal/sec\text{-}cm\text{-}^oK$

K NO^+ mobility, $cm^2/v\text{-}sec$

K_f rate constant for ion-electron formation, $cm^3/ion\text{-}sec$

K_r rate constant for ion-electron recombination, $cm^3/ion\text{-}sec$

ℓ Chapman-Rubesin factor = $\rho\mu/\rho_w\mu_w$

$\bar{L}$ ion mean free path, cm

L Lewis number for gas mixture = $\rho D\bar{c}_p/k$

L_i Lewis number for ion-electron pairs = $\rho D_i \bar{c}_p/k$

L_p probe shock detachment distance, cm

m_i mass of NO^+ ion, g

M flow Mach number of gas mixture

M_s shock tube Mach number

n ion number density, ion/cm^3

$\langle N \rangle$ nitrogen number density, atom/cm^3

$\langle N_g \rangle$ number density of gas mixture, particle/cm^3

$\langle O \rangle$ oxygen number density, atom/cm^3

p pressure, cm Hg or atmospheres

P density ratio = ρ_e/ρ

r radial distance of probe surface from axis of symmetry, cm

R gas constant for air = 1.987 cal/mole-^oK

s mass fraction ratio for ions = c_i/c_{ie}

s_j mass fraction ratio for jth component = c_j/c_{je}

t time, sec

t_f time required for equilibrium ionization, sec

T absolute temperature, ^oK

u x component of gas mixture velocity, cm/sec

U x component of gas mixture velocity at outer edge of boundary layer, cm/sec

v y component of gas mixture velocity, cm/sec

v_D y component of ion diffusion velocity due to concentration gradient, cm/sec

v_E y component of ion diffusion velocity due to electric field, cm/sec

$\bar{v}$ y component of total ion velocity = $(v + v_D + V_E)$, cm/sec

W mass rate of formation of ions, g/sec-cm^3

W_j mass rate of formation of component j, g/sec-cm^3

x distance along meridian profile, cm

y distance normal to the surface, cm

Z compressibility factor = $p/\rho RT$ ($Z = 1$ at S.T.P.)

β x component of velocity gradient at outer edge of boundary layer, sec^{-1}

δ_s sheath thickness, cm

δ_T thermal boundary layer thickness, cm

ϵ_o permittivity = 8.85 (10^{-12}) coulomb^2/newton-m^2

η defined by equation (3.10)

θ temperature ratio = T/T_e

κ Boltzmann constant = 1.38 (10^{-23}) joule/^oK

μ absolute viscosity, kg/sec-m

ξ defined by equation (3.10)

ρ mass density, kg/m^3

σ Prandtl number = $\mu\bar{c}_p/k$

σ_{12} average molecular diameter, Å, see p 22

ϕ sheath potential referred to plasma, v

ϕ_p probe potential referred to shock tube wall, v

ψ stream function, see p 17

SUBSCRIPTS

o initial shock tube condition

1 ahead of detached probe shock

2 immediately behind probe shock

e stagnation value for a point at the outer edge of the thermal boundary layer

i ion

j jth component of mixture

s outer edge of sheath

T outer edge of thermal boundary layer

w wall

1. INTRODUCTION

It was recently shown how probes could be used in a low density plasma jet to obtain point measurements of undisturbed

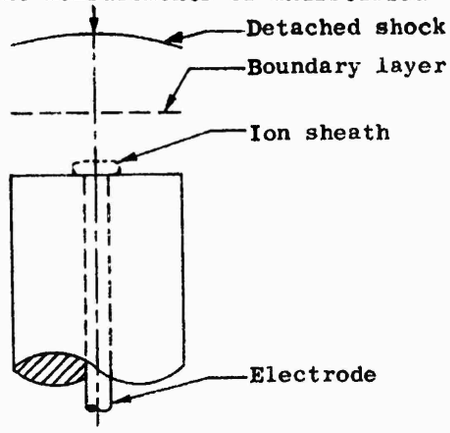

Stagnation-point probe

incident ion and electron densities (ref 1, 2, 3,). As shown in the above sketch, the probe consists of a flat-headed circular cylinder with an electrode placed at the stagnation point of the incident flow. For air at equilibrium fractional ionization densities less than 10^{-4}, all electrons and ions may be assumed formed through the reaction (ref 4)

$$N + O \rightleftarrows NO^{+} + e \tag{1.1}$$

To measure ion current only, the electrode is biased negatively with respect to the plasma. The negative potential causes an ion sheath to form at the electrode and, if sufficiently strong, will repel all electrons. A boundary layer is formed at the probe wall and its thickness in the stagnation region is much less than the probe shock detachment distance. The sheath is much thinner than the boundary layer. Consequently, outside the sheath, ions and electrons in the boundary layer diffuse through the gas mixture at a speed corresponding to ambipolar diffusion. In the sheath there occurs diffusion of ions.

The well-known blunt-body stagnation point solutions for the continuum flow of a nonionized gas are applicable for slightly ionized gases. These solutions give the enthalpy, pressure, and velocity distributions for the gas mixture in the stagnation region between the detached shock and the probe wall. The equation for the electric potential together with the conservation equations for ions and electrons yields solutions for the electric potential, ion and

electron distributions in the boundary layer between the shock and the probe wall. The flow and fluid properties of the gas mixture as well as formation and recombination rate constants of the various air constituents are known in the entire region behind the shock. Accordingly, ion and electron distributions between the probe wall and detached shock can be determined. Moreover, the ion-electron density of the incident flow may be obtained when the variation of this quantity across the shock is known. For neutral plasma flow behind the probe shock, due to ambipolar diffusion, the electron and ion flows and density distributions are the same, excluding the thin sheath formed at the stagnation point.

For the low gas densities in the plasma jet, frozen flow is assumed in the entire region between the detached probe shock and the stagnation point. The ion sheath is a small fraction of the boundary layer thickness. Since the fractional ionization is less than 10^{-2} and the sheath is so thin, the charged particles are assumed to have no effect on the enthalpy and motion of the neutral gas. The mean free path of the gas is sufficiently small to permit the use of the hypersonic boundary layer equations. Therefore, outside the sheath, the ion motion is assumed to be the sum of the gas motion and the relative motion due to ion-electron ambipolar diffusion.

In a low-density plasma jet, the ion mean free path is larger than the sheath thickness, and consequently, ion collisions do not occur within the sheath. Moreover, since the ion drift velocity is small compared with the ion thermal velocity, the potential distribution within the sheath is given by the familiar Child's law,

$$J = \frac{4\epsilon_o}{9\delta_s^2}\left(\frac{2e}{m_i}\right)^{1/2} |\phi_w|^{3/2}$$

The current density is assumed constant within the sheath by virtue of the assumed free-fall flow of the ions through the sheath. Moreover, J is independent of ϕ_w and within the sheath $\phi \propto y^{4/3}$. Thus, when the ion density ratio across the probe shock is known, which here is assumed equal to the gas density ratio, the undisturbed free stream ion or electron number density at a point ahead of the probe may be determined from the measured probe current density by solving the hypersonic boundary layer equations and the sheath equation.

The present effort is an extension of the above work in that ion-electron densities in a neutral plasma are measured in a shock tube for which the gas is about 10^3 times more dense. This increased density changes the physics of the flow in a number of ways. The region between the detached probe shock and the stagnation point is no longer frozen. The ion number density increases by a factor of more than 100 between the shock and the edge of the thermal boundary layer. As shown by the calculations in section 3.4, the ionization attains thermodynamic equilibrium in this region.

Ion-electron recombination occurs within the boundary layer up to the edge of the sheath, where electrons are sharply repelled because of their low energy (approximately 0.3 v). For a probe in a shock tube, the sheath is also much thinner than the boundary layer and the fractional ionization encountered in the present test measurements and calculations was always less than 10^{-4}. However, the flow incident to the probe is now supersonic, and the corresponding boundary layer equations are applicable. Outside the sheath, the ion motion is again the sum of the gas motion and the relative motion due to ion-electron ambipolar diffusion. Here, the diffusion velocity is appreciably affected by formation and recombination.

Additional ion-electron formation within the sheath is negligible when the sheath is a small fraction of the boundary layer. Accordingly, formation within the sheath becomes important at low shock tube Mach numbers and large probe potentials.

Inside the sheath, ion collisions occur mainly with neutral particles. Hence, the ion flow through the sheath is largely governed by the mobility and the electric field resulting from the potential applied at the probe. In addition, the sheath equation includes terms to account for the initial ion drift velocity across the sheath due to the neutral gas motion and diffusion caused by a concentration gradient. Here, ion thermal diffusion does not affect the probe current density. The current density increases slightly with distance from the stagnation point, because ions are carried away by the neutral gas flow tangential to the probe surface.

Thus, in the shock tube, a determination of the ion or electron number density distribution in the stagnation region of a blunt body behind the detached shock requires the solution of the supersonic boundary layer equations and also a different sheath equation. In addition, account must be taken of the ion-electron formation and recombination processes, which in turn require a knowledge of the local thermodynamic conditions and the rate constants. To obtain the undisturbed incident ion or electron number density, the variation in the number density across the probe shock must also be known. Since the flow is not frozen, this variation is not determined by the gas density ratio across the shock, as was the case for the plasma jet.

The following presentation describes the ion-electron flow in the boundary layer behind the detached probe shock for the shock tube Mach numbers 7.43, 9.88, and 10.43 at an initial shock tube pressure of 1 cm Hg and temperature of 300° K for probe potentials in the range -5.4 to -21.6 v with air as test gas. A description of the test equipment and probe measurements of the stagnation-point ion current density made in the HDL 2 in. by 2 in. shock tube is given in section 2.

A model describing the physical processes involved in the flow over the probes permits the assumption of distinct flow regimes, see section 3. Using this model, ion-electron number density distributions

in the boundary layer behind the probe shock are calculated in section 4. The validity of the calculations is indicated by the comparison between the calculated and experimental values for the stagnation-point ion current density.

Calculations are included in section 4 to show the effects on the ion current density of variation of some of the lesser known parameters. The parameters varied include the ratio of the Prandtl to Lewis numbers (the Schmidt number) for the ion-electron pairs in the partially ionized boundary layer flow, initial ion number density at the edge of the boundary layer, stagnation point velocity gradient, and the ion-electron formation and recombination rates in the boundary layer.

In appendix A, for the described test conditions, Coulomb forces are shown to have a negligible effect on the ion mean free path and the coefficients for diffusion and viscosity.

2. EXPERIMENTAL MEASUREMENTS

2.1 Test Equipment

The test measurements were made in the HDL 2 in. by 2 in. shock tube facility. The unit is an ordinary single-diaphragm straight shock tube in which the shock velocity is varied by controlling the driver gas enthalpy; the shock tube Mach number was varied through controlled heat addition to helium driver gas. The shock tube Mach number is determined with a precision of better than 1 percent, using six pressure pickups at 1-ft intervals along the tube. All the reported data were obtained using bottled dry air as the test gas at an initial pressure of 1 cm Hg and initial temperatures between 295 and 300° K.

The shock tube comprises two sections, one of which is movable and permits the lengthening of the tube for inserting test sections of lengths up to 30 in. A special test section to mount probes was constructed from a single piece of 2-in. thick plexiglas and located 17 ft from the aluminum diaphragm. Figures 1, 2, and 3 show the position of the test section in the shock tube and the installation of the probes with axes parallel to the tube centerline. In figures 1, 2, and 4, a second plexiglas section is shown adjacent to the test section to help illustrate the probe installation and flow of the hot gas over the probes. This section was removed during the test measurements to obtain a flush alignment between the walls of the test section and the shock tube. The stagnation point of all the probes tested was always located upstream of the test section-shock tube joint.

Four base supports were placed symmetrically in the test section with the centerline of each support parallel to and 1/2 in. from the vertical centerline of the shock tube (fig. 2 and 3). This allowed the stagnation point of each of four probes to be located 1/2 i . from the two near walls of the shock tube in the same plane normal

to the shock tube axis. Each support has a metal insert connected to a center cable and to the center electrode of an external plug, all of which is electrically insulated from the exposed outer surface of the base support. The latter was electrically connected to ground through the external plug, using the shock tube wall as ground. A probe was threaded into the metal insert of each support, thus connecting the probe electrode to the external plug. A teflon washer was used to insure electrical insulation of the probe electrode from the plasma and base support (fig. 2). The probe electrode was insulated everywhere from the plasma, except at the stagnation point.

Four simultaneous probe current measurements were recorded using two Tektronix 555 dual-beam oscilloscopes. Figure 4 shows the flow over the probes during a typical test, the radiation of the hot gas causing the film exposure.

A total of five sets of probes was constructed. Three sets were flat-headed circular cylinders each of 2-in. length (excluding thread) having glass insulation over the electrode with the following dimensions:

(1) 0.02-in. electrode, 0.25-in. diameter cylinder,
(2) 0.06-in. electrode, 0.25-in. diameter cylinder,
(3) 0.02-in. electrode, 0.10-in. diameter cylinder.

The third set was broadened to 0.25 in. diameter at the base in order to secure firmly in the support (fig. 3).

A fourth set of 1-in. length probes with dimensions otherwise identical with set 2 was constructed with a brass sleeve concentric with the cylinder axis and running the entire length of the probe. An epoxy resin insulator was used between the sleeve and the brass electrode. Two of these probes are shown in figure 3, outside the test section.

In the fifth set, each probe consisted of a conical nose with a 20-deg vertex angle and 0.25-in cylindrical afterbody. Excluding thread, the probes were of 2-in. lengths. The electrode was exposed to the plasma at the nose tip for 0.142 in., which corresponds to a diameter of 0.050 in. Glass insulation covered the remainder of the probe.

For reasons given in section 2.2, current measurements are reported only for the first three sets of probes. As discussed in section 2.2, the plasma potential may be assumed to be about +0.7 v, referred to the shock tube wall. Ion currents were measured by using probe potentials of -5.4, -10.8, and -21.6 v, with the shock tube wall as ground. These potentials were obtained by placing mercury cells in series, each cell having a potential of 1 35 v and capable of

delivering 10 ma. The current was always observed to be less than 10 ma and the steady-state value never exceeded 3 ma. A resistor was placed in series between the battery and ground, and the oscilloscope was connected across the resistor. The resistor had a value of 100 or 1000 ohms and was always used so that the steady-state potential drop across it and thereby the reduction in the probe potential was less than 2 percent of the applied potential. The complete circuit from probe to ground had a capacitance of 4×10^{-10} f, so that the time constant with the 1000-ohm resistor was 0.4×10^{-6} sec^{-1}.

The d-c conductivity of the undisturbed air stream increases with increasing M_s and amounts to about 0.01 mho/cm at M_s = 10.5 (fig. 5 of ref 6). Thus, for sufficiently large M_s, it was conceivable that the gas could provide a conducting path between adjacent probes or, because of the increased conductivity behind the detached probe shock, a conducting path could be established between a probe and the shock tube wall. To determine whether this effect was present, at the higher M_s, current density measurements were obtained using both 100- and 1000-ohm resistors. In addition, measurements obtained by setting all four probes at the same potential were compared at the same potential and M_s with measurements obtained when each of the four probes was set at four different potentials. In each instance, no observable effect was noted, and thus it appears that the gas conductivity did not influence the measurements.

2.2 Test Results

Initially, measurements were made using four identical probes biased at the same potential to observe the uniformity of the ionized flow across the tube and determine bias and repeatability of the probes. As shown in figure 5 for ϕ_p = -10.8 v on the 0.06-in. electrode, 0.25-in. diameter probes, the total variation of the four measured probe currents on a given test is within 20 percent and is usually closer to 10 percent. This variation does not appear to be due to individual peculiarities in the probes, although the results of the measurements were altered when the probe faces were not clean and polished, and when occasionally the probes were deformed during a test series by diaphragm debris (in the form of very fine aluminum dust particles impacting the probe face). After about 20 firings, the currents measured by one or two probes would suddenly increase 50 per cent or more above the currents measured by the remaining probes. This was apparently due to diaphragm dust that had coated the probe face, for on polishing the probe surface with a fine abrasive the probe current measurements were restored to their previous values. This dust coating was observable with the naked eye and serveral of the larger flakes along the test section wall were noted, by means of an ohmmeter, to be an electrical conductor.

As may be seen from figure 5, an error of 1 percent in the determination of M_s will result in a 10-percent error in j. The

precision in the determination of M_s appears a little better than 1 percent. Therefore, taking into account the variations in the individual probe readings and the error in the M_s determination, the accuracy of the measurements is ±15 percent.

As shown in figure 6, additional measurements were made on the 0.06-in. electrode, 0.25-in. diameter probes over the Mach number range 7.2 to 11.0 at probe potentials of -21.6, -10.8 and -5.4 v.

All measurements with the other two sets of probes were made at ϕ_p = - 10.8 v. As indicated in figure 7, the repeatability appears to be about the same as previously noted in figure 5.

The current measurements for the 0.02-in. and 0.06-in.

M_s	j 0.02-in. electrode (μamp)	j 0.06-in. electrode (μamp)	$\frac{j(0.06\text{ in.})}{j(0.02\text{ in.})}$
8.6	28.9	245	8.48
9.0	42.5	355	8.35
9.4	56.1	475	8.46
9.8	69.7	620	8.89

electrode probes with diameter of 0.25 in. at various M_s are compared in the above table. Assuming no fringe or sheath effects and no variation in the current tangential to the probe surface, the j ratio for the two sets of probes should be the same as the ratio of their electrode areas, 9:1. As shown in the table, this ratio is about 8.5:1; the difference between this ratio and the ratio 9:1 is within the accuracy of the test measurements. A reduced ratio could be expected to occur if the sheath thickness added to the effective electrode area, for, as will be seen in section 4 (fig. 12a) at ϕ_p = -10.8 v, δ_s amounts to about 20 microns over the M_s range 8.6 to 9.8. Assuming the electrode diameter to be increased by $2\delta_s$, the reduction in the j ratio would be 10 percent. However, since this difference is also within the experimental accuracy, fringe or sheath effects may not be accounted for in this manner. Most importantly, however, we can conclude that the electrodes are located in a region that is essentially independent of variation of the current tangential to the probe surface. Hence, in the sheath equations in sections 3.7 and 4, we need refer only to the one-dimensional Poisson equation for the electric potential. Although the measurements on the 0.06-in. electrode probes are equivalent to those of the 0.02-in.

electrode, 0.25-in. diameter probes, the noise-to-signal ratio on the latter probes was significant at low M_s. Hence, the measurements on the smaller electrode, 0.25-in. diameter probes were discontinued and future reference will be made only to the 0.06-in. electrode probes

The current measurements shown in figure 7 for the 0.22-in.

M_s	j 0.25-in. probe (μamp)	j 0.10-in. probe (μamp)	$\frac{J\ (0.10\ in.)}{J\ (0.25\ in.)}$
8	129	48	3.35
9	354	154	3.91
10	707	305	3.88
11	1288	489	3.42

electrode, 0.10-in. diameter probes are compared in the above table with those shown in figure 6 for the 0.06-in. electrode, 0.25-in. diameter probes at $\phi_p = -10.8$ v. The current density, J, is obtained by dividing the current by the electrode area. According to the table, allowing for the experimental error, the measured current densities of the 0.10-in. probes are larger by a factor of about 3.7. This difference is due to the fact that the values of $\beta = U/x$ for the 0.10-in. diameter probes are larger by a factor of 2.5. Since the effect of β on the two sets of measurements will involve specific calculations of boundary layer thickness, gas velocity, ion-electron recombination, etc, the discussion of the effect of reducing the probe diameter will be deferred to section 4.1.1,(see pp. 30-32).

In the solution of the sheath equations, the probe potential must be referred to the plasma potential. In all the measurements, the probe potentials were referred to the shock tube wall, which will generally be at a potential different from that of the plasma. The floating potential of the probes was found to be +0.45 $\pm$0.15 v for M_s in the range 9.2 to 10.8. In gas discharges, the plasma potential is approximately 0.2 v larger than the floating potential, because of the higher random velocity of the electrons compared with the ion random velocity (ref 7). In the boundary layer, the ion random motion is at least an order of magnitude larger than the uniform gas velocity. Hence, we may neglect the effect of the gas motion and assume the plasma potential referred to the shock tube wall as +0.7 v.

As previously noted, a fourth set of probes with 0.06-in. electrode, 0.25-in. diameter cylinder was constructed having an outer brass sleeve concentric with the cylinder axis. The brass and glass

probe measurements were compared for M_s in the range 9.2 to 10.8 at ϕ_p = -21.4 v. The purpose of this comparison was to determine whether a static charge could develop on the glass insulation and thereby influence the data. Measurements were made with the brass sleeves both insulated from and grounded to the shock tube through the base supports. Since within the experimental error of ±15 percent these measurements appeared identical, only the glass probe results are given.

The signal forms of the oscillograms for all the flat-headed probes appeared approximately the same, regardless of cylinder diameter. The upper trace in figure 8 for M_s = 8.9 is typical for the flat-headed probes. The probe current is measured by the vertical scale and the time trace is left to right at 20 μsec per division. In figure 8, the signal begins at the point (a) and is unsteady for about 20 μsec to point (c). The signal then remains at an approximately constant value until the contact surface reaches the probe, whereupon it rapidly falls to zero. Probes that were not clean also exhibited an interval of increasing ion current signal prior to the appearance of the contact surface, the total rise being as much as 20 percent of the steady-state signal. The duration of the steady-state ion current was always at least 30 μsec and increased with decreasing Mach number to about 120 μsec at M_s = 7.2.

The initial unsteady signal lasted for about 16 μsec at M_s = 11.0 and lasted as long as 40 μsec at M_s = 7.2. For a given test, individual deviations in the time duration of the initial unsteady signal for the four probes could be as much as ±10 percent. As suggested by the strong initial pulse shown in the upper trace of figure 8, the unsteady signal would seem to be the time required for the flow to attain a steady state, rather than the time to attain a steady-state ionization level. The strong initial ion current is probably due to the detached probe shock moving out into the flow, thereby increasing the shock strength and the ionization level.

To support these contentions, the conical probes described in the previous section were constructed to determine the time required to attain a steady signal and observe the signal form. As shown in the lower trace of figure 8, no large initial pulse or probe current appears. The signal begins at point (a) and rises linearly to point (b). Here, the absence of a strong initial pulse is explained by the formation of an attached conical shock of a strength much weaker than the detached normal shock of the flat-headed probes. Moreover, the unsteady signal of the conical probe gradually increases to the steady-state value at point (b) in about 6 μsec which, at M_s = 8.9, is approximately four times longer than the time required for the shock to travel the 0.142-in. length of the exposed electrode (ref 8). This additional time may be required to fully establish the ion current. However, the unsteady signal for the next 14 μsec to point (c) is not understood. The unsteady signals shown by the

two traces of figure 8 between points (a) and (c) are typical and were largely repeatable.

No noticeable change in the test data appeared because of variation in T_o between 295 and 300° K. This appears reasonable in view of the following consideration. At p_o = 1 cm Hg and M_s between 9 and 10, a change in T_o of 5° K amounts to a change in T_e of 80 to 95° K (ref 8). At 300° K, the difference in T_e between M_s = 9 and 10 amounts to 900° K. As shown in figure 6 for ϕ_p = -10.8 v, j increases from 0.355 ma at M_s = 9 to 0.705 ma at M_s = 10. Since the increase in n is due primarily to the increase in temperature (ref 4) it appears that the 5° difference in T_o will provide about a 10-percent increase in j. As may be seen from figure 6 and reference 8, the variation in j due to a change in T_o from 295 to 300° K is approximately the same at other M_s and ϕ_p. Thus, this variation in j is within the ±15-percent accuracy of the measurements.

Although a few measurements at $T_o < 295°$ K appeared to give lower values of j, this effect was not sufficiently investigated to make a quantitative statement.

3. ION FLOW IN THE STAGNATION REGION OF A BLUNT BODY

3.1 Flow Model

It is convenient to describe the flow over a probe by construction of a model in which distinct flow regimes are assumed. It appears possible to assume the following three distinct flow regimes:

(1) The detached probe shock and outer edge of the thermal boundary layer form the boundaries of a region in which the incident ion number density is increased by a factor of more than 100 and attains thermodynamic equilibrium upstream of the edge of the thermal boundary layer.

(2) The outer edges of the thermal boundary layer and the ion sheath, which envelopes the probe electrode and is completely imbedded within the boundary layer, form the boundaries of a region in which the usual supersonic stagnation-point boundary layer equations for a nonionized gas mixture apply together with the conservation equations for ions and electrons. The latter equations include terms for ambipolar diffusion and formation-recombination of ion-electron pairs. Due to the low fractional ionization, the boundary layer equations for the neutral gas are not altered by the presence of ions or by their additional formation or recombination.

(3) Electrons are sharply repelled at the sheath edge. The neutral gas equations together with the ion conservation and the one-dimensional Poisson equations determine the ion flow within the sheath.

As will be shown by numerical calculations, this model appears valid for $M_s > 7$, the value for the lower M_s limit depending on ϕ_w, D_o and p_o.

The calculations of sections 3.2, 3.3, and 3.4 show that the ion-electron transit time through region (1) is sufficiently long to attain equilibrium ionization at the edge of the boundary layer. The derivation of the stagnation-point boundary layer equations through the flow regions (2) and (3) are given in sections 3.5, 3.6, and 3.7. Also in 3.7, the electron penetration of the sheath is shown to be negligible. In section 4, the numerical calculations of the boundary layer and sheath thicknesses and the excellent agreement between the calculated and measured values of J_w indicate the validity of the assumed flow model.

3.2 Flow Time from Detached Probe Shock to Outer Edge of Thermal Boundary Layer

The Mach number of the gas flow incident to the probe is supersonic for $M_s \geq 7$. Thus, the gas temperature and other fluid properties change appreciably across the detached probe shock. The calculated gas mixture velocities and properties in the different shock tube flow regimes were determined using references 8 and 9, and the ionization densities were determined using reference 4.

The temperature, density, and pressure behind the probe shock differ by less than 10 percent from their stagnation values for p_o in the range 2.0 to 0.2 cm Hg, $T_o = 300^o$ K, and M_s from 7 to 10. In particular, for this flow regime, the difference in the ion-electron densities between conditions immediately behind the probe shock and stagnation amounts to about 35 percent of the former. Consequently, to calculate the time for ionization to reach equilibrium, the region between the detached probe shock and the boundary layer may be considered one of constant fluid properties and ionization.

The gas flow decelerates approximately linearly in the inviscid region behind the probe shock, and the velocity at the edge of the boundary layer is only about 2 percent of the velocity immediately behind the shock. The ion velocity is the sum of the gas motion and the relative motion due to ambipolar diffusion. Because of ion formation between the probe shock and the boundary layer, the diffusion velocity is in a direction opposite to the gas motion. In the following calculations, the diffusion velocity is neglected. We obtain time values somewhat smaller than those actually required for the flow to cross the region bounded by the outer edge of the thermal boundary layer and the probe shock. As will be seen in section 3.4, these times are still sufficient to attain equilibrium ionization.

For the linear deceleration of the gas motion in the inviscid region behind the probe shock, the approximate time for the ions to traverse the distance between the detached shock and the thermal boundary layer is given by

Table II summarizes the calculations for M_s from 7 to 10 at p_o = 1.0 and 0.2 cm. Values for p_e and T_e were obtained from reference 8. It is clear from these results that for sheath thicknesses of the order of a micron or larger, collisions occur within the sheath and the drift velocity and probe current will be governed largely by ion mobility and not by free-fall diffusion. The sheath thicknesses calculated in section 4 (fig 12a) indicate that this is indeed the case.

3.4 Time Required to Attain Equilibrium Ionization

As noted in section 3.2, the flow in the region between the detached probe shock and thermal boundary layer has approximately constant values of temperature, density, pressure, and equilibrium ionization (if attained) equal to those occuring at stagnation. The time required for the gas to reach equilibrium ionization for stagnation conditions is given below for M_s from 7 to 10 at p_o = 1.0 cm and M_s = 9 and 10 at p_o = 0.2 cm.

The production of ions and electrons at the fractional ionization levels encountered here, less than 10^{-4}, is governed by the reaction

$$N + O \rightleftarrows NO^+ + e \tag{1.1}$$

At fractional ionization concentrations less than 10^{-4}, the electron and NO^+ concentrations are approximately equal.

The formation of equilibrium values of dissociated N and O takes place within several hundred collisions (ref 5, 12, 13). The mean free paths of the ions and neutrals behind the probe shock are approximately equal to the values of $\bar{L}_e$ given in table II. Since the ion and neutral random velocities are about 2 x (10^9) micron/sec, the required time for equilibrium dissociation is less than 0.1 μsec. This time is negligible compared with the values given in table I for the time required for the ions to traverse the region bounded by the probe shock and thermal boundary layer. Hence, the time required for dissociation will be neglected in the following calculations.

The change in the ion or electron number density is given by

$$W/m_i = dn/dt = K_f \langle N \rangle \langle O \rangle - K_r n^2 \tag{3.3}$$

where the formation and recombination rate constants are given by equations (62-b) and (64-b) of reference 5 as

$$K_f = 5(10^{-11})\, T^{-0.5} \exp(-32{,}500/T)$$

and

$$K_r = 3(10^{-3})\, T^{-1.5} \quad cm^3/ion\text{-}sec \tag{3.4}$$

The equilibrium ion number density increases across the probe shock by a factor exceeding 100. Consequently, the reduction in dn/dt by recombination is seen by equation (3.3) to depend on n^2, and therefore, recombination becomes significant only as $n \to n_e$. Hence, we may neglect recombination and assume that the time required to attain equilibrium ionization is governed by the equation

$$t_f = n_e/(K_f \langle N \rangle \langle O \rangle)_e \tag{3.5}$$

The calculations for t_f are summarized in table III, where the values for the equilibrium densities of $\langle N \rangle$, $\langle O \rangle$ and n were determined from reference 4.

A comparison of the times calculated in tables I and III shows that equilibrium ionization is attained when M_s and p_o are sufficiently large. Accordingly, for the 0.25-in. probes, it appears that equilibrium ionization occurs ahead of the thermal boundary layer at $M_s \geq 7.4$ when $p_o \geq 1.0$ cm and at $M_s \geq 8.3$ when $p_o \geq 0.2$ cm.

As noted in section 3.2, taking into account the decreased shock detachment distance and boundary layer thickness, the ion transit time from the shock to the thermal boundary layer for the 0.10-in. probes will be 0.35 times as large as that for the 0.25-in. probes. Hence, for the 0.10-in. probes, equilibrium ionization occurs ahead of the thermal boundary layer at $M_s \geq 7.9$ when $p_o \geq 1.0$ cm and at $M_s \geq 8.8$ when $p_o \geq 0.2$ cm.

In section 4, equilibrium ionization will be assumed at the edge of the thermal boundary layer for $M_s \geq 7.43$ at $p_o = 1$ cm for both the 0.25- and 0.10-in. probes. For the latter probes at low M_s this requires an increase of the time values in table I or a decrease of the time values in table III, each by a factor of 2. This factor can be accounted for by the ion diffusion due to formation between the shock and the boundary layer, which reduces the ion flow in the direction of the gas motion. Also this factor can be accounted for by assuming a somewhat larger value for K_f, for, as indicated in pages 25 and 34-36 and in figures 13-17 of reference 5, the rate constants may actually be three times larger than those given by equation (3.4).

3.5 Axisymmetric Laminar Boundary Layer Flow of Dissociated Air at the Stagnation Point

The preceding calculations show that equilibrium ionization is attained at the edge of the thermal boundary layer for sufficiently large D_o, p_o and M_s. The fractional ionization increases rapidly with increasing M_s, but there is only a small change with p_o in the range 2.0 to 0.2 cm. In section 4.1, the test measurements of the stagnation-point ion current density will be compared with the numerical calculations at $M_s = 7.43$, 9.88 and 10.43 for $p_o = 1$ cm. Here, the maximum ion number density fraction is 0.98 (10^{-4}) and occurs at the

edge of the thermal boundary layer. Ion-electron recombination occurs in the boundary layer prior to reaching the sheath, and the amount of recombination increases with increasing M_s. Consequently, as will be seen in section 4.1, due to recombination and the additional velocity due to ambipolar diffusion, the fractional ionization at the edge of the sheath is at most 10^{-5} for $M_s \leq 10.43$. The fractional ionization is further reduced in the sheath by the ion acceleration caused by the probe potential. Because of the low ion-electron concentration, the presence of the charged particles is assumed to have no effect on the neutral gas equations.

In particular, the ratio of the energy required to produce the ionization behind the probe shock to the air mixture total enthalpy is less than 10^{-3} for $M_s = 10.43$ and decreases with decreasing M_s. Assuming ion formation from N_2 and O_2, approximately 10 ev per ion are required (ref 5). At $M_s = 10.43$, the corresponding energy required to form $n_e = 23.2 \times 10^{14}$ ion/cm^3 is 3.72×10^{-3} joule/cm^3. This is insignificant in comparison with the air mixture total enthalpy of 8.89 joule/cm^3, calculated with the help of reference 4 and table IV. Hence the initial ionization level in the shock tube upstream of the probe shock has no effect on the enthalpy behind the probe shock.

In appendix A, Coulomb forces are shown to have a negligible effect on the diffusion and viscosity of the dissociated air mixture. Consequently, in the following presentation, the stagnation-point boundary layer flow is assumed to consist of a binary mixture of neutral gas particles and ion-electron pairs.

Neglecting the presence of the ion-electron pairs, a procedure for obtaining solutions of the dissociated neutral gas motion in the boundary layer is given in reference 14. Since these solutions will be used to obtain solutions of ion-electron flows, some of the details presented in the Fay-Riddell method of solution will be shown. In particular, reference will be made to their Method 2 solution.

The laminar boundary layer equations for axisymmetric dissociated air flow are given by*

$$\underline{\text{Continuity}}: \quad (\rho u r)_x + (\rho v r)_y = 0 \tag{3.6}$$

$$\underline{\text{Momentum}}: \quad \rho u u_x + \rho v u_y = -p_x + (\mu u_y)_y \tag{3.7}$$

$$\underline{\text{Energy}}: \quad \rho u h_x + \rho v h_y = (k T_y)_y + u p_x + \mu (u_y)^2 + \left[\Sigma D_j \rho (h_j - \quad) c_{jy}\right]_y \tag{3.8}$$

*Subscripts x and y (or η below) are used to denote partial differentiation.

Species Conservation: $$\rho u c_{jx} + \rho v c_{jy} = (D_j \rho c_{jy})_y + W_j \qquad (3.9)$$

where y and x are directions normal and tangential to the body surface, and r is the distance of the probe surface from the axis of symmetry. For the flat-headed circular cylinder probes previously described, r = x in the stagnation region. The enthalpy of the mixture is given by $h = \sum c_j (h_j - h_j^o)$. The terms for thermal diffusion are omitted in equations (3.8) and (3.9) since, for stagnation-point supersonic and hypersonic dissociated flows, the motion due to thermal diffusion has been found to be negligible compared with the flow due to concentration gradient (ref 15).

In stagnation-point flow, because of symmetry, all dependent variables are functions of y only, except u, which is proportional to x times a function of y. This includes W_j, since the formation and recombination of atoms are functions only of the local thermodynamic variables. Consequently, for stagnation-point flow, the exact partial differential equations may be transformed to exact ordinary differential equations.

The exact ordinary differential equations are obtained as functions of a single dimensionless variable η through use of the Howarth-Mangler transformation equations

$$\eta \equiv \frac{U}{\sqrt{2\xi}} \int_o^y r\rho dy$$

$$\xi \equiv \int_o^x \rho_w \mu_w U r^2 dx \qquad (3.10)$$

and the additional nondimensional variables

$$\partial f/\partial \eta \equiv u/U \qquad f = \int_o^\eta (\partial f/\partial \eta)\, d\eta \qquad \theta = T/T_e$$

$$\ell \equiv \rho\mu/\rho_w \mu_w \qquad g = (h + u^2/2)/h_e \qquad s_j = c_j/c_{je}$$

where the subscript e refers to values in the "free stream" at the stagnation point. Here, "free stream" denotes the fluid at the outer edge of the boundary layer that has passed through the detached shock close to the axis of symmetry.

To obtain a solution of the continuity equation (3.6), we note that $U = \beta x$ with β = constant. Referring to equation (3.10), we have

$$\sqrt{2\xi} = x^2 \sqrt{\beta\rho_w\mu_w/2}$$

$$\xi_x = \beta\rho_w\mu_w x^3$$

and $$\eta_y = \rho\sqrt{2\beta/\rho_w\mu_w}$$

We now assume $\rho ur = \psi_y$, $\rho vr = -\psi_x$ and $\psi = \sqrt{2\xi}\, f(\eta)$. This gives

$$u = \beta x f_\eta = U f_\eta \tag{3.11}$$

and $$\rho v = -f\sqrt{2\beta\rho_w\mu_w} - (\sqrt{\beta\rho_w\mu_w/2})\, x f_\eta \eta_x$$

Thus, the continuity equation (3.6) is satisfied.

By substituting into the terms of equation (3.7),

$$\rho u u_x + \rho v u_y = \rho\beta^2 x(f_\eta^2 - 2ff_{\eta\eta})$$

$$-p_x = \rho_e U U_x = \rho_e \beta^2 x$$

and $$(\mu u_y)_y = 2\rho\beta^2 x(\ell f_{\eta\eta})_\eta$$

Consequently, for stagnation-point flow, the momentum equation becomes (see eq A1 of ref 14),

$$(\ell f_{\eta\eta})_\eta + ff_{\eta\eta} + \frac{1}{2}(\rho_e/\rho - f_\eta^2) = 0$$

Before transforming the energy equation, we note that

$$\nabla h = [\Sigma c_j (dh_j/dT)]\, \nabla T + \Sigma(h_j - h_j^o)\nabla c_j$$

and we set $$\bar{c}_p = \Sigma c_j (dh_j/dT) = \Sigma c_j c_{pj}$$

Combining equations (3.8) and (3.9), there results (eq 20 of ref 14),

$$\bar{c}_p(\rho u T_x + \rho v T_y) = (kT_y)_y + up_x + \mu(u_y)^2 - \Sigma W_j(h_j - h_j^o) + \Sigma c_{pj} D_j \rho c_{jy} T_y$$

Assuming θ is a function of η only, the terms in the above equation can be written

$$\bar{c}_p(\rho u\theta_x + \rho v\theta_y) = -2\bar{c}_p\beta\rho f\theta_\eta$$

$$(k\theta_y)_y = (k\theta_\eta\rho)_\eta \frac{2\beta\rho}{\rho_w\mu_w} = (\bar{c}_p\ell\theta_\eta/\sigma)_\eta 2\beta\rho$$

$$up_x/T_e = -(\rho_e UU_x)u/T_e = -\beta^3 x^2 \rho_e f_\eta/T_e \to 0 \text{ at the stagnation point}$$

$$\frac{\mu u_y^2}{T_e} = \frac{\mu\beta^2 x^2}{T_e} f_{\eta\eta}^2 \eta_y^2 = \frac{2\mu\beta^3 x^2 \rho^2}{T_e \rho_w \mu_w} f_{\eta\eta}^2 \to 0 \text{ at the stagnation point}$$

$$\Sigma c_{pj} D_j \rho c_{jy} \theta_y = \frac{2\beta\rho^3}{\mu_w \rho_w} \theta_\eta \Sigma c_{pj} D_j c_{j\eta} = \frac{2\beta\rho^2}{\sigma} \theta_\eta \Sigma c_{pj} L_j c_{j\eta}$$

where $L_j/\sigma = D_j\rho/\mu$. Combining terms, the energy equation becomes (eq A10 of ref 14)

$$\left(\frac{\ell}{\sigma} \bar{c}_p \theta_\eta\right)_\eta + \bar{c}_p f \theta_\eta + \frac{\ell}{\sigma} \theta_\eta \Sigma c_{pj} L_j c_{j\eta} + \frac{W_j (h_j - h_j^o)}{2\beta\rho T_e} = 0 \qquad (3.13)$$

In the same way, we find that the species conservation equation (3.9) becomes (eq 34 of ref 14),

$$\left(\frac{\ell}{\sigma} L_j c_{j\eta}\right)_\eta + f c_{j\eta} + W_j/2\beta\rho = 0 \qquad (3.14)$$

Fay and Riddell assume dissociated air to be a diatomic gas composed of "air" molecules and "air" atoms with properties properly averaged between oxygen and nitrogen. Accordingly, we call c_A the mass fraction of atomic oxygen and nitrogen. Now, only one equation of the form (3.14) is needed. Closed form approximations are given for the thermodynamic properties as functions of θ and c_A. We then have the system of three equations (3.12), (3.13), and (3.14) in θ, c_A and f.

In their Method 2 solution, Fay and Riddell obtain two alternate forms of solution for c_A:

(a) The c_A is in thermodynamic equilibrium

(b) The c_A is frozen in the boundary layer, so that $W_j = 0$. For the equilibrium boundary layer, the W_j term is eliminated between equations (3.13) and (3.14) and the resulting equation is solved simultaneously with the momentum equation (3.12) and an equation that gives c_A as a function of θ. For the frozen boundary layer, equations (3.12), (3.13), and (3.14) are solved with $W_j = 0$.

The required boundary conditions are

$$\left.\begin{aligned} &f(0) = f_\eta(0) = 0 \qquad && f_\eta(\infty) = 1 \\ &\theta(0) = \theta_w && \theta(\infty) = 1 \\ &c_A(0) = 0 \text{ for catalytic wall} \\ &c_{A\eta}(0) = 0 \text{ for noncatalytic wall} \end{aligned}\right\} \quad c_A(\infty) = c_{Ae} \qquad (3.15)$$

For the equilibrium boundary layer, numerical solutions were obtained by Fay and Riddell on a digital computer using an iterative procedure whereby values were selected for $f_{\eta\eta}(0)$ and $\theta_\eta(0)$ until the required conditions at "infinity" were met, i.e., $f_\eta \to 1$ and $\theta \to 1$. For the frozen boundary layer, values were also selected for either $c_{A\eta}(0)$ (catalytic wall) or $c_A(0)$ (noncatalytic wall) with the added condition $c_A(\infty) = c_{Ae}$.

A summary of the various parameters and initial conditions for which numerical solutions of the stagnation-point dissociated boundary layer flow have been obtained by Fay and Riddell appears in table II of their Avco publication. For use in the present work, these authors made available three sets of numerical calculations, which are identified in their table II as

(a) equilibrium boundary layer with $\theta_w = 0.0538$

(b) frozen boundary layer with $\theta_w = 0.0497$

(c) frozen boundary layer with $\theta_w = 0.0797$

The last two calculations assume a catalytic wall with respect to atom recombination. All the calculations were made for $T_w = 300^\circ$ K, $L_j = L = 1.4$, and $\sigma = 0.71$. According to reference 8, the calculations in (a), (b), and (c) for the above θ_w correspond to the shock tube Mach numbers 9.88, 10.43, and 7.43, respectively.

The above solutions give f, θ, and ℓ in terms of η. With the help of reference 4, the compressibility factor can be found. Denoting this factor by Z, we can evaluate $\rho = p_e/RTZ$. From equation (3.10), there results

$$y = \sqrt{\rho_w \mu_w / 2\beta} \int_0^\eta (1/\rho) d\eta \tag{3.16}$$

Hence, all solutions may be expressed in terms of the distance from the wall, y, when β is known.

By table I, the Mach number of the flow incident to the probes is between 2.1 and 2.7. For this Mach number range, it appears that β may be determined to within ±15 percent by the relation given in reference 16 (see also ref 17-20).

$$\beta \simeq 0.64\ a_e/D_o \tag{3.17}$$

where a_e denotes the stagnation value of the sound speed. Using the values for p_e and ρ_e given in table I, a_e was evaluated with the help of table IV and figure 6 of reference 9.

The functions f, $\partial f/\partial\eta$, θ, ℓ and P are shown in figure 9 at M_s = 7.43, 9.88, and 10.43 for the 0.25-in. diameter probes. By

equations (3.16) and (3.17), $y \propto \sqrt{D_o}$. Accordingly, the above functions for the 0.10-in probes may also be obtained from figure 9 by reducing the given y values by the factor $\sqrt{2.5}$.

Shock tube experimental verification of the Fay-Riddell theory with respect to stagnation-point heat transfer is given in reference 21 for flow Mach numbers between 2.3 and 5. This compares with the flow Mach numbers 2.1 to 2.7 for the test measurements described in section 2. As shown in reference 14, the stagnation-point heat transfer for equilibrium boundary layer flow is approximately equivalent to that for frozen flow with identical catalytic wall (for atom recombination) and "free stream" conditions. However, the two flows result in different distributions for f, θ, and ℓ. For a frozen boundary layer, the assumption of a noncatalytic wall (for atom recombination) results in excessively small heat transfer (ref 14,21) and an examination of the recombination rates indicates that a noncatalytic wall can be realized only at initial shock tube pressures below 1 mm Hg (ref 21).

3.6 Ion-Electron Boundary Layer Flow outside the Sheath

Outside the sheath, due to ambipolar diffusion, the description of the ion flow is the same as that for electrons. Accordingly, only the equations for ions will be considered. The ion conservation equation has the same form as the species conservation equation (3.14) and may be written as

$$\left(\frac{\ell}{\sigma} L_i \, s_\eta\right)_\eta + f s_\eta + \frac{W}{2\beta c_{ie} \rho} = 0 \qquad (3.18)$$

where $s = c_i/c_{ie}$. Equation (3.18) applies in the region $\delta_s \leq y \leq \delta_T$.

Two boundary conditions are required for the solution of equation (3.18). With the help of equation (3.16) we can refer to the flow and boundary conditions as functions of y. At $y = \delta_T$, $\theta = s = 1$. At any point in the boundary layer, there is an infinite number of (s, s_y) pairs that yields $s = 1$ at $y = \delta_T$. The y component of the ion current density is $J = \bar{v} e n$, where $n = n_e s/P$ and outside the sheath $\bar{v} = -v + D_a s_y/s$. Accordingly, since outside the sheath J is a function of s and s_y, the other boundary condition is determined by the requirement of continuous s and J across the sheath. Hence, we require the (s, J) pair at δ_s that satisfies the boundary condition at infinity in equation (3.18) and is compatible with the remaining boundary conditions given for the sheath equations.

To obtain numerical solutions, a value for the sheath thickness was arbitrarily selected. Starting at this value for $y = \delta_s$, equation (3.18) was solved for a number of (s, s_y) pairs, obtaining thereby

a continuous curve of J as a function of s at δ_s.* By equations (3.16) and (3.18), at any δ_s, we see that the curve $s_{ys}(s_s)$ must have a negative slope. From the above definition of J, for the curve $J_s(s_s)$ to have a negative slope, the increase in the term $D_a s_y$ resulting from a reduction in s must be larger than the reduction in the term vs. For each value of δ_s where $0 > \phi_w > -30$ v, all calculations demonstrated that the curve $J_s(s_s)$ had a negative slope over the required range of s_s. As will be seen in section 3.7, the possible solutions for the sheath equations lie along a single curve for which $\partial J_s/\partial s_s > 0$ and, if a solution of the boundary layer flow exists, this curve intersects the previous curve at a single point. The solutions for the ion flow through the boundary layer are therefore unique and single-valued for each δ_s.

Equation (3.18) was solved using the solutions for ℓ, T, f, and ρ given in section 3.5, constant values for $L_i/\sigma = 2$ and 3, and the values for β and $c_{ie}/m_i = n_e/\rho_e$ in table IV. W is given by equations (3.3) and (3.4).

The contribution to W from ion-electron formation is dependent on the boundary layer distribution of <N> and <O>. The equilibrium dissociation fraction at δ_T varies between 14 and 23 percent at p_o = 1cm for $7.43 \leq M_s \leq 10.43$. However, ion-electron formation in the boundary layer does not appear significant except in the vicinity of δ_T, since the slow rate of ion-electron recombination and the sharp decrease of K_f with decreasing temperature allows for ion-electron number densities greatly in excess of equilibrium. As noted in section 3.4, atomic nitrogen and oxygen recombination occurs very rapidly. Hence, equilibrium values for <N> and <O> are assumed in the boundary layer. These were obtained with the help of reference 4 and are summarized in table V for M_s = 7.43, 9.88, and 10.43 at p_o = 1 cm.**

---

*To reduce the number of calculations we set s = 0 at various values of $y < \delta_s$ and solved equation (3.18), determining therefrom J as a function of s at each δ_s.

**The value for W depends on the rate constants given by equation (3.4) and the values for <N>, <O> and n. At $y = \delta_T$, $n = n_e$ refers to the equilibrium value. Equation (3.3) does not result in a precise value of W = 0 at $y = \delta_T$. In the calculations of equation (3.18), we set W = 0 when ion-electron formation exceeded recombinations; otherwise, the calculated value for W was used. Of course, due to the large boundary layer temperature gradient, ion-electron formation never exceeded recombination except possibly for very short distances from the edge of the boundary layer. The small error in the calculation of W causes small variations of s and J in the vicinity of δ_T which diminish rapidly with decreasing y and were always negligible for $y = \delta_s$.

Ion Diffusion—The evaluation of J requires the determination of the ion motion relative to the neutral gas due to ambipolar diffusion. No values are known to the author for ambipolar diffusion coefficients of NO^+ ion-electron pairs in air. However, because of the structural similarity between NO^+ and N_2, the ambipolar diffusion within the boundary layer should be approximately twice the value for self-diffusion of N_2. Computations of the latter are given in reference 22 for the temperature range 1,000 to 15,000° K. For comparison with these computations and in order to obtain values at lower temperatures, calculations were also made for twice the binary diffusion coefficient of NO in air, using the Lennard-Jones potential given in reference 23. In the notation of reference 23, it was assumed that

M_1 = 30 = molecular weight of NO

M_2 = 28 = molecular weight of partially dissociated air

T = absolute temperature, °K

p = pressure, atmospheres

$\sigma_{12} = \frac{1}{2}(\sigma_1 + \sigma_2) = 3.54$ Å, where $\sigma_1 = 3.47$ Å for NO and $\sigma_2 = 3.62$ Å for air

$\epsilon_{12}/\mathring{\kappa} = \sqrt{(\epsilon_1/\mathring{\kappa})(\epsilon_2/\mathring{\kappa})} = 107.3°$ K, where $\epsilon_1/\mathring{\kappa} = 119°$ K for NO and $\epsilon_2/\mathring{\kappa} = 97°$ K for air.

Substituting these values into equation (8.2 - 44) of reference 23, the value for twice the diffusion coefficient of NO in air is given by

$$D_a = 7.80\ (10^{-5})\ T^{1.5})/p_e\Omega \qquad (3.19)$$

where $\Omega = \Omega(\mathring{\kappa}T/\epsilon_{12})$ is the Lennard-Jones potential given in table I-M of reference 23 and p_e is the value for the pressure in the boundary layer.

Comparing the above calculations for NO in air with the tabulated values for self-diffusion of N_2 given in reference 22, the latter values are 15 percent larger at 6000° K, become equal at 2500° K, and become 5 percent smaller at 1000° K. Since this agreement was so close, equation (3.19) was used to evaluate the ambipolar diffusion coefficient for the entire boundary layer (exclusive of the sheath, where electrons are absent). The results of the calculations for $p_e D_a$ are given in table V as a function of temperature. D_a was obtained as a function of η for each M_s, since T is a known function of η and $p = p_e$ = constant.

Moreover, because the pressure is constant in the boundary layer, the value of $L_i/\sigma = D_a\rho/\mu$ is a function of temperature only.

However, L_i/σ varies only from 2.68 to 2.35 in the temperature range 300 to 5000° K. Thus, as previously stated, we may assume L_i/σ = constant in the solution for s in equation (3.18).

3.7 Ion Flow within the Sheath

The current measured by the probes is due entirely to ions, since the mean electron energy is only about 0.3 v and the electrode potential was always strongly negative, at least -6.1 v with respect to the plasma. Due to the negative probe bias, the electrode is enveloped within an NO^+ ion sheath. On account of the high ion density and the low electron energy, the transition region between the sheath and the neutral plasma is very narrow. As will be shown at the end of this section, the effect of electrons on the ion distribution and electric potential within the sheath is very small. In particular, ion-electron recombination within the sheath is negligible. Accordingly, the conservation equation for electrons may be dropped.

The amount of ion formation occurring within the sheath is negligible compared with the ion flow entering the sheath. This is due to (a) the slow rate of ion-electron recombination in the boundary layer, resulting in ion number densities entering the sheath that are considerably larger than those which would occur in an equilibrium flow and (b) the low ion-electron formation within the sheath, because of the low values of $\langle N \rangle$, $\langle O \rangle$, and K_f associated with the sharp reduction in the boundary layer temperature.

Within the sheath, the electric field and potential change rapidly from zero at the sheath edge; the potential decreases monotonically to the applied potential at the electrode, all potentials being referred to the plasma potential. However, in describing the effect on the ion velocity, it will be shown in section 4.1 that the nonuniformity of the field may be neglected, and the field is everywhere one of moderate strength. Accordingly, the ion motion will vary linearly with the electric field. We now proceed to derive the relations necessary to evaluate the electric potential and the ion current density in the sheath.

Taking into account the diffusion of ions due to the presence of the elctric field ϕ_y in the sheath, the conservation equation (3.9) for ions becomes

$$vs_y/P = (D_i s_y/P + sK\phi_y/P)_y \tag{3.20}$$

where W = 0 in the sheath, $s = c_i/c_{ie} = nP/n_e$, and $c_{ix} = 0$ due to symmetry in the thermodynamic properties at the stagnation point.

In equation (3.20), D_i refers to diffusion of the NO^+ ion through the dissociated air. The mobility and ion diffusion coefficients are related by

$$K = eD_i/\mathcal{R}T$$

or

$$K = 11{,}600\ D_i/T \tag{3.21}$$

D_i and K may be determined as functions of y for any given M_s since, by section 3.6 and table V, $D_i = D_a/2$ and D_a and T may be expressed as functions of y.

Poisson's equation for the electric potential is

$$\phi_{yy} = - en/\epsilon_o \tag{3.22}$$

As in section 3.6, the y component of the ion current density is defined by the equation

$$J = \bar{v}en \tag{3.23}$$

where now, for flow within the sheath, the y component of the average drift velocity of ions is

$$\bar{v} = - v + D_i s_y/s + K\phi_y \tag{3.24}$$

Equation (3.24) gives the relation between s and s_y.

Combining equations (3.20), (3.23) and (3.24), we obtain

$$J_y/en_e + s(v/P)_y = 0$$

Substituting the relations (3.11) and (3.16) for v and $dy/d\eta$, there results

$$J_y = 2\beta f_\eta\ en_e s/P \tag{3.25}$$

Except at the stagnation point where $f_\eta = 0$, $J_y > 0$.

It is of interest to show that the same relation (3.25) will be obtained if we start from the ion conservation equation in the form

$$(\rho_i ur)_x + (\rho_i \bar{v}r)_y = 0$$

where, as in section 3.5, $r = x$, $u = \beta x f_\eta$ and $n_x = 0$. Accordingly, we see that the loss in J on approaching the probe electrode is due to the gas mixture flow tangential to the probe surface, which causes a corresponding current outflow.

Finally, Poisson's equation (3.22) may be written

$$\phi_{yy} + \frac{10^{14}}{8.85}\frac{en_e s}{P} = 0 \tag{3.26}$$

The boundary conditions applied at δ_s are

(a) continuous s and J
(b) $\phi = \phi_y = 0$ (3.27)

Eliminating $\bar{v}$ in equations (3.23) and (3.24), there results

$$s_y = (1/D_i)\,[JP/en_e - sK\phi_y + vs] \tag{3.28}$$

The three equations (3.25), (3.26), and (3.28) are explicit expressions for the derivatives $(\phi_y)_y$, J_y, s_y in terms of ϕ_y, J, s. Hence, if initial values are given at one end of the interval, the derivatives can be calculated and a step-by-step numerical integration procedure is possible.

The sheath equations cannot be integrated from the sheath edge all the way to the wall, since integration in this direction is unstable and leads always to either positively infinite or negative values of s prior to reaching the wall. Hence, it is required to integrate from the wall to the sheath edge, and a matching procedure is necessary to satisfy the boundary conditions (3.27).

The boundary conditions at the wall can be given in either of two forms. For given J_w, ϕ_{yw} and s_w, assuming for instance $s_w = 0$ (catalytic wall), we can calculate the wall values of $(\phi_y)_y$, J_y and s_y and proceed at once as indicated in the step-wise numerical solution. If on the other hand J_w, ϕ_{yw} and s_{yw} are given, for instance $s_{yw} = 0$ (noncatalytic wall), equation (3.28) can be used to evaluate s_w. Then, the procedure is the same as in the first case.

In comparing the two cases (i.e., either $s_w = 0$ or $s_{yw} = 0$), it was observed that the results for ϕ_y, J, and s as functions of y were identical everywhere in the sheath, except in the vicinity of the wall for a distance of about 1 percent of the sheath thickness. Apparently, this means the quantity contained in the brackets on the right side of equation (3.28) became small, so that approximately

$$s\,\frac{en_e}{P} = \frac{J}{K\phi_y - v} \tag{3.29}$$

Accordingly, only the values of ϕ_{yw} and J_w were important. Thus, the integration for ϕ_y, J, and s from the wall to an assumed value for δ_s can be uniquely determined by the initial values for J_w and ϕ_{yw}.

To obtain a continuous s and J across the sheath, the following procedure was chosen. Values for (s_s, J_s) obtained from the solution of equation (3.18) were used as boundary conditions in the solution of the sheath equations, where now the latter integration was started at the sheath edge and in the direction of the wall. Although integration in this direction is unstable and can only be carried out for short distances from the sheath edge, the required (s_s, J_s) pair has a value of s_s that lies on the s(y) curve separating the previously mentioned two groups of positively infinite and negative s solutions. Hence, this procedure was very convenient for determining the (s_s, J_s) pair that satisfied the boundary conditions (3.27a).

Since the change in J through the sheath is small, values of J_w slightly smaller than J_s can be used. For each value of J_w, we may choose ϕ_{yw} and integrate the equations from the wall to the edge of the sheath. By properly adjusting ϕ_{yw} and J_w, we can obtain J_s and $\phi_{ys} = 0$ at $y = \delta_s$. At the same time, this procedure automatically insures the proper value of s_s.

In carrying out the calculations, $s_{yw} = 0$ was assumed. Since the reduction in J through the sheath never exceeded 5 percent of J_s, except for one or two adjustments of J_w, the matching procedure was reduced almost entirely to finding the ϕ_{yw} for which $\phi_{ys} = 0$.*

By equation (3.26), ϕ_y varies linearly with s and therefore, by equation (3.28) an increase in J_s results in an increase of s_s. Hence, the (s_s, J_s) pairs form a single curve for which $\partial J_s/\partial s_s > 0$. At each δ_s, the solutions of equation (3.18) resulted in a single curve $J_s(s_s)$ with a negative slope. Consequently, each solution of the ion flow through the boundary layer is single-valued and uniquely determined.

Finally, ϕ_w can be determined by a direct integration of ϕ_y, starting with $\phi_s = 0$. Thus, each δ_s gives a value for ϕ_w. Hence, a particular value of ϕ_w can always be found by adjusting δ_s, since ϕ_w decreases with decreasing δ_s. Accordingly, the curves for ϕ_y, J and s may be found as functions of y for a given ϕ_w. Moreover, using δ_s as a parameter, curves for $J_w(\phi_w)$ and $\phi_{yw}(\phi_w)$ may be obtained for $0 > \phi_w \geq -24$ v.

Electron Penetration of Ion Sheath—The electron penetration of the ion sheath, Δy, may be determined from the relation of the Debye shielding distance (ref 24).

*The solutions for the ion conservation equation (3.18) were obtained on an IBM 7090 computer and the solutions for the sheath equations were obtained on a PACE 131-R analog computer, manufactured by Electronic Associates Inc. The results of each computer were partially checked by making several complete sets of calculations on the other computer.

$$\Delta y = (kT/4\pi ne^2)^{\frac{1}{2}} = 6.90\ (T/n)^{\frac{1}{2}}\ \text{cm}$$

To determine whether the electron penetration is significant, we compare it with the total sheath thickness. For example, at $M_s = 7.43$ and $y = \delta_e = 36.5$ microns, figure 9a gives $\theta = 0.92$. Since $T_e = 3764$, $T_s = 3460$ K. As will be shown in section 4.1 for $\phi_w = -11.5$ v (fig. 14a), the corresponding $n_s = 2.34\ (10^{12})/\text{cm}^3$. Thus, the electron penetration is about 7.6 percent of the sheath thickness. Similarly, for $\phi_w < -2$ v, the electron penetration amounts to a small percentage of the sheath thickness at other values of δ_s and for other $M_s > 7.43$.

The electron penetration will reduce $|\phi_{yy}|$ in the neighborhood of $y = \delta_s$ and will thereby also modify s. However, for a given ϕ_w, this effect is essentially equivalent to increasing the sheath thickness by an amount smaller than the electron penetration. Thus, the effect of the electron penetration is small and will be neglected in the determination of the ion-electron boundary layer flow. In particular, the sharp rejection of electrons at the sheath edge results in the cessation of ion-electron recombination inside the sheath.

4. SOLUTIONS OF THE ION-ELECTRON BOUNDARY LAYER FLOW AND COMPARISON WITH MEASUREMENTS OF THE WALL ION CURRENT DENSITY

4.1 Exact Numerical Calculations

4.1.1 Discussion of Results

In accordance with the procedure given in section 3.7, exact numerical solutions of the equations for ion-electron boundary layer flow are presented for the condition of frozen atom flow ($W_j = 0$ through the boundary layer) at $M_s = 7.43$ and 10.43 and for equilibrium dissociated flow at $M_s = 9.88$. The calculations were carried out for the "free stream" and wall conditions given in table IV and the boundary layer values for $D_i = D_a/2$, $\langle N \rangle$ and $\langle O \rangle$ given in table V. These results are summarized in figures 10 through 14 for the 0.10- and 0.25-in. probes at $p_o = 1$ cm, $T_o = T_w = 300^\circ$ K and $-2 \leq \phi_w \leq -24$ v.

Calculations are also included to give the effects of uncertainty in the values for L_i/σ, n_e, K_r, and K_f. Although $L_i/\sigma = 2$ = constant was generally used in equation (3.18), as mentioned in section 3.6, L_i/σ varies between 2 and 3 in the boundary layer. Both microwave reflection measurements and magnetic probe measurements of dc conductivity to determine electron density in a shock tube (ref 5, 6, 25) have indicated equilibrium values for n somewhat larger than the theoretical values calculated from reference 4. In addition, reference 5 indicates that the rate constants K_f and K_r lie between the values given by equation (3.4) and three times these values. To evaluate the effect of these uncertainties, the calculations were repeated for $L_i/\sigma = 3$, the n_e values given in

table IV increased by a factor 2, and the K_f and K_r given by equation (3.4) each increased by a factor 3.* The repeated calculations are presented only at M_s = 7.43 and 10.43, since the results at M_s = 9.88 and 10.43 appeared to be similar because of the near quality in M_s.

When $n_e s$ instead of s is considered the variable in equations (3.25), (3.26) and (3.28), we see that $n_e s$ as a function of y in the sheath is independent of variations in the parameters L_i/σ, n_e, K_f, and K_r. According to equations (3.23) and (3.24), the sheath solutions for J(y) will also remain unchanged. However, by equation (3.18), changes will occur in the solutions for $J(n_e s)$ and J(s) outside the sheath. Hence, changes in the sheath calculations due to variation of the above parameters are brought about by the alteration of the boundary values for (s_s, J_s).

The changes in (s_s, J_s) can be determined approximately in the following way. The values of s and J as functions of y can be obtained by integration of equation (3.18), beginning the calculations with s = 0 at y = 0. As noted in section 3.7, the correct boundary conditions (s_s, J_s) are determined by a matching procedure involving the sheath equations. Consequently, the solution of equation (3.18) with s = 0 at y = 0 will generally not give the correct boundary values (s_s, J_s) for the solution of the sheath equations. However, the changes in (s, J) due to variations in L_i/σ, n_e, K_f, and K_r will be approximately the same as the changes in (s_s, J_s). In addition, we draw attention to the fact that the calculations showed that the variations in the curves $J_w(\phi_w)$ were mostly governed by variations in J_s and much less affected by variations of a similar amount in s_s. Here, for a given ϕ_w, J_w decreases with decreasing J_s.

Equation (3.18) was integrated with s = 0 at y = 0; figures 10 a and b show the resulting curves of s (dashed) and J (solid) as functions of y. The calculations were repeated for each of the following conditions:

(1) no variation of the parameters (▽),

(2) L_i/σ increased from 2 to 3 (◯),

(3) K_f and K_r each increased by the factor 3(□), and

(4) n_e increased by the factor 2 (▷).

As indicated, these parameters were varied one at a time. The symbols within parentheses identify the calculation condition for the curves given in figures 10 and 11. In figures 11 and 12, the open

*By equation (3.3), in order to have $W \approx 0$ at $y = \delta_T$, K_f was increased by the factor 4 when n_e was increased by the factor 2.

and solid symbols refer to the 0.25- and 0.10-in. probes, respectively.

It is important to keep in mind that the n_e and rate constant effects on J and s are interrelated. Thus, if recombination in the boundary layer is small, the curves s(y) and J(y) will be little affected by variation in the rate constants and the value of n_e will be important. In the other extreme, the two parameters have interchanged roles when the boundary layer recombination is large. In addition, since ion-electron recombination ceases at the sheath edge, the effect of a variation in the rate constants increases with decreasing sheath thickness.

According to figure 10a for $M_s = 7.43$, the variation in n_e will produce the largest change in J_s and thereby the largest change in the $J_w(\phi_w)$ curve. Moreover, as shown in figure 10a, increasing the rate constants reduces the J values, the percentage reduction of J increasing with decreasing δ_s. However, referring to figure 12a, $\delta_s > 20$ microns for $\phi_w < -4$v and $D_o = 0.25$ in. Hence, the effect of varying the rate constants will be significant only at small negative values of ϕ_w. Furthermore, according to figure 10a we may expect the variation in L_i/σ to have only a moderately small effect on the $J_w(\phi_w)$ curve. Thus, we see in figure 11a that the calculated curves $J_w(\phi_w)$ are in fact changed in accordance with the above changes shown in figure 10a. Apparently then, at low M_s, the ion-electron recombination in the boundary layer is small and the uncertainty in the calculations is most sensitive to the value of n_e.

At $M_s = 10.43$, we see by figure 12 a that $3 \leq \delta_s \leq 11$ microns when $-2 \geq \phi_w \geq -24$ v and $D_o = 0.25$ in. From figure 10b, we observe that the largest variation in J is due to varying the rate constants. Consistent with the previous remarks, there appears to be no effect on J due to varying n_e in figure 10b for the above range of δ_s. At any δ_s in this range, it is also seen that the s values for the curve (▽) are twice those of the curve (□). Since $n = n_e s/P$, this means that the n values of the two curves are identical. Apparently, since recombination is a function of n^2, at $M_s = 10.43$ we have a case of large boundary layer recombination so that the above two sets of calculations asymptotically attain equal values of J and n. To a lesser extent, the larger recombination occurring at higher M_s is a result of encountering larger variations in the boundary layer temperature and thereby larger variations in K_f, $\langle N \rangle$ and $\langle O \rangle$.

For $M_s = 10.43$, as for $M_s = 7.43$, we observe in figure 10b that the variation of L_i/σ should have a small effect on the $J_w(\phi_w)$ curves. Referring to figure 11c, we see that the above changes in the $J_w(\phi_w)$ curves are in fact as indicated by figure 10b. Consequently, at high M_s, the uncertainty in the calculations is most sensitive to the values for the rate constants.

By equations (3.11) and (3.16), since $\beta \propto 1/D_o$, reducing the probe size from 0.25 to 0.10 in. means an increase in the gas mixture velocity and a reduction in the boundary layer thickness each by a factor of $\sqrt{2.5}$. Hence, the amount of recombination will decrease with decreasing probe size because of the more rapid ion-electron transit through the region $\delta_T \geq y \geq \delta_s$. However, the values for $p_e = p_w$, T_e and T_w will remain unchanged. Therefore, n(y), s(y) and J(y) increase with decreasing D_o.

The calculations showed that the changes in the $J_w(\phi)$ curves for the 0.10-in. probe caused by variations in the above parameters were approximately the same as those for the 0.25-in. probe. In figure 11a for the 0.10-in probe at $M_s = 7.43$, we show only the calculations assuming (a) no variation of parameters and (b) a simultaneous increase in n_e by a factor 2 and increase in the rate constants by a factor 3. In figure 11c for the 0.10-in. probe at $M_s = 10.43$, we show only the calculations assuming (a) no variation of parameters and (b) an increase in the rate constants by a factor 3. These calculations give the approximate limits of the values of $J_w(\phi_w)$ due to uncertainty in the values of the above parameters.

The test measurements of J_w for the 0.25- and 0.10-in. probes are also given in figures 11a,b, and c. In each figure, the test measurements are given at $\phi_w = -6.1$, -11.5 and -22.3 v for the 0.25-in. probe and at $\phi_w = -11.5$ v for the 0.10-in. probe. In each figure, a dashed curve is drawn through the experimental points for the 0.25-in. probe. Evidently, as shown for $M_s = 7.43$ and 10.43, the test measurements fall within the limits of the uncertainty in the calculations obtained by the above variation of parameters. The calculation giving the best fit to the experimental data at $M_s = 7.43$ for both probe sizes corresponds to simultaneously increasing n_e by the factor 2 and increasing the rate constants by the factor 3. At $M_s = 10.43$, the best fit for the 0.25-in. probes is obtained by increasing the rate constants by the factor 3, whereas the best fit for the 0.10-in. probes corresponds to the case where the parameters are not varied. Within the experimental error, the comparison between the test measurements and the calculations at $M_s = 9.88$ is the same as that for $M_s = 10.43$. Because of the near equality in M_s, we may assume that the discussion for $M_s = 10.43$ also applies at $M_s = 9.88$.

For the condition where the parameters were not varied, the sheath thicknesses are given as functions of ϕ_w in figure 12a at the aforementioned M_s and D_o. By equation (3.26), for a given $y = \delta_s$, $|\phi_w|$ will increase with increasing $n = n_e s/P$. Since n is not in equilibrium in the boundary layer, n(y) increases with increasing M_s. We have already seen that n(y) is greater for the smaller probes. Accordingly, as shown in figure 12a, for a given ϕ_w we should expect δ_s to decrease with increasing M_s and decreasing D_o. Therefore, as

shown in figure 12b for a given ϕ_w, we should expect ϕ_{yw} to increase with increasing M_s and decreasing D_o.

The boundary layer thickness for the 0.25-in. probes is shown in figure 9 to be about 70 microns and independent of M_s. Therefore, the boundary layer thickness for the 0.10-in. probes is smaller by a factor of $\sqrt{2.5}$ and amounts to about 44 microns. A comparison of figures 9 and 12a shows that $\delta_s < \delta_T$ for $\phi_w \geq -24$ v at all M_s when $D_o = 0.25$ in. and at $M_s = 9.88$ and 10.43 when $D_o = 0.10$ in. However, at $M_s = 7.43$, δ_s extends fully to the edge of the boundary layer at $\phi_w = -24$ v when $D = 0.10$ in.

The numerical solutions of the complete boundary layer flow were obtained for $M_s = 7.43$, 9.88, and 10.43 with $D_o = 0.25$ and 0.10 in. at $\phi_w = -11.5$ v. The solutions for the flow outside the sheath are given in figures 13 a-f and the solutions for the flow within the sheath are given in figures 14a-f. The quantities J/J_T, s, n/n_e, v/v_T and v_D/v_{Ds} are given in figure 13 as functions of y from the boundary layer edge to the sheath edge and ϕ/ϕ_w, ϕ_y/ϕ_{yw}, n/n_s, s/s_s and s_y/s_{ys} are given in figure 14 as functions of y from the sheath edge to the probe wall.

As can be seen from figure 13 and as was previously noted, the reductions in J, n/n_e and s as functions of y increase with increasing M_s and increasing D_o due to the larger ion-electron recombination. In all calculations, we can observe the approximate linear variation of v with y and the rapid increase in the value of v_D in the neighborhood of the sheath edge. Accompanying the increase in v_D, a rapid change in $\partial J/\partial y$ near the sheath edge can be seen and here $\partial J/\partial y \approx 0$.

These changes in v_D and J near the sheath edge are not due to a sudden change in recombination but rather to the presence of the electric field within the sheath. The electric field causes a rapid acceleration of the ion flow within the sheath, thereby changing the values of s_s and J_s. In turn, the changes in the boundary conditions (3.27a) requiring continuous s and J across the sheath affects the entire boundary layer flow. For example, at $M_s = 7.43$, $D_o = 0.25$ in. and $\phi_w = -11.5$ v, figure 13a gives $\delta_s = 36.5$ microns, $s_s = 0.229$ and $J_s = 2.28$ ma/cm^2. Integrating equation (3.18) with $s = 0$ at $y = 0$ gives the minimum values of s(y) that can be obtained in the absence of an electric field. This was done in figure 10a for $M_s = 7.43$, where $s = 0.600$ and $J = 1.54$ ma/cm^2 at $y = 36.5$ microns. For this example, a comparison of the two cases shows that the electric field causes a reduction in s_s and an increase in J_s. The reduction in s_s is consistent with the increase in J_s for, as was mentioned in section 3 6, the solutions of equation (3.18) give curves for which $\partial J_s/\partial s_s < 0$.

In each figure 14, if the y scale is normalized by the given value of δ_s, the normalized solutions of the flow within

the sheath ϕ_y/ϕ_{yw}, ϕ/ϕ_w, n/n_s, s_y/s_{ys} and s/s_s as functions of y/δ_s appear to be independent of M_s and D_o. The sheath solutions for J are not given, since in the sheath J is constant to within 5 percent of J_s. The reason for the similarity in the normalized solutions may be seen from the approximate sheath equations given in section 4.2

$$s = JP/en_eK\phi_y \tag{4.1}$$

and

$$\phi_{yy} = -\frac{10^{14}}{8.85}\frac{J}{K\phi_y} \tag{4.3}$$

Assuming J and K are constant in the sheath, $\phi_y = \phi = 0$ at $y = \delta_s$, and $\phi_y = \phi_{yw}$ and $\phi = \phi_w$ at $y = 0$, successive integrations of equation (4.3) give

$$\phi_y/\phi_{yw} = (1 - y/\delta_s)^{1/2} \quad \text{and} \quad \phi/\phi_w = (1 - y/\delta_s)^{3/2}$$

Now, by equation (4.1), $s/s_w = (1 - y/\delta_s)^{-1/2}$. In each of figures 14, we see that $s_w/s_s \approx 0.07$. However, a good fit to the s/s_s curves is

$$s/s_s = 0.14(1-y/\delta_s)^{-1/2} \quad (\text{for } 0.1 < y/\delta_s < 0.98)$$

Furthermore, since $n = n_e s/P$, a good fit to the n/n_s curves is

$$n/n_s = sP_s/s_sP \approx 0.20\,(1-y/\delta_s)^{-1/2} \quad (\text{for } 0.2 < y/\delta_s < 0.96).$$

Near the wall, the factor (P_s/P) must be included.

Lastly, by differentiation of s/s_s and assuming $s_{yw}/s_{ys} = 0.012$

$$s_y/s_{ys} = 0.012\,(1-y/\delta_s)^{-3/2} \quad (\text{for } 0.1 < y/\delta_s < 0.95)$$

As previously noted, we find in figures 13 and 14 that n(y) increases with increasing M_s and decreasing D_o. Hence, in agreement with the previous results given in figures 12a and b, figures 14 show that δ_s decreases and ϕ_{yw} increases with increasing M_s and decreasing D_o.

4.1.2 New Technique for Evaluation of K_f and K_r

As was observed, the ion-electron flow behind the detached shock is sensitive to variations in a number of parameters. Because of this dependence, it may be possible to devise new techniques for improving our knowledge of some of these quantities. The following consideration illustrates a procedure for the determination of the ion-electron formation and recombination rate constants.

The flow model given in section 3.1 assumes $\delta_s < \delta_T$. However, a similar model will apply when $L_p > \delta_s \gtrsim \delta_T$, providing

the ion-electron and neutral gas quantities can be described at δ_s. This information can be obtained from a knowledge of the formation and recombination rate constants and the diffusion coefficient for ion-electron pairs in a manner similar to that for which n and v_D were calculated in the boundary layer in section 3.6. In addition, v can be found as described in section 3.5.

The electric field effects on the ion-electron flow can be varied by changing ϕ_w without altering the gasdynamic effects. Here, a change in ϕ_w results in a change in δ_s without altering δ_T or altering the flow of the neutral gas. In addition, both the gas mixture and the ion-electron flows will be changed by varying M_s, D_o and p_o. The latter variations will alter both δ_T and δ_s. By suitable variations of M_s, ϕ_w, D_o and p_o, the ion-electron flow can be altered by changing only the location of the sheath edge over a specified interval behind the detached shock when $L_p > \delta_s \lesssim \delta_T$.

Ion-electron recombination ceases for $y < \delta_s$ because of the absence of electrons in the sheath. Furthermore, since the equilibrium ion number density increases by a factor of more than 100 across the probe shock, until the ionization approaches or exceeds that for the equilibrium, recombination will be small in comparison with formation in the region $L_p \geq y \geq \delta_s$. Also recombination is small when the sheath edge is located sufficiently close to the detached shock. By varying ϕ_w and thereby δ_s, the resulting changes in J can be made highly sensitive to changes in the ion-electron formation rate. Furthermore, by varying M_s, we can alter the temperature behind the detached shock. Here, we affect the ion-electron formation since K_f varies sharply with temperature. The equilibrium constant, K_e, is known to within about 10 percent (ref 13), and the relation between the formation and recombination rate constants is given by $K_f = K_e K_r$. Consequently, for various locations of the sheath edge sufficiently close to the detached shock, we can determine the values of the ion-electron formation and recombination rate constants as functions of temperature which will bring the calculated and measured values of stagnation-point ion current density into agreement. This procedure may result in a more accurate determination of the rate constants, which are presently known only to within about a factor 3 (ref 5).

4.1.3 Validity of the Assumption $v_E = K\phi_y$

As noted in section 3.7, the calculations are based on the assumption that the ion velocity due to the electric field is given by $v_E = K\phi_y$. This relation is valid only in the event certain restrictions are satisfied. We now examine the numerical results to determine the validity of our use of this relation.

The linear dependence of v_E on ϕ_y does not hold for very strong electric fields. An indication of moderate field strengths

is that $\bar{v} \ll \bar{c}$, where $\bar{c}$ is the random thermal ion velocity (ref 26). Strong electric fields produce large values for v_E. Within the ion sheath, the ratio $\bar{c}/\bar{v}$ decreases from the sheath edge to the wall. At the wall, $T = 300^{o}$ K and therefore, $\bar{c} = 4.6 \times 10^4$ cm/sec. At the wall $\bar{v} \approx v_E$. For the range $0 \geq \phi_w \geq -24$ v and $M_s \leq 10.43$, the largest value for $v_{Ew} = 2.7 \times 10^4$ cm/sec, where $\phi_{yw} \leq 5.2 \times 10^4$ v/cm is given in figure 12b and K_w is given in table IV. Consequently, for the above ϕ_w and M_s range and with the possible exception of the immediate neighborhood of the electrode, $\bar{c}/\bar{v} \gg 1$, as required.

In order to be able to neglect the effect of the nonuniformity of the electric field on the ion mobility, it is necessary that the product $|\phi_{yy}\bar{L}| \ll |\phi_y|$, where $\bar{L}$ is the ion mean free path (ref 26). Except in the neighborhood of the sheath edge, equation (4.3) gives the approximate relation within the sheath

$$\phi_{yy} = -\frac{10^{14}}{8.85}\frac{J}{K\phi_y}$$

The values for $\bar{L}$ and K at the wall were previously calculated and are given in tables II and IV, respectively. The ratio $\bar{L}/K$ is nearly constant through the sheath, since both quantities vary essentially as $1/\rho$. Therefore, through the sheath the quantity $\phi_{yy}\bar{L}$ varies as $1/\phi_y$. Based on the J and ϕ_y values given in figures 11 and 12b, at the probe wall we obtain

$$|\phi_y| \geq 200|\phi_{yy}\bar{L}|$$

for $7.43 \leq M_s \leq 10.43$ and $\phi_w \leq -2$ v. Except for the region bounding the sheath edge, amounting to about 5 percent of the sheath thickness, the results of the exact calculations given in figures 14a-f show that $\phi_y \geq 0.1\ \phi_{yw}$. Hence, except in the neighborhood of the sheath edge, $|\phi_{yy}\bar{L}| \ll |\phi_y|$. Moreover, since both the region of the possible electric field nonuniformity and the value for ϕ_y within this region are small, a nonuniformity of the field appearing here will not seriously affect the ion mobility. Therefore, the conditions under which $v_E = K\phi_y$ is assumed are fully met and the use of this relation in the present calculations is fully justified.

4.2 Approximate Closed Form Solutions

In section 4.1, we required the use of electronic computers to obtain exact numerical solutions of the ion-electron boundary layer flow. Here, a simple procedure is given to determine the approximate ion-electron recombination in the boundary layer and the approximate values for J and n at the sheath edge. In addition, the exact sheath equations are simplified and numerical results for the flow within the sheath can be obtained from approximate closed form solutions. As

will be shown, the approximate solutions compare very well with the previous exact solutions and also yield values for J_w that are in close agreement with the test measurements.

We start by simplifying the exact sheath equations. First, we observe that $v_E \gg v$ within the sheath, except in the neighborhood of the sheath edge. Then, by equation (3.29), the approximate relation for s within the sheath is given by

$$s = JP/en_e K\phi_y \tag{4.1}$$

With the help of equation (4.1), equations (3.25) and (3.26) become

$$J_y = 2\beta f_\eta \frac{J}{K\phi_y} \tag{4.2}$$

and

$$\phi_{yy} = -\frac{10^{14}}{8.85}\frac{J}{K\phi_y} \tag{4.3}$$

From equation (4.2), we see that the change in J will be small for small sheath thicknesses. In all the calculations of section 4.1, the reduction in J through the sheath never exceeded 5 percent of J_s. Accordingly, we may neglect the variation of J and drop equation (4.2)

In order to integrate equation (4.3), the direction of y is reversed and it is assumed in equations (4.4) and (4.5) that y = 0 at the sheath edge and increases positively to $y = \delta_s$ at the probe electrode. Then for the conditions $\phi = \phi_y = 0$ at y = 0* and assuming J and K are constants, successive integrations of equations (4.3) result in equations

$$\phi_y = \frac{10^7}{2.10}\sqrt{\frac{Jy}{K}} \tag{4.4}$$

$$\phi = \frac{10^7}{3.15}\sqrt{\frac{Jy^3}{K}} \tag{4.5}$$

In equations (4.4) and (4.5), at the probe electrode

$$y = \delta_s,\ \phi = \phi_w,\ \phi_y = \phi_{yw} \text{ and } J = J_w$$

Numerical solutions of the sheath equations can be obtained when the value for J is known, since we can solve for $\phi_y(y)$, $\phi(y)$ and s(y) by using equations (4.4), (4.5) and (4.1). By definition and since J is practically constant in the sheath

$$J = J_s = \bar{v}_s e n_s \tag{4.6}$$

*At y = 0, the condition $\phi_y = 0$ leads to infinite ϕ_{yy} in equation (4.3). Hence, in the neighborhood of the sheath edge where $v_E = K\phi_y$ is small, the omission of the terms $(v + v_D)$ results in increased values for ϕ_{yy}; in turn, this results in numerically higher values for ϕ_y and ϕ. Elsewhere, $v_E \gg (v + v_D)$ and their omission is negligible. Accordingly, neglecting v and v_D in the sheath results in slightly larger values for ϕ_w, ϕ_{yw} and $\bar{v}_w$.

To evaluate v_s, reference must be made to the exact calculations given in section 4.1. Then, taking into account the ion-electron recombination in the region $\delta_s \leq y \leq \delta_T$, a value for J_s corresponding to a given ϕ_w can be obtained. The following presentation gives the details for the evaluation of J_s.

In figures 13, except near the sheath edge where the ion flow rapidly accelerates, it can be observed that $\bar{v}$ is nearly constant through the boundary layer. For each case, it can be assumed that this value of $\bar{v} \approx \bar{v}_s$. However, if possible, it would be preferable to express $\bar{v}_s$ in terms of the gas mixture velocity and calculate the latter from equation (3.11). In this way, an approximate method for evaluating $\bar{v}_s$ could be established without having to refer to the exact calculations. Accordingly, the exact calculations for $\bar{v}$ were compared with the approximate values for v_T, where the latter were calculated from equation (4.8) given below. It was found that approximately

$$\bar{v}_s = -2v_T \tag{4.7}$$

For the calculations given in the previous section, the validity of equation (4.7) appeared to be independent of both M_s and D_o.

To evaluate v_T, we have $\partial f/\partial\eta \equiv u/U \approx \theta \approx P$ from figure 9. Then from equation (3.11)

$$v_T = -(\sqrt{2\beta\rho_w\mu_w}/\rho_e) \int_0^\eta P d\eta$$

As indicated by figure 1 of reference 14, and in reference 27, $P \approx g$, where $g \equiv (h + u^2/2)/h_e$ and h is the enthalpy of the mixture. By figure 5 of reference 14 for equilibrium or frozen dissociated flows and as assumed in reference 1 for frozen flow, $g = 0.47\eta$ is a valid approximation for over 90 percent of the thermal boundary layer. The limit of integration is then $\eta = 2.1$ and

$$v_T = -\frac{1.04}{\rho_e}\sqrt{2\beta\rho_w\mu_w} \tag{4.8}$$

Moreover, as will be used later in this section, we see that $1/\rho \propto T \propto \eta \propto \sqrt{y}$, approximately.

Using the above result for $\int P d\eta$, the relation for the boundary layer thickness given by equation (3.16) becomes

$$\delta_T = \frac{1.04}{\rho_e}\sqrt{\rho_w\mu_w/2\beta} \tag{4.9}$$

As noted in section 3.6 ion formation in the boundary layer is small compared with reduction through recombination

Then, assuming recombination only in the region $\delta_s \leq y \leq \delta_T$, for K_r = constant, the integration of equation (3.3) yields

$$n_e/n_s = 1 + K_r n_e t \tag{4.10}$$

Here, $t = 0$ at $y = \delta_T$ and $n(t = 0) = n_e$.

The approximate ion transit time through the region $\delta_s \leq y \leq \delta_T$ is given by

$$t = (\delta_T - \delta_s)/\bar{v}_s \tag{4.11}$$

For given $\bar{v}_s$ and δ_T, the simultaneous solution of equations (4.5), (4.6), (4.10) and (4.11) yields approximate values for J, δ_s, t and n_s for a prescribed ϕ_w. Then, as previously noted for $0 \leq y \leq \delta_s$, equations (4.4), (4.5), and (4.1) can be solved for $\phi_y(y)$, $\phi(y)$ and s(y). To illustrate the procedure, solutions for δ_s, J_w and ϕ_{yw} will be given for the 0.25-in. diameter probes at p_o = 1 cm, $T_o = T_w = 300^o$ K, ϕ_w = -11.5 v, and M_s = 7.43, 9.88 and 10.43. In addition, the approximate sheath solutions are given for $\phi_y(y)$, $\phi(y)$ and s(y) at M_s = 9.88.

The approximate values for $\bar{v}_s$ and δ_T, shown in table VI, were calculated using equations (4.7), (4.8) and (4.9) and the "free stream" and wall conditions given in table IV. Dividing the $\bar{v}_s$ in table VI by 2, the resulting approximate v_T agree to within 10 percent of the exact values obtained in section 4.1 and given in figures 13.* As can be seen from figures 9 at the δ_T given in table VI, the exact values for θ are between 0.92 and 0.97 and the exact $\partial f/\partial \eta$ are between 0.96 and 0.98.** Thus, equation (4.9) adequately defines the edge of the boundary layer.

As will be seen from the calculations, $\delta_s \approx 0.25\ \delta_T$. As shown earlier, $1/\rho \propto T \propto \eta \propto \sqrt{y}$ approximately. Consequently, $\eta_s \approx 0.5\ \eta_T$ and $\rho_s \approx 2\rho_e$.*** The product of K and ρ does not appear to vary appreciably

* This agreement holds also for the 0.10-in. probes.

** Since the y scales in figures 9 and the δ_T in table VI are all reduced in value by the factor $\sqrt{2.5}$ in going from the 0.25- to the 0.10-in. probes, the above values for θ and $\partial f/\partial \eta$ also result for the latter probes.

***By neglecting changes in Z, we introduce an error in ρ_s not exceeding 10 percent.

with temperature (ref 26). Using equation (3.21) and the values for $D_a = 2D_i$ given in table V, to within a factor of 1.6 it may be assumed that $K = 6.0/\rho$ cm^2/v-sec in the sheath, where ρ is in kg/m^3. Since $1/\rho \propto \sqrt{y}$, an average gas density within the sheath will be assumed as $\bar{\rho} = (2\rho_s + \rho_w)/3$, and the corresponding value for K is $\bar{K} = 6.0/\bar{\rho}$.

By table IV, T_e is between 3764 and 6036°K for $7.43 \leq M_s \leq 10.43$. Since $T_s \approx T_e/2$ and reference 5 gives $K_r = 3 \times 10^{-3}/T^{1.5}$, $K_r = 10^{-8}$ cm^3/ion-sec was assumed for the entire region $\delta_s \leq y \leq \delta_T$.

The results of the calculations for J_w are summarized in table VI. Within the uncertainty in the values for n_e and K_r, it was previously noted in section 4.1 that the exact calculations gave values for J_w equal to the experimental measurements. Assuming the measured J_w are representative of the exact calculated values, table VI shows that the approximate calculations for J_w are smaller and within 30 percent of the measured values. However, since the approximate calculations for the J_w are all smaller, and considering the approximate nature of equation (4.7), the above comparison could be improved by increasing the coefficient in equation (4.7) from 2 to 2.3. In this way, the approximate values for J_w would be within 13 percent of the test measurements. To this same end, K_r and n_e could be modified within the limits of uncertainty noted in section 4.1

The exact solutions of δ_s and ϕ_{yw} given in figures 12a and b for $\phi_w = -11.5$ v at $M_s = 7.43$ differ by as much as 40 percent from the approximate values given in table VI. However, the agreement between the exact and approximate values of these quantities is much closer at $M_s = 9.88$ and 10.43. Moreover, the exact calculations for δ_s are larger at all M_s.

The ion-electron recombination in the region $\delta_s \leq y \leq \delta_T$ is indicated by the ratio n_e/n_s. As shown in table VI, the approximate values of n_e/n_s are smaller than those given for the exact calculations.

Since the J_w for the two sets of calculations are nearly equal, the higher n_e/n_s for the exact calculations is mainly due to the previously noted rapid acceleration of the ion flow near the sheath. As in section 4.1, here we also find n_e/n_s and therefore the ion-electron recombination is small at $M_s = 7.43$ and increases significantly with increasing M_s. Assuming the values for T_s and ρ_s obtained in section 4.1, the corresponding equilibrium values for n_s were calculated using reference 4. As shown in table VI, both the exact and approximate values for n_s are larger than those for equilibrium, and these differences increase sharply with increasing M_s.

In figure 15, a comparison is made of the approximate (dashed curves) and the exact (solid curves) solutions for ϕ_y, ϕ and s through the sheath for $M_s = 9.88$ with $D_o = 0.25$-in. at $\phi_w = -11.5$ v. Here, the curves are all drawn so that y = 0 represents the wall. In the approximate calculations, use is made of equations (4.4), (4.5) and (4.1) and the single value $K = \bar{K} = 0.980$ throughout the sheath in equations (4.4) and (4.5). For the calculation of s, since $P = \rho_e/\rho$, $K = 6.0/\rho$, and $J = 31.0$ ma/cm^2, equation (4.1) reduces to $s = 20.3/\phi_y$. Except near the sheath edge where $\phi_y \to 0$ and due to the difference between the exact and approximate values of δ_s, the two sets of calculations for ϕ_y, ϕ and s agree to within a factor 2.

Finally, we can compare the previous results of the exact calculations for all M_s and ϕ_w with the results that can be obtained from the approximate sheath equations (4.4) and (4.5). Since $J \approx$ constant in the sheath, equations (4.4) and (4.5) give $\phi_y \propto \sqrt{y}$ and $\phi \propto y^{1.5}$. Approximately, these are the functional dependencies shown in figures 14 when allowance is made for the variation in temperature and therefore K through the sheath, particularly near the wall where K rapidly decreases.

Also, as may be seen from figure 6, both J and the ratio ϕ_w^2/J increase with increasing ϕ_w and therefore, by equation (4.5), δ_s increases with increasing ϕ_w. By equation (4.5), doubling ϕ_w provides an increase in δ_s by a factor less than $2^{2/3} = 1.59$. This result is in agreement with the exact solutions for $\delta_s(\phi_w)$ shown in figure 12a.

Furthermore, combining equations (4.4) and (4.5), we see that $\phi_y \propto (J\phi)^{1/3}$. According to figure 6, $0 < \partial J_w/\partial \phi_w < 1$. Hence, doubling ϕ_w will result in an increase in ϕ_{yw} by a factor between 1.26 and 1.59. This result is in agreement with the exact solutions for $\phi_{yw}(\phi_w)$ given in figure 12b.

5. SUMMARY AND SUGGESTIONS FOR FURTHER STUDY

A model of the ion-electron flow in the stagnation region between the detached shock and the wall of a Langmuir-type probe is proposed in section 3.1 for ionized air at ion mass fractions less than 10^{-4}. Based on the close agreement between numerical calculations and experimental shock tube measurements of ion current density at the stagnation point of the probe, it can be concluded that the proposed model gives an accurate description of the ion-electron flow in the stagnation-point boundary layer when negative potentials are applied at the probe stagnation point. Although this was not done in the present work, these solutions can also be extended to cover the entire stagnation region behind the detached shock, since the ion-electron formation and flow velocity can be determined in this region by the method given in section 3.6.

The flow model given in section 3.1 assumed $\delta_s < \delta_T$ and the model is valid for restricted ranges of M_s, ϕ_w, D_o and p_o. The present study is well within these limits and covers the ranges $7 < M_s < 11$ and $-2 \geqq \phi_w \geqq -24$ v with $D_o = 0.10$ and 0.25 in. at $p_o = 1$ cm. A similar flow model will apply when $L_p > \delta_s \geqq \delta_T$, and solutions of the ion-electron flow can again be obtained in the entire stagnation region behind the detached shock.

In the shock tube, the ion-electron number density increases across the detached probe shock by a factor exceeding 100, and this increase does not depend on the state of the undisturbed incident ionized flow. Hence, in the shock tube, the ion-electron flow ahead of the probe shock cannot be determined. However, when ion-electron formation and recombination due to the presence of the body does not greatly exceed the number density in the undisturbed flow, we can trace the ion-electron flow from a point in the undisturbed incident flow to the stagnation point of the probe. An example of this situation can arise for flight at high altitudes.

Although the present work refers to a Langmuir-type probe in the form of a flat-headed circular cylinder with an electrode located at the stagnation point of the incident flow, in principle, the probe may have any geometry for which at least at one point (the probe electrode) the gas mixture and ion-electron flows can be determined. Thus, it may be possible to determine the ion-electron distributions in the stagnation region of any axially symmetric blunt body and in the boundary layers of conical bodies and flat plates. Accordingly, it would be of interest to repeat the above calculations and shock tube measurements for these types of bodies, thereby contributing to the further understanding of ion-electron boundary layer flows.

The ion-electron flow behind the detached shock has been shown in section 4.1 to be sensitive to a number of physical properties, such as D_a, D_i, K, K_r and K_f. Because of this dependence, it may be possible to extend the present work and develop procedures to improve the accuracy to which some of these properties are known. An example of such a procedure is given in section 4.1 for the determination of the ion-electron formation and recombination rate constants.

The procedure given to obtain numerical solutions is of special interest, since the one-dimensional Poisson equation for the electric potential is joined with the usual gasdynamic stagnation-point boundary layer equations for the dissociated neutral gas mixture. Since the ion mass fraction is less than 10^{-4}, the latter equations are not affected by the presence of the charged particles or by their formation or recombination. Hence, solutions for the electric potential and the ion-electron number and current densities can be readily obtained.

However, at higher levels of ionization, the enthalpy and the flow of the gas mixture will be affected by ion-electron formation and recombination. In addition, for sufficiently large ionization, Coulomb forces will increase the cross section of ions for

collisions between charged particles and thereby tend to modify the values of $\mathcal{L}$, D_i and μ. The calculation comparing the energy for ion-electron formation with the gas mixture total enthalpy are given on page 15 and the calculations for the effect of Coulomb forces are given in appendix A. From these calculations, it appears that ion-electron formation and recombination effects on the gas mixture enthalpy as well as Coulomb effects on the boundary layer diffusion of ions and electrons will become significant at ion mass fractions exceeding about 10^{-2}. In a shock tube, for a given probe, the fractional ionization increases primarily with increasing M_s.

On the experimental side, the conductivity of the gas increases with increasing M_s and the gas may provide an additional conducting path between the probe electrode and the shock tube wall. This effect may result in erroneously larger values of the probe measurements. A procedure to determine when the gas conductivity affects the measurements was given on page 6. Hence, both the calculation and experimental procedures will require modification at large ion mass fractions.

Finally, the present study can be extended to other gases where the ionization process leads to positive ions of a single type and electrons only. To date, no attempt has been made to treat flows consisting of other types of charged particles.

6. REFERENCES

(1) Talbot, L., Theory of the Stagnation-Point Langmuir Probe, Physics of Fluids, Vol 3, No. 2 pp. 289-298, March-April 1960.

(2) Brundin, C. L., Talbot, L., and Sherman, F. S., Flow Studies in an Arc Heated Low Density Supersonic Wind Tunnel, Univ of Calif Inst of Engineering Research Report HE-150-181, April 15, 1960.

(3) Talbot, L., Katz, J. E., Brundin, C. L., A Comparison between Langmuir Probe and Microwave Electron Density Measurements in an Arc Heated Low Density Supersonic Wind Tunnel, Univ of Calif Inst of Engineering Research Report HE-150-186, Jan 27, 1961.

(4) Hilsenrath, J., Klein, M., and Woolley, H. W., Tables of Equilibrium Properties of Air and Nitrogen Including Second Virial Corrections from 1,500 to 15,000° K, National Bureau of Standards Publication (In press).

(5) Lin, S. C., and Teare, J. D., Rate of Ionization behind Shock Waves in Air. II. Theoretical Interpretation, Avco Research Report 115, Sept 1962.

(6) Lin, S. C., Ionization Phenomena of Shock Waves in Oxygen-Nitrogen Mixtures, Avco Research Report 33, June 1958.

(7) Loeb, L. B., Fundamental Processes of Electrical Discharge in Gases, John Wiley and Sons Inc., 1939, p. 242.

(8) Feldman, S., Hypersonic Gas Dynamic Charts for Equilibrium Air, Avco Research Lab, 1957.

(9) Hansen, C. F., Approximations for the Thermodynamic and Transport Properties of High-Temperature Air, NASA TR R-50, 1959.

(10) Moeckel, W. E., Approximate Method for Predicting Form and Location of Detached Shock Waves Ahead of Plane or Axially Symmetric Bodies, NACA TN 1921, 1949.

(11) Francis, G., Ionization Phenomena in Gases, Academic Press Inc, 1960.

(12) Gaitatzes, G., and Bloom, M. H., On the Interior of Normal Shocks According to Continuum Theory, Including Rate Thermochemistry, Polytechnic Inst of Brooklyn, ARL 65, June 1961.

(13) Wray, K. L., Chemical Kinetics of High Temperature Air, International Hypersonics Conference, M.I.T., Cambridge, Mass., Aug 16-18, 1961.

(14) Fay, J. A. and Riddell, F. R., Theory of Stagnation Point Heat Transfer in Dissociated Air, Avco Research Report 1, April 1957. Also, Journal of the Aeronautical Sciences, Vol 25, No. 2, pp. 73-85, Feb 1958.

(15) Lees, L., Convective Heat Transfer with Mass Addition and Chemical Reactions, Third Agard Colloquim, Combustion and Propulsion, pp. 454-455, 467, Pergammon Press, 1958.

(16) Stoney, W. E., Jr. and Markley, J. T., Heat Transfer and Pressure Measurements on Flat-Faced Cylinders at a Mach Number of 2, NACA TN 4300, July 1958.

(17) Chones, A. J., Heat-Transfer and Pressure Measurements on Flat-Faced Flared-Tail Circular Cylinders and Normal Disks, NAVORD Report 6669, 15 June 1959.

(18) Stoney, W. E., Jr., and Swanson, A. G., Heat Transfer on a Flat-Face Cylinder in Free-Flight at Mach Numbers up to 13.9, NACA RM L57E13, June 1957.

(19) Cooper, M. and Mayo, E. E., Measurements of Local Heat Transfer and Pressure on Six 2-Inch Diameter Blunt Bodies at a Mach Number of 4.95 and at Reynolds Numbers per Foot up to 81 x 10^8, NASA Memo 1-3-59 L, March 1959.

(20) Boison, J. C. and Curtiss, H. A., An Experimental Investigation of Blunt Body Stagnation Point Velocity Gradient, American Rocket Society Journal, pp. 130-5, Feb 1959.

(21) Rose, P. H. and Stark, W. I., Stagnation Point Heat-Transfer in Dissociated Air, Journal of the Aeronautical Sciences, Vol. 25, No. 2, pp. 86-97, Feb 1958.

(22) Amdur, I. and Mason, E. A., Properties of Gases at Very High Temperatures, Physics of Fluids, Vol 1, No. 5, pp. 370-83, Sept-Oct 1958.

(23) Hirschfelder, J. O., Curtiss, C. F., and Bird, R. B., Molecular Theory of Gases and Liquids, John Wiley and Sons, Inc, 1954.

(24) Spitzer, L., Jr., Physics of Fully Ionized Gases, Interscience Pubs. Inc., 1956.

(25) Tevelow, F. L. and Curchack, H. D., Microwave Diagnostics in the Shock Tube, Proceedings of the 1962 Army Science Conference, U.S. Military Academy, West Point, N. Y., Vol II, pp. 349-62 (see fig. 9), 20-22 June 1962.

(26) Von Engle, A., Ionized Gases, Oxford Univ Press, 1955.

(27) Cohen, C. D. and Reshotko, E., Similar Solutions for the Compressible Laminar Boundary Layer with Heat Transfer and Pressure Gradient, NACA TN 3325, 1955.

(28) Burgers, J. M., Statistical Plasma Mechanics, Symposium of Plasma Dynamics, Addison-Wesley Pub Co., 1960, Edited by F. H. Clauser.

(29) Chapman, S. and Cowling, T. G., The Mathematical Theory of Non-Uniform Gases, Cambridge Univ Press, 1960.

ACKNOWLEDGMENT

I wish to express my appreciation to Prof. J. M. Burgers of the University of Maryland for his valuable suggestions and counsel throughout the course of this work; to J. Hilsenrath of NBS for making available prior to publication the thermodynamic data given in reference 4; to the authors of reference 14 and N. Kemp of the AVCO Research Laboratory for providing the numerical data on page 19; to L. Joseph and A. Hausner for help in preparing and carrying out the computer calculations; to H. Curchack for help in obtaining the shock tube measurements, and to M. Bradley for help in designing and constructing the test section and probes.

APPENDIX A. THE EFFECT OF COULOMB FORCES ON $\bar{L}$, D_i AND μ

In the preceding determinations for $\bar{L}$, D_i and μ, collisions between neutral particles and between ions and neutral particles were based on particles treated as hard elastic spheres. For sufficiently large ionization, Coulomb forces will increase the cross section of ions for collisions between charged particles and thereby tend to modify the values of the above quantities. The effect of Coulomb forces will be shown to increase with increasing M_s and be greatest at the edge of the thermal boundary layer. In the following calculations, reference will be made to the case for $M_s = 10.43$ for the corresponding "free stream" conditions at $y = \delta_T$ given in table IV. As will be shown, the effect of Coulomb forces on the quantities $\bar{L}$, D_i and μ may be neglected for $M_s \leq 10.43$.

By equation (5-63a) of reference 28, the assumption of binary collisions is valid when the dimensionless parameter

$$\underline{\lambda} = \hbar T/e^2(2n_e)^{1/3} \gg 1$$

where the subscript e refers to conditions at the edge of the boundary layer. The present calculation gives $\underline{\lambda} = 21.6$, and we therefore assume binary collisions in the following calculations.

Mean Free Path—By page 149 of reference 28, assuming only collisions between the charged particles and Coulomb forces, the ion mean free path at $y = \delta_T$ is

$$\overline{L_e} = (2\sqrt{2}\ \underline{Z} n_e)^{-1}$$

where, by equations (5-20) to (5-22) of reference 28, the collision cross section is

$$\underline{Z} = Z_{st} = Z_{st}^{(11)} = 2\sqrt{\pi}\ (e^2/\hbar T)^2\ \ln \Lambda$$

with

$$\Lambda = \frac{3\hbar T}{e^2}\left[\frac{\hbar T}{8\pi n_e e^2}\right]^{1/2}$$

For our case, $\ln \Lambda = 4.45$, $\underline{Z} = 1.210\ (10^{-12})$ cm^2 and $\bar{L}_e = 1.260\ (10^{-4})$ cm. By the calculations of section 3.3, which are summarized in table II, the ion mean free path with the neutral particles can be expected to be $\bar{L}_e < 10^{-5}$ cm at $M_s = 10.43$ for $p_o = 1$cm and to be smaller toward the wall. Hence, $\bar{L}_e$ is governed by collisions between the ions and neutral particles.

The ratio $n:\langle N_g \rangle$ decreases within the thermal boundary layer due to ion-electron recombination and due to ion acceleration within

the sheath. Moreover, this ratio decreases with decreasing M_s, (table IV). Hence, we may conclude that $\bar{L}$ is governed by collisions between ions and neutral particles for the entire flow field at $M_s \leq 10.43$.

Diffusion Coefficient—For diffusion, the collision cross section for molecules treated as hard elastic spheres may be obtained from equations (5-19) of reference 28 as

$$\underline{Z} = Z_{st}^{(11)} = 4\sqrt{\pi}\,\sigma_{12}^2$$

where σ_{12} is the average diameter of the colliding molecules. As noted in section 3.6, $\sigma_{12} = 3.54$ Å and therefore $\underline{Z} = 8.89 \times 10^{-15}$ cm^2. The "first approximation to the diffusion coefficient" is given on page 245 of reference 29 as

$$[D_{12}]_1 = \frac{3}{2}\left[\frac{\mathscr{R}T}{2\underline{\mu}}\right]^{\frac{1}{2}} \frac{\sqrt{\pi}}{\langle N_g \rangle \underline{Z}}$$

where

$$\underline{\mu} = m_1 m_2/(m_1 + m_2)$$

m_1 = mass of neutral particle = 4.65×10^{-23} g

m_2 = mass of NO^+ ion = 4.99×10^{-23} g

For the "free stream" conditions at the edge of the boundary layer given in table IV at $M_s = 10.43$, there results $[D_{12}]_1 = 2.08$ cm^2/sec. This compares with the diffusion coefficient of $64.572/(15.57) = 2.07$ cm^2/sec, obtained from table V. (In table V, values are given for ambipolar diffusion of NO^+ ion-electron pairs in air, which were assumed to be equal to twice the binary diffusion coefficient of NO in air, see page 22, and the factor $15.57 = p_e$).

The effect of Coulomb forces on D_i, like that for $\bar{L}$, depends on the product $\langle N_g \rangle \underline{Z}$. Since the mean free path between charged particles is more than a factor 10 greater than the mean free path between ion and neutral particles, we see that the effect of Coulomb forces on the diffusion coefficient is negligible.

Viscosity Coefficient—The coefficient of viscosity for a pure gas is given by equation (10.21,1) of reference 29 as

$$\mu = \frac{5}{2}\,\frac{(\mathscr{R}Tm)^{\frac{1}{2}}}{Z^{(22)}}$$

where m = molecular mass and $Z^{(22)}$ = collision cross section. Treating molecules as hard elastic spheres, $Z^{(22)} = 8\sqrt{\pi}\,\sigma_{12}^2 = 1.778 \times 10^{-14}$

cm^2 for the neutral particles. Assuming ions subject to Coulomb forces only, equation (5-22) of reference 28 gives $Z^{(22)} = 2\ Z^{(11)} = 2.60 \times 10^{-12}$ cm^2 for the ions. Since the temperature and mass of the ions and neutrals are approximately equal, the ratio of the viscosity of a gas consisting of ions to that of a gas consisting of neutral particles is about 1:150, or the inverse ratio of their collision cross sections.

The "first approximation to the coefficient of viscosity" of a gas mixture is given by equation (12.5,1) of reference 29 in the following form

$$[\mu]_1 = \frac{n_{12}\left[\frac{2}{3} + \frac{m_{1A}}{m_2}\right] + n_{21}\left[\frac{2}{3} + \frac{m_{2A}}{m_1}\right] + \frac{E}{2[\mu_1]_1} + \frac{E}{2[\mu_2]_1} + \frac{4}{3} - 2A}{\frac{n_{12}\left[\frac{2}{3} + \frac{m_{1A}}{m_2}\right]}{[\mu_1]_1} + \frac{n_{21}\left[\frac{2}{3} + \frac{m_{2A}}{m_1}\right]}{[\mu_2]_1} + \frac{E}{2[\mu_1]_1[\mu_2]_1} + \frac{4A(m_1 + m_2)^2}{3Em_1m_2}}$$

where, for the notation of reference 29, $[\mu_1]_1$ and $[\mu_2]_1$ are the above "first approximations to the coefficients of viscosity" of the constituent neutral and ion gases, respectively, $n_{12} = n_1/n_2$, $n_{21} = n_2/n_1$, $n_1 = \langle N_g \rangle_e$, $n_2 = n_e$, and where A and E are quantities depending only on the interaction of molecules of different kinds. For hard elastic spheres, pages 172-3 of reference 29 gives A = 0.4. By page 230 of reference 29, the quantity

$$E = \frac{2}{3}(n_1 + n_2)(m_1 + m_2)[D_{12}]_1 = 2.53 \times 10^{-3}\ g/cm\text{-}sec$$

where $[D_{12}]_1 = 2.08$ cm^2/sec is the previously calculated "first approximation to the coefficient of diffusion" of the ion and neutral particles. Substituting numerical values into the above equation, there results

$$[\mu]_1 = [\mu_1]_1 = 8.76 \times 10^{-4}\ g/cm\text{-}sec$$

The quantities n_{21} and E decrease with decreasing M_s, so that the equality remains between $[\mu]_1$ and $[\mu_1]_1$. Moreover, n_{21} decreases in the boundary layer due to ion-electron recombination and ion acceleration within the sheath due to the electric field. Also, E decreases in the boundary layer approximately as $\sqrt{T}$. Thus, the effect of Coulomb forces on the viscosity coefficient is negligible for all $M_s \leq 10.43$.

TABLE I

FLOW TIME FROM DETACHED PROBE SHOCK TO OUTER EDGE OF THERMAL BOUNDARY LAYER FOR 0.25-IN.DIAMETER PROBES

M_s	p_o cm Hg	v_1 m/sec	$M_1=v_1/a_1$	L_p cm	v_2 m/sec	p_e atm.	ρ_e kg/m^3	β 10^5/sec	δ_T micron	t 10^{-8} sec
7	1.0	2080	2.14	0.254	561	4.78	0.445	1.14	49.6	17.8
8	1.0	2400	2.33	0.227	580	7.05	0.540	1.26	46.8	15.2
9	1.0	2750	2.52	0.212	624	10.10	0.625	1.41	45.6	13.1
10	1.0	3120	2.66	0.206	690	13.80	0.710	1.56	45.2	11.4
9	0.2	2750	2.60	0.208	595	2.16	0.140	1.39	95.7	10.8
10	0.2	3120	2.74	0.204	661	2.96	0.157	1.50	96.6	9.41

TABLE II

ION MEAN FREE PATH WITHIN BOUNDARY LAYER

M_s	p_o cm Hg	p_e atm	T_e ^oK	$\langle N_g \rangle_e$ 10^{19}/cm^3	$\bar{L}_e$ micron	$\bar{L}_w$ micron
7	1.0	4.78	3570	0.985	0.182	0.0153
8	1.0	7.05	4090	1.27	0.142	0.0104
9	1.0	10.10	4770	1.56	0.115	0.00725
10	1.0	13.80	5670	1.79	0.100	0.00530
9	0.2	2.16	4560	0.348	0.516	0.0340
10	0.2	2.96	5420	0.402	0.446	0.0246

TABLE III

TIME REQUIRED TO ATTAIN EQUILIBRIUM IONIZATION

M_s	p_o cm Hg	$\langle N \rangle_e$ $10^{16}/cm^3$	$\langle O \rangle_e$ $10^{18}/cm^3$	n_e $10^{14}/cm^3$	K_f $\frac{10^{-16}\ cm^3}{ion\text{-}sec}$	t_f 10^{-6} sec
7	1.0	0.121	0.922	0.0340	0.930	32.8
8	1.0	1.01	2.21	0.294	2.70	4.87
9	1.0	7.50	4.01	2.16	8.05	0.891
10	1.0	57.6	5.37	13.0	21.6	0.195
9	0.2	2.07	1.03	0.468	6.02	3.66
10	0.2	15.6	1.28	2.87	16.9	0.849

TABLE IV

"FREE STREAM" AND WALL CONDITIONS
WITH D_o = 0.25 in. AND p_o = 1 CM HG

M_s	p_e atm	θ_w	T_e °K	ρ_e kg/m³	ρ_w kg/m³	K_w $\frac{cm^2}{v\text{-}sec}$	n_e $10^{14}/cm^3$	$\langle N \rangle_e$ $10^{16}/cm^3$
7.43	5.70	0.0797	3764	0.485	6.49	1.425	0.0840	0.289
9.88	13.30	0.0538	5580	0.701	15.60	0.611	11.16	45.0
10.43	15.57	0.0497	6036	0.740	18.10	0.522	23.2	95.4

M_s	$\langle O \rangle_e$ $10^{16}/cm^3$	$\langle N_g \rangle_e$ $10^{19}/cm^3$	β 10^5/sec	$-v/fP$ cm/sec	$y/\int_o^\eta P d\eta$ cm
7.43	1.38	1.11	1.20	1108	0.00462
9.88	5.22	1.75	1.54	1345	0.00437
10.43	5.80	1.90	1.60	1400	0.00437

TABLE V

EQUILIBRIUM <N> AND <O> AND AMBIPOLAR DIFFUSION COEFFICIENT

		M_s = 7.43		M_s = 9.88		M_s = 10.43	
T	$p_e D_a$	<N>	<O>	<N>	<O>	<N>	<O>
10^3 °K	cm^2/sec	$1/cm^3$	$10^{17}/cm^3$	$1/cm^3$	$10^{17}/cm^3$	$1/cm^3$	$10^{17}/cm^3$
6.0	63.9					8.89 $(10)^{17}$	58.2
5.5	55.4			3.74 $(10)^{17}$	52.6	4.04	60.6
5.0	47.3			1.43	51.6	1.54	59.6
4.8	44.2			0.914	50.6	0.990	57.4
4.6	41.2			0.564	47.5	0.611	53.6
4.4	38.2			0.333	43.0	0.361	48.3
4.2	35.4			0.187	37.4	0.203	41.5
4.0	32.7			98.9 $(10)^{14}$	30.7	0.107	33.9
3.8	30.0			48.9	24.1	52.9 $(10)^{14}$	26.4
3.6	27.4	14.5 $(10)^{14}$	10.7	22.2	17.3	24.0	18.9
3.4	25.0	5.99	7.40	9.20	11.8	9.95	12.7
3.2	22.6	2.20	4.73	3.37	7.38	3.66	8.00
3.0	20.2	0.706	2.77	1.08	4.28	1.17	4.63
2.8	18.1	0.191	1.47	0.292	2.25	0.316	2.44
2.6	16.0	42.1 $(10)^{11}$	0.690	64.4 $(10)^{11}$	1.06	69.6 $(10)^{11}$	1.14
2.4	14.0	7.15	0.283	11.0	0.433	11.9	0.468
2.2	12.1	0.874	0.0971	1.34	0.148	1.45	0.161
2.0	10.3	0.0698	0.0266	0.105	0.0407	0.116	0.0440
1.8	8.65						
1.6	7.06						
1.4	5.67						
1.2	4.41						
1.0	3.27						
0.8	2.25						
0.6	1.39						
0.4	0.696						
0.3	0.420						

TABLE VI

APPROXIMATE SOLUTIONS OF THE SHEATH EQUATIONS FOR THE 0.25-IN. PROBES AT ϕ_w = - 11.5 V

M_s	$\bar{K}$	$\bar{v}_s$	δ_T	δ_s	t	ϕ_{yw}	Approx (sec 4.2) J_w	Measured J_w
	$\frac{cm^2}{v/sec}$	cm/sec	micron	micron	10^{-6} sec	v/cm	ma/cm^2	ma/cm^2
7.43	2.14	2230	48.0	21.9	1.17	7,960	2.73	3.12
9.88	0.980	2800	45.4	7.49	1.35	23,200	31.0	35.9
10.43	0.855	2910	45.4	6.92	1.32	25,000	34.1	50.8

M_s	n_e	Exact Solution (sec 4.1)			Approx (sec 4.2)	Equilibrium
		T_s	ρ_s	n_e/n_s	n_e/n_s	n_e/n_s
	$10^{14}/cm^3$	^oK	kg/m^3			
7.43	0.0840	3226	0.592	3.58	1.098	6.14
9.88	11.16	3242	1.424	34.4	16.10	473
10.43	23.2	2837	1.907	45.0	31.7	11,400

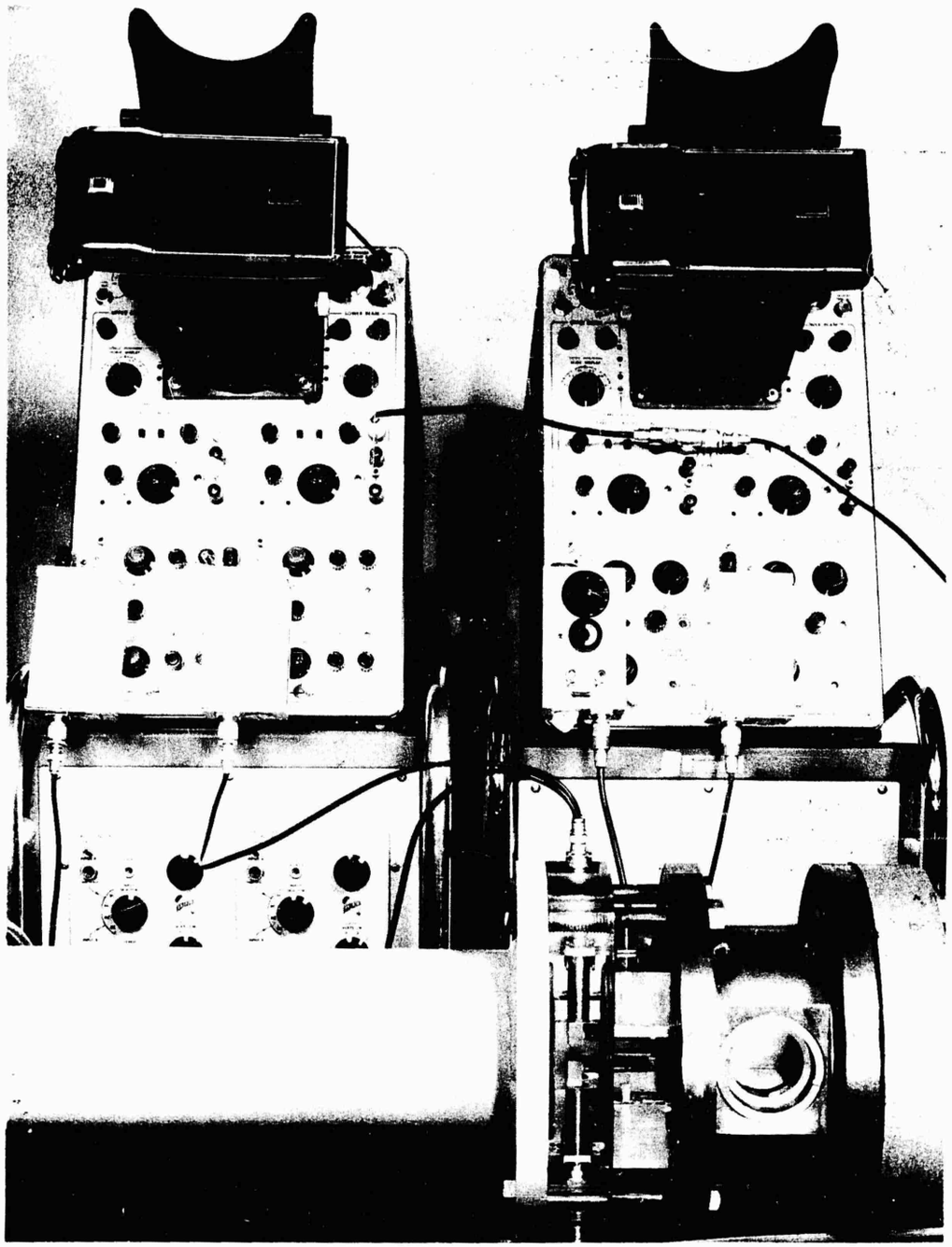

884-62

Figure 1. Installation of the probes in the shock tube. The four probes are shown mounted in the 2-in. thick plexiglas section. A second plexiglas section shown adjacent to this section was not used during the test measurements. In the background are the two Tektronix 555 dual beam oscilloscopes and the miniboxes housing the mercury cells and resistor.

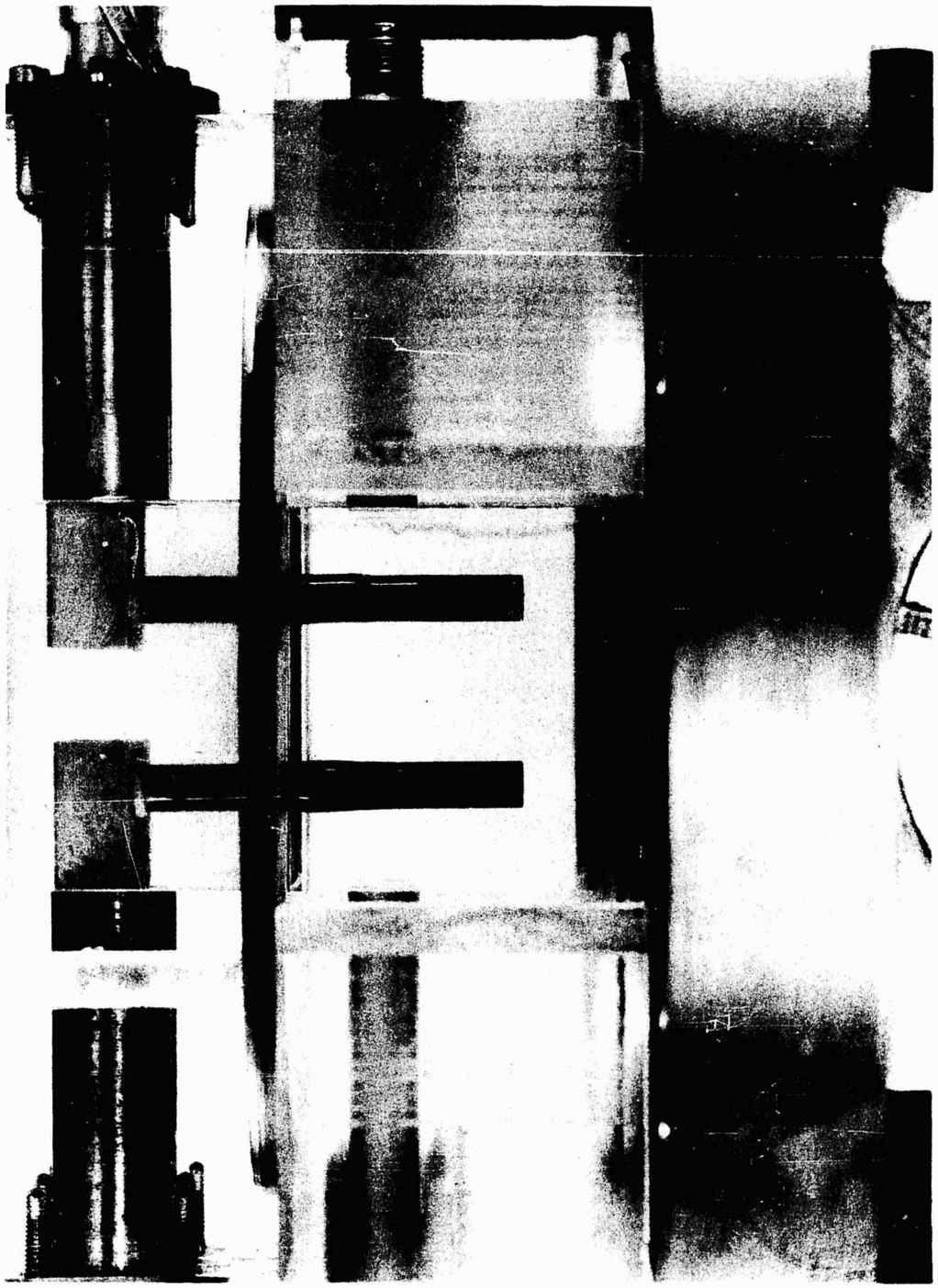

883-62

Figure 2. Close view of the probe installation.

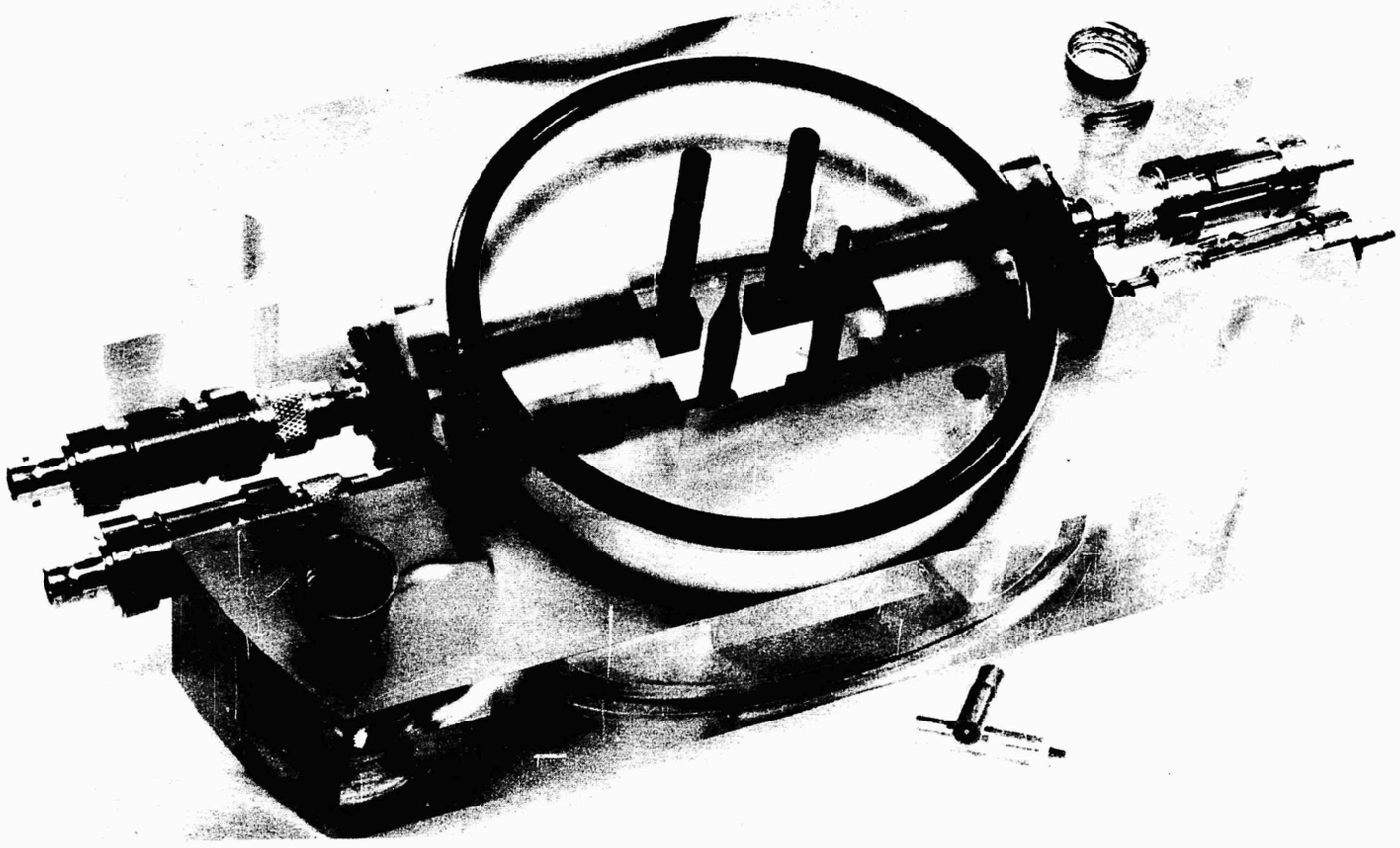

628-62

Figure 3. Probes and plexiglas test section. Two each 0.25- and 0.10-in. diameter glass insulated probes are mounted in the section and two brass probes are shown in the foreground.

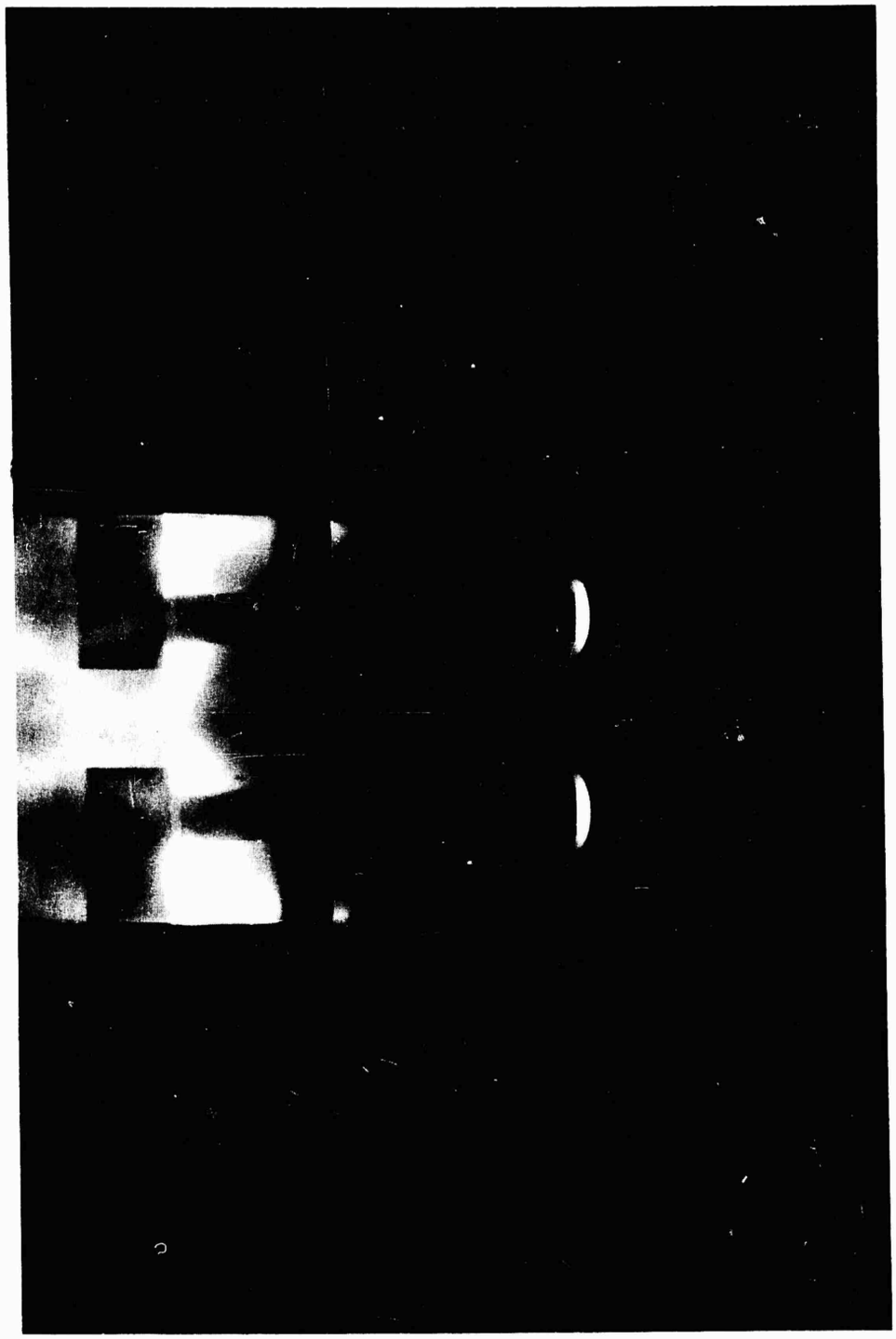

882-62

Figure 4. Typical flow about the probes in air, M_s=9 and P_o=0.5 cm hg. Illumination of the hot gas caused the film exposure.

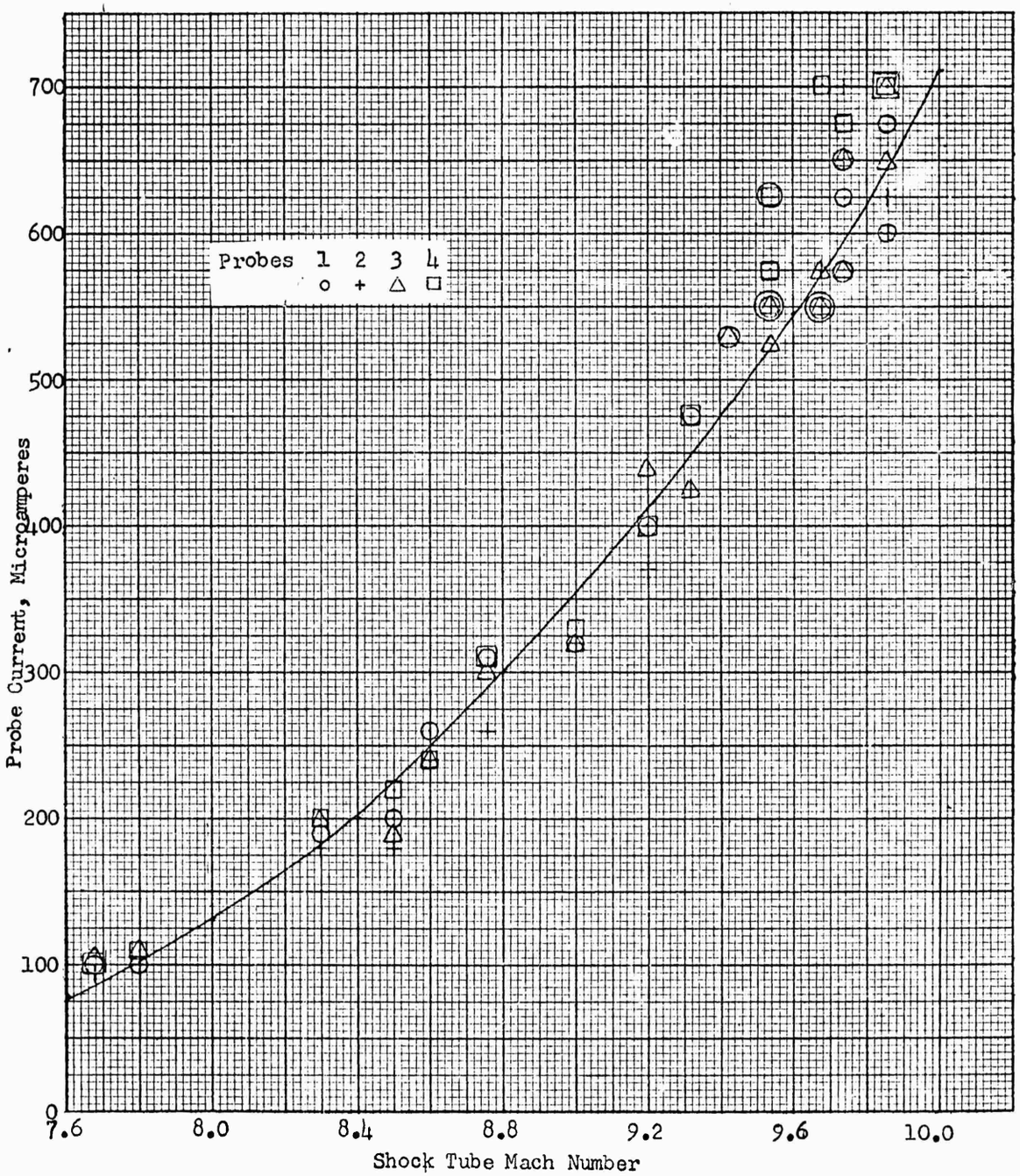

Figure 5. Probe current vs. shock tube Mach number for four 0.25 inch diameter probes with 0.060 inch electrodes. ϕ_p = -10.8 volts.

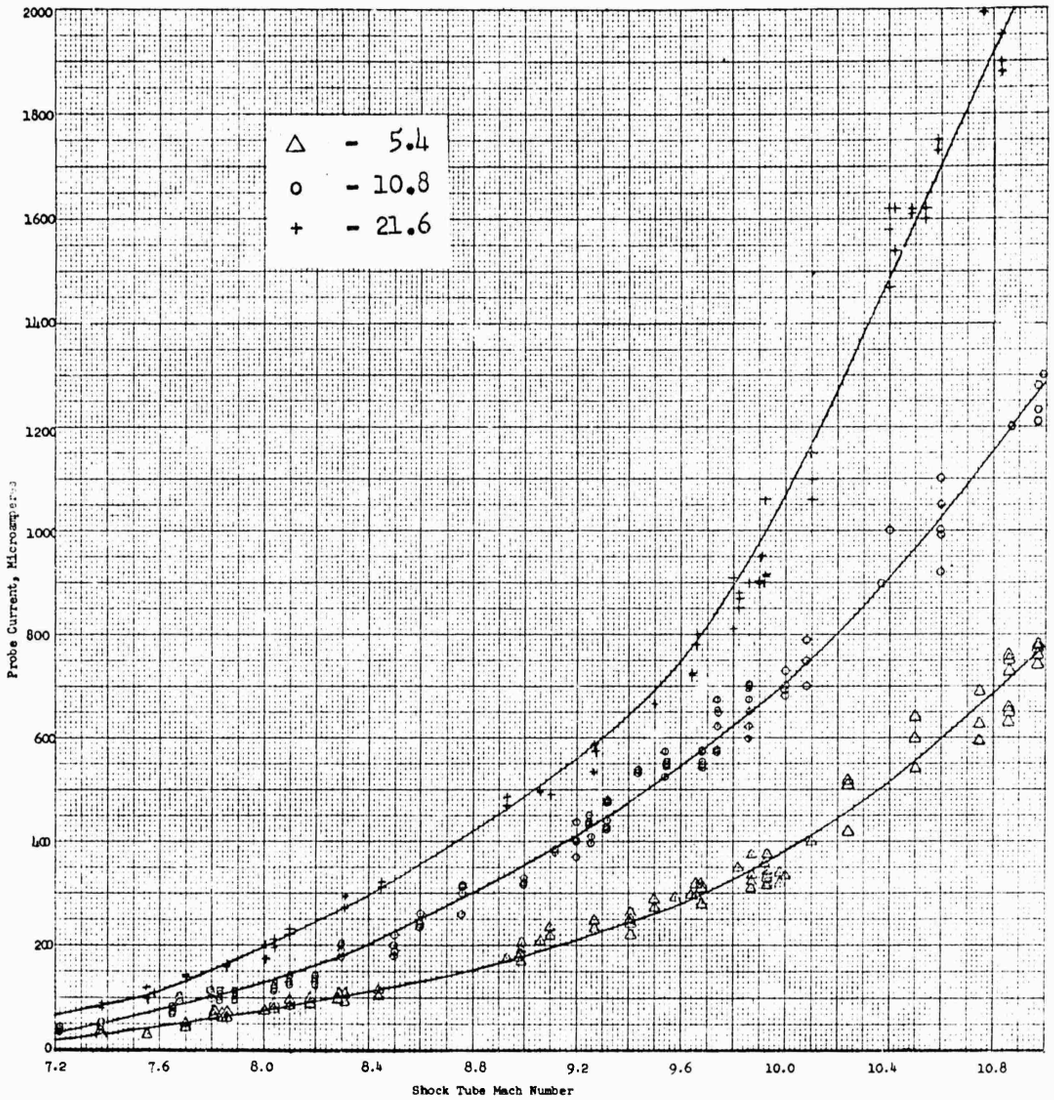

Figure 6. Probe current vs. shock tube Mach number for 0.25 inch diameter probes with 0.060 inch electrodes. ϕ_p = -5.4, -10.8 and -21.6 volts.

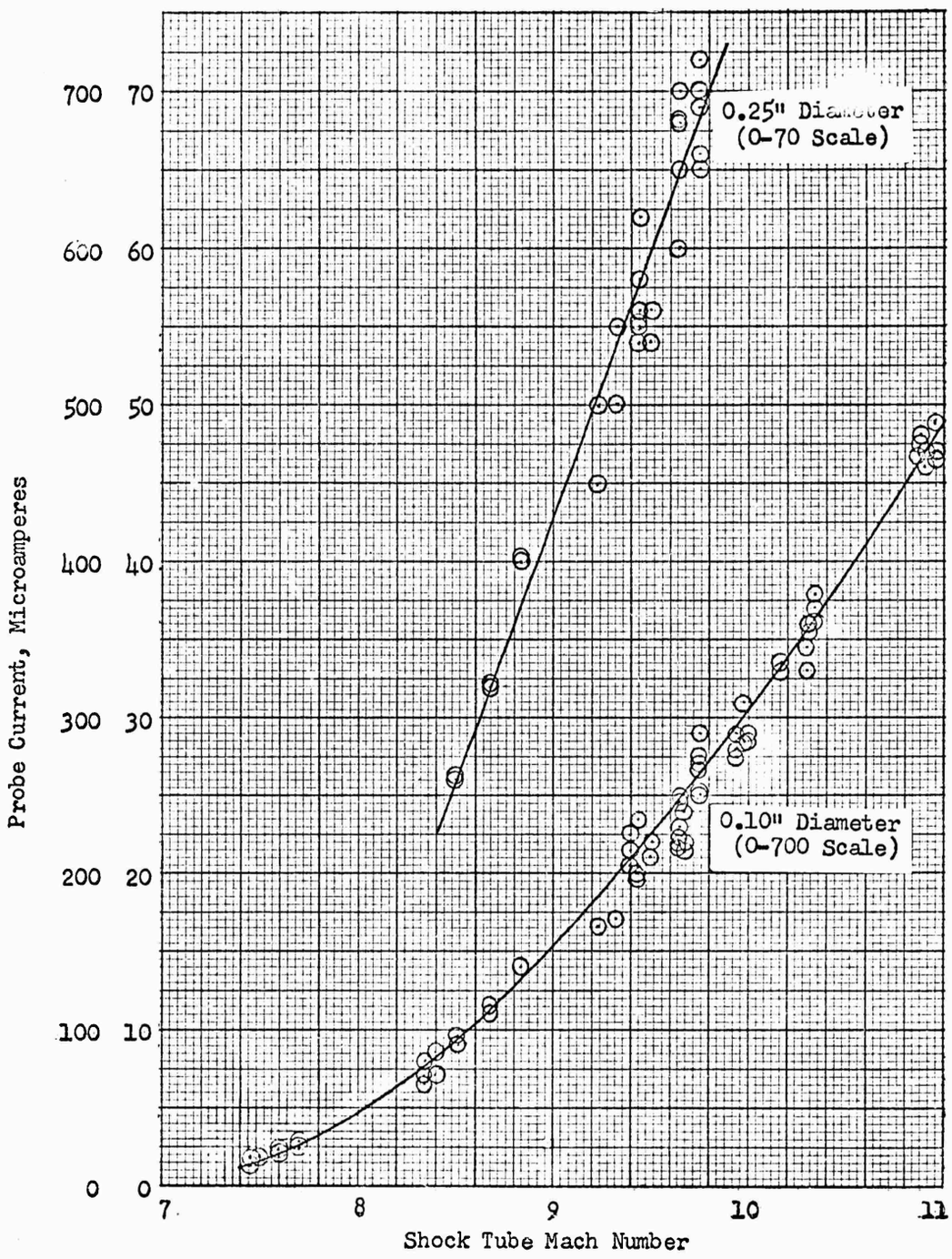

Figure 7. Probe current vs. shock tube Mach number for 0.25 and 0.10 inch diameter probes with 0.020 inch electrodes. ϕ_p = -10.8 volts

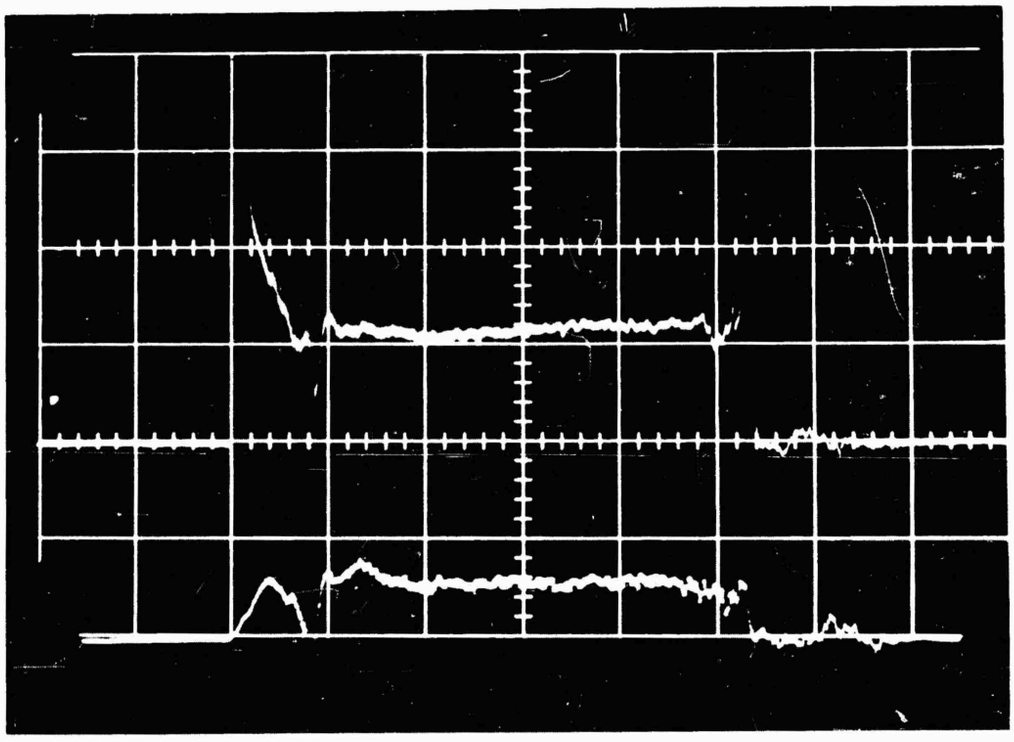

1014-62

Figure 8. Typical oscilloscope traces. Upper trace is typical for the flatheaded probes and lower trace is typical for the conical probes. Time traces left to right at 20 μsec per division.

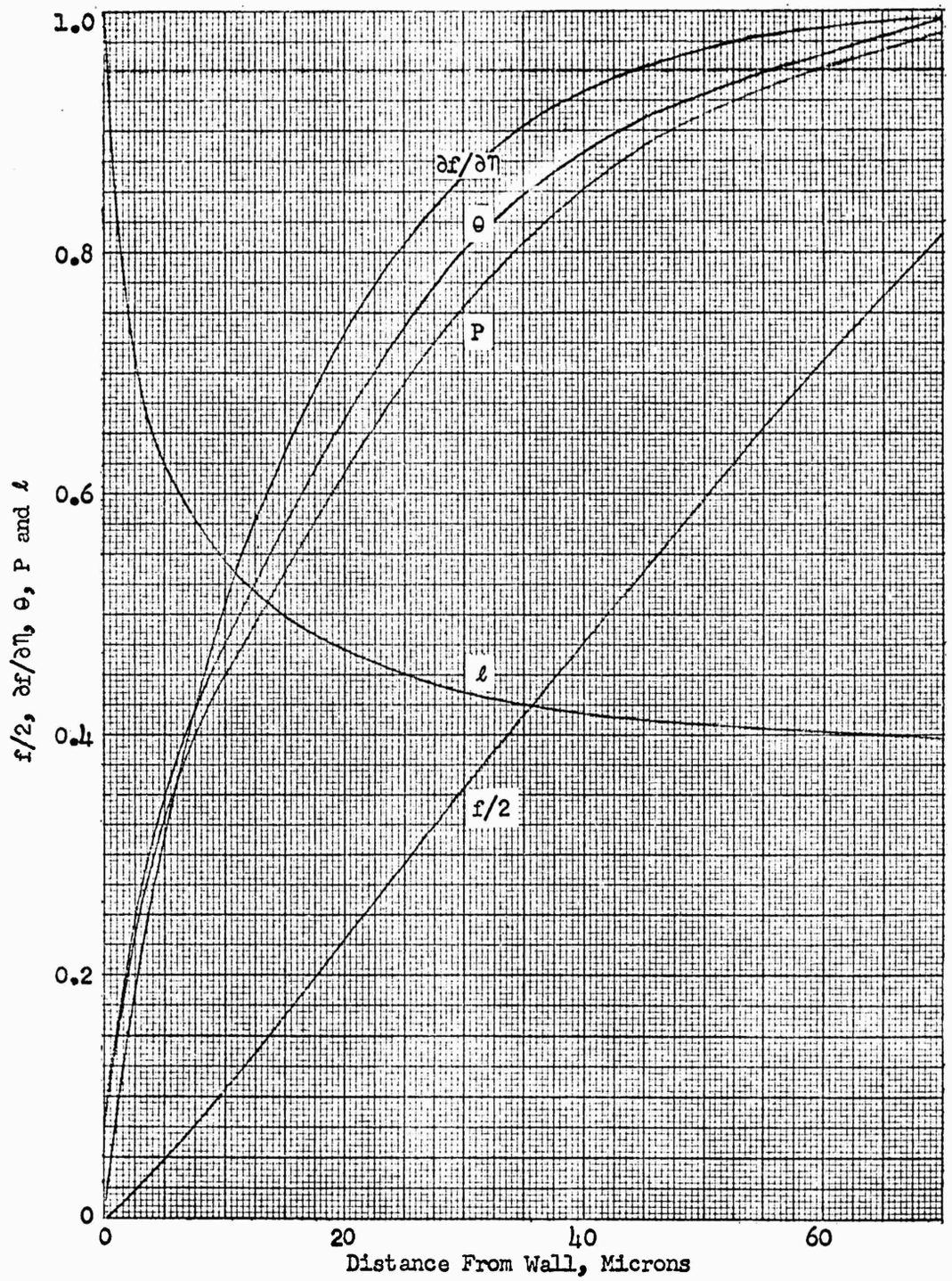

Figure 9a. Variation of f, $\partial f/\partial \eta$, θ, P and ℓ through the boundary layer at $M_s = 7.43$ for the 0.25 inch diameter probes.

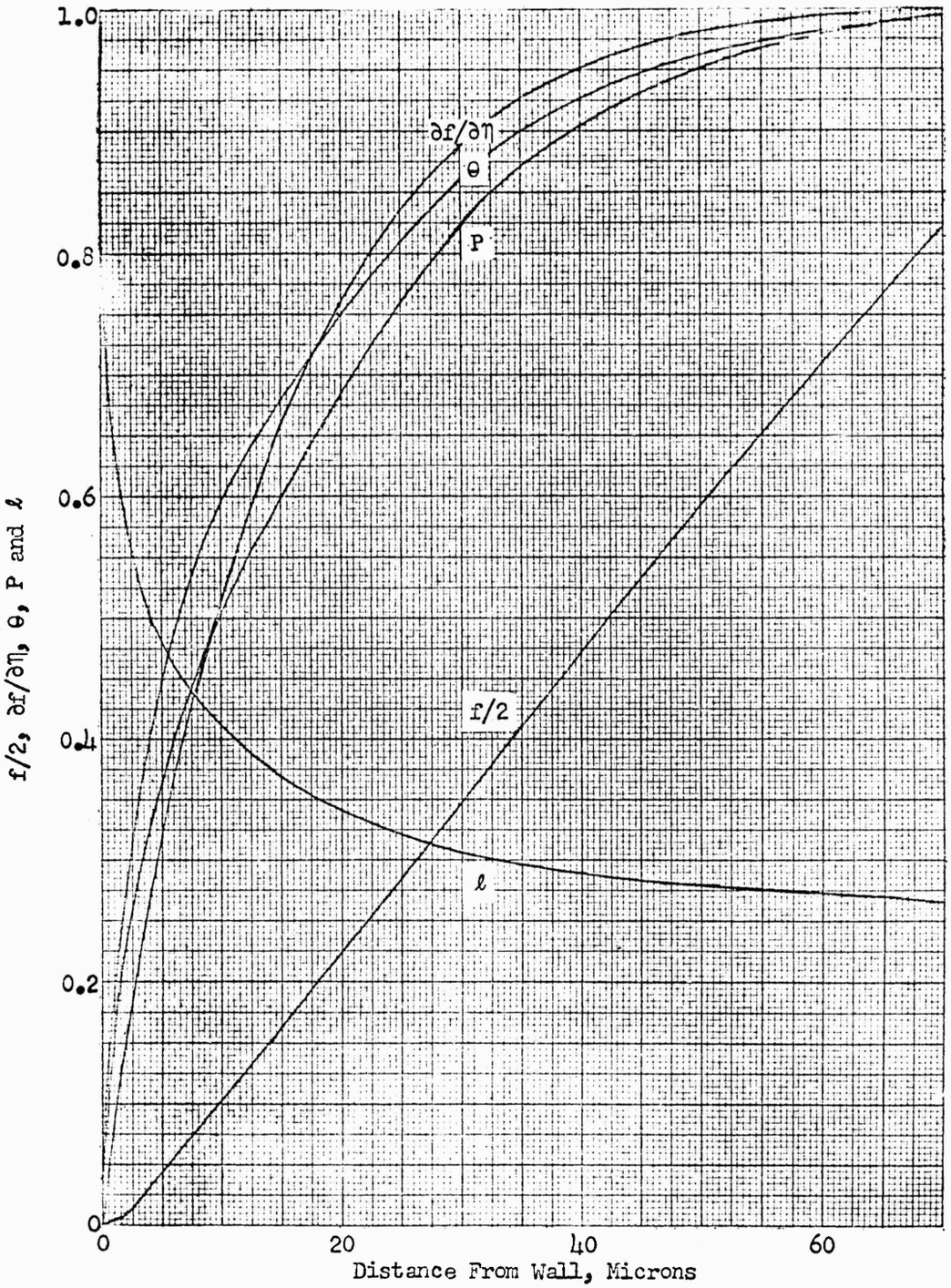

Figure 9b. Variation of f, $\partial f/\partial \eta$, θ, P and ℓ through the boundary layer at $M_s = 9.88$ for the 0.25 inch diameter probes.

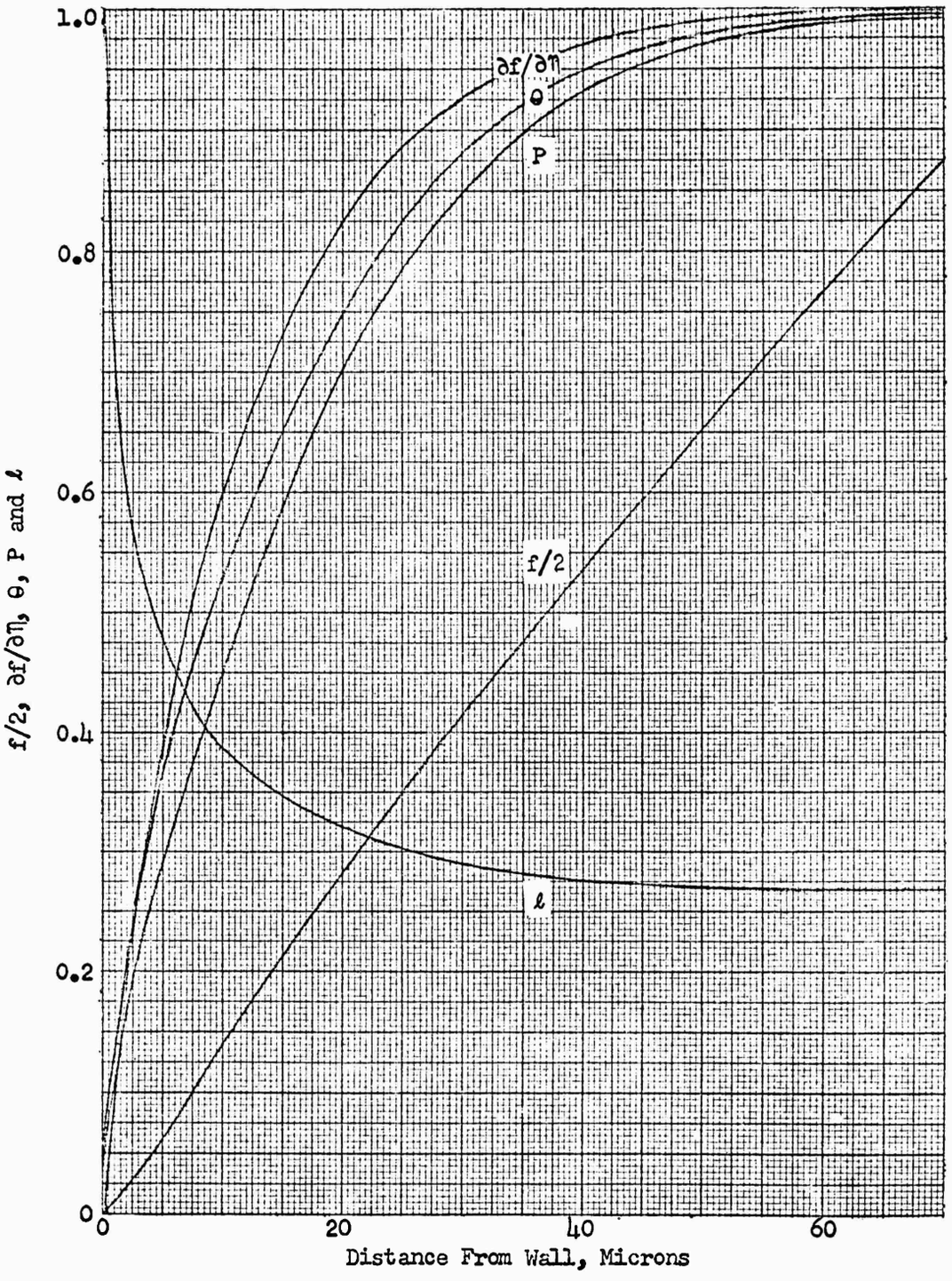

Figure 9c. Variation of f, $\partial f/\partial \eta$, Θ, P and ℓ through the boundary layer at $M_s = 10.43$ for the 0.25 inch diameter probes.

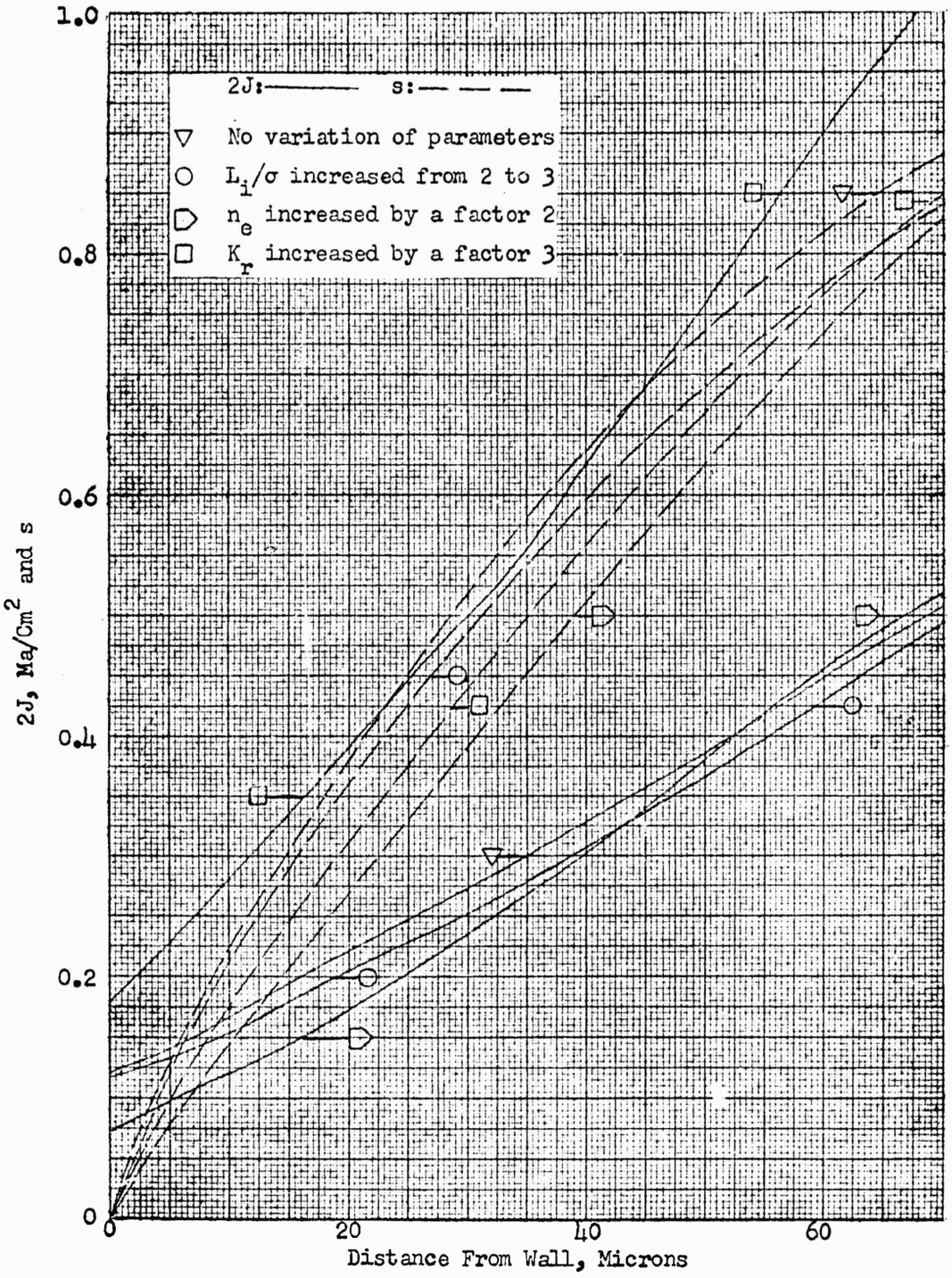

Figure 10a. Effects of L_i/σ, n_e, K_f and K_r on the variation of J and s through the boundary layer for the 0.25 inch probes at $M_s = 7.43$. Calculation is for $s = 0$ at $y = 0$.

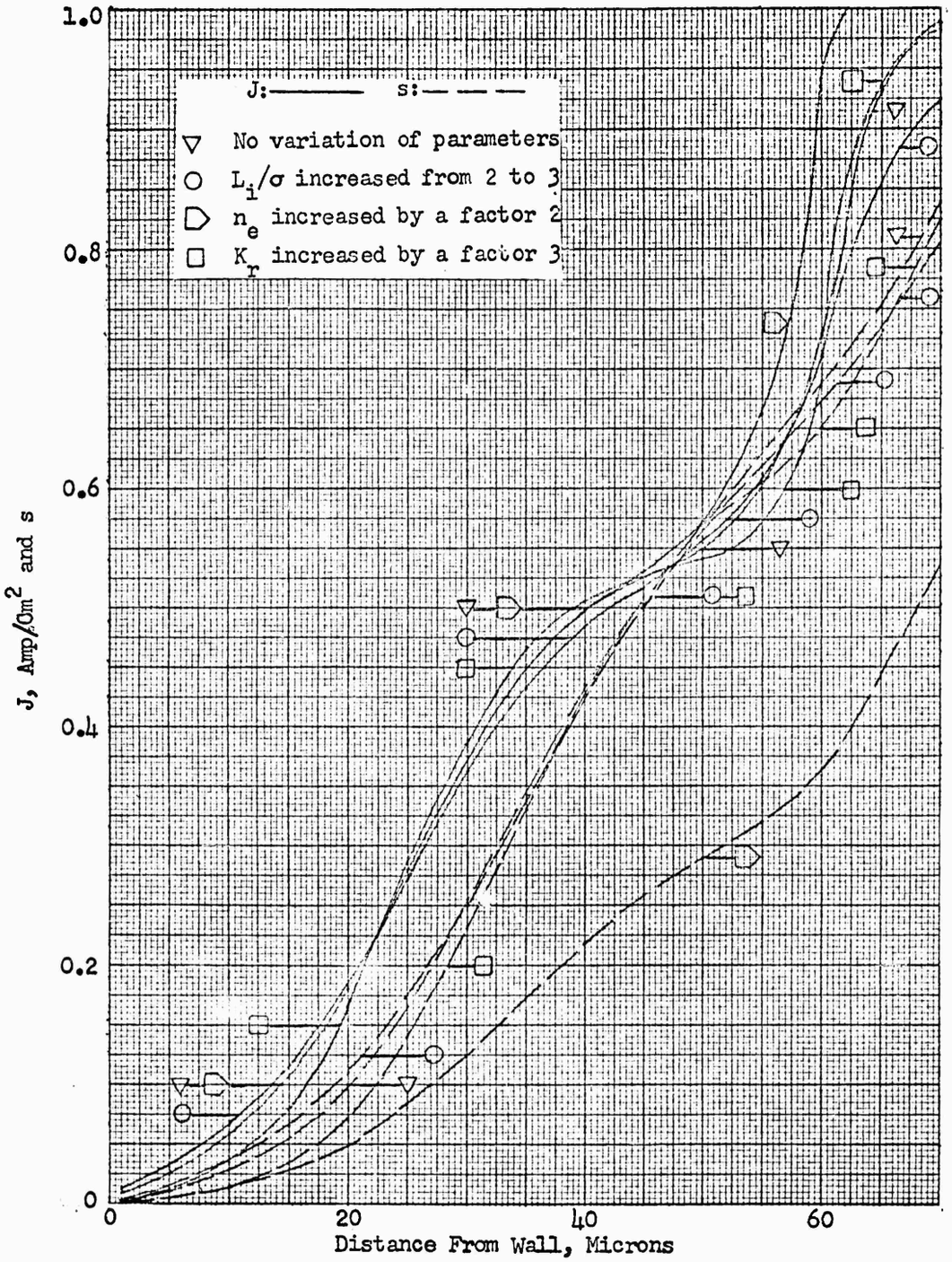

Figure 10b. Effects of L_i/σ, n_e, K_f and K_r on the variation of J and s through the boundary layer for the 0.25 inch probes at $M_s = 10.43$. Calculation is for s = 0 at y = 0.

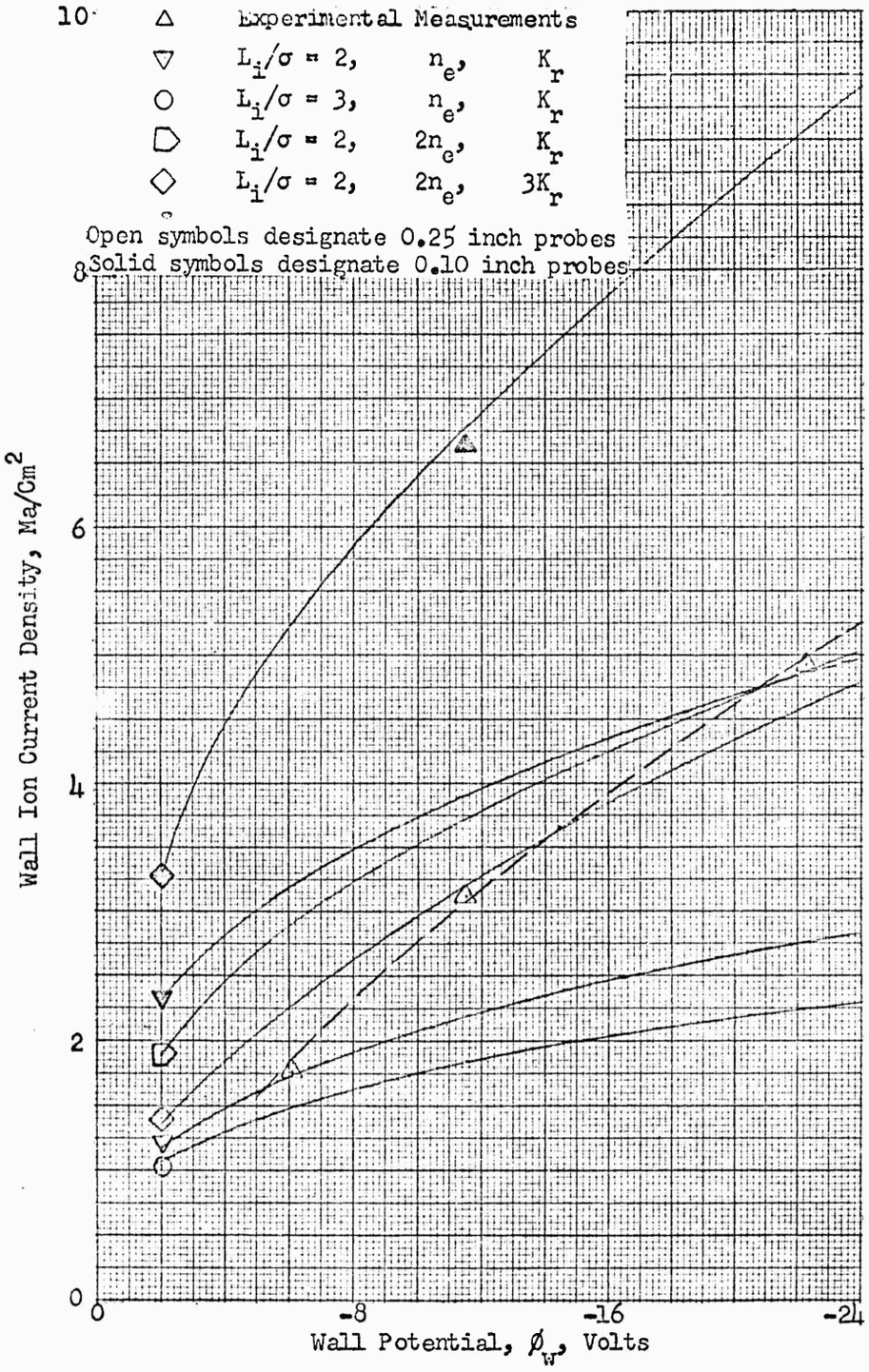

Figure 11a. Comparison of the numerical calculations with test measurements of J_w as a function of ϕ_w for the 0.25 and 0.10 inch probes at $M_s = 7.43$.

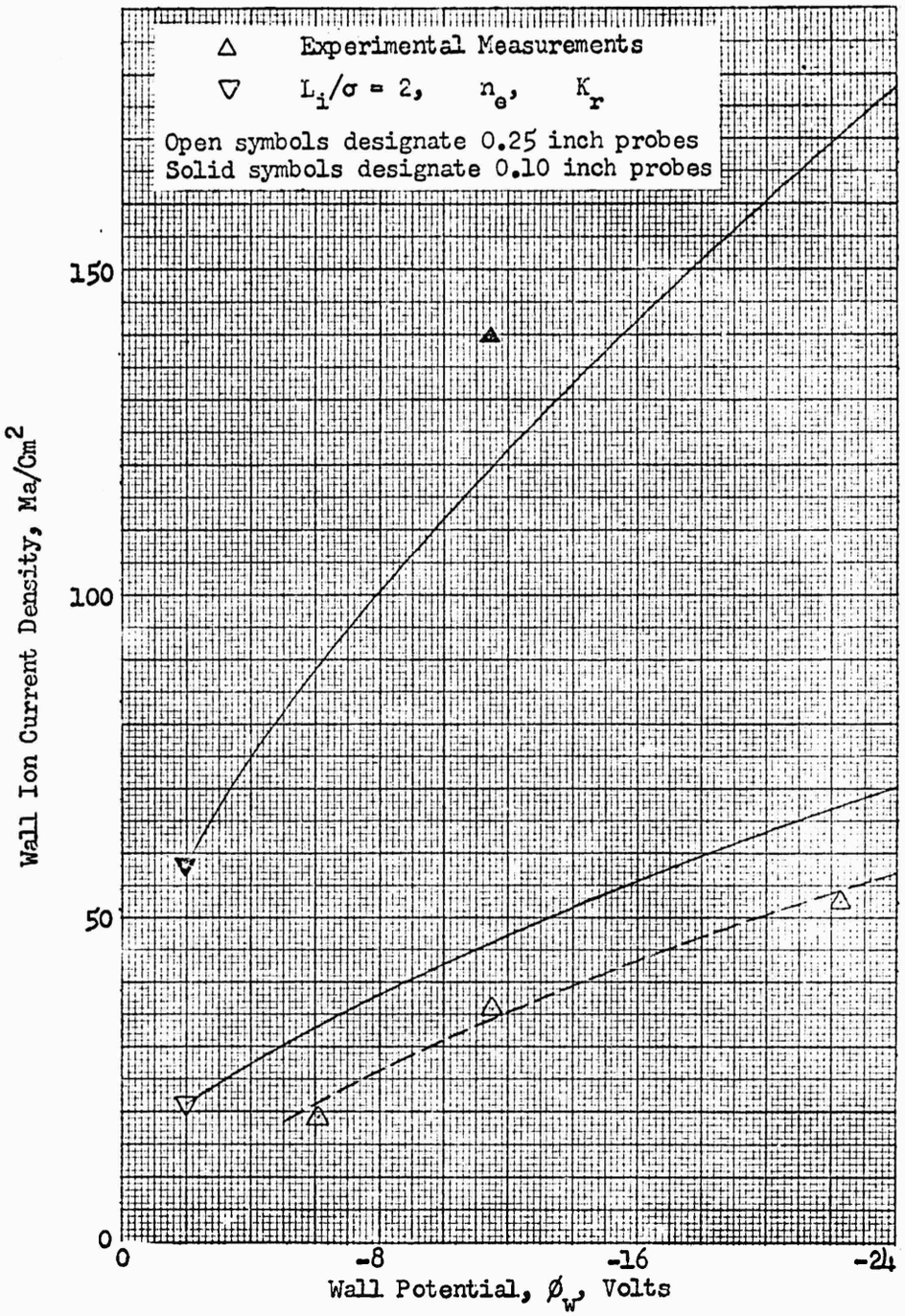

Figure 11b. Comparison of the numerical calculations with test measurements of J_w as a function of ϕ_w for the 0.25 and 0.10 inch probes at $M_s = 9.88$.

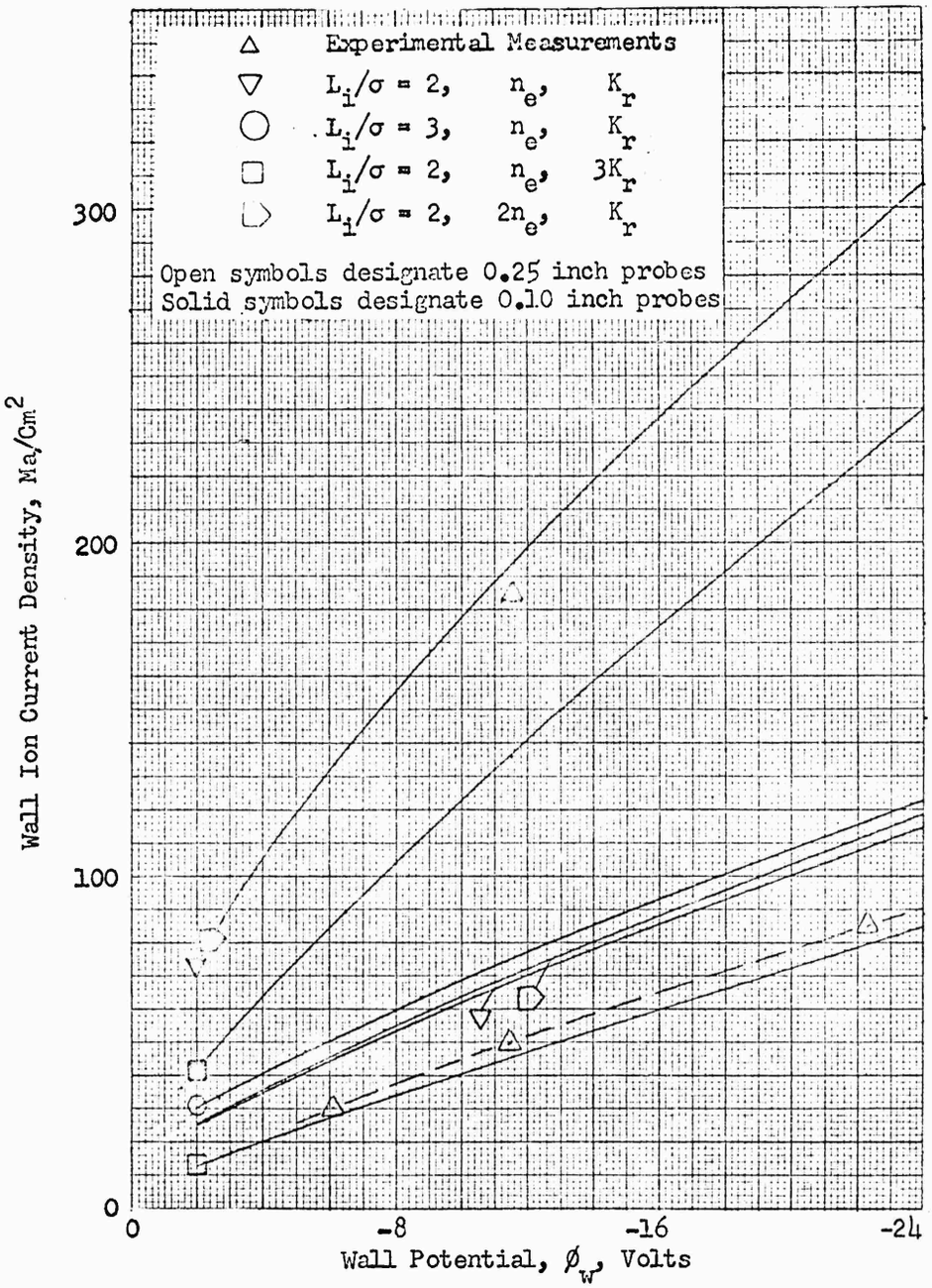

Figure 11c. Comparison of the numerical calculations with test measurements of J_w as a function of ϕ_w for the 0.25 and 0.10 inch probes at $M_s = 10.43$.

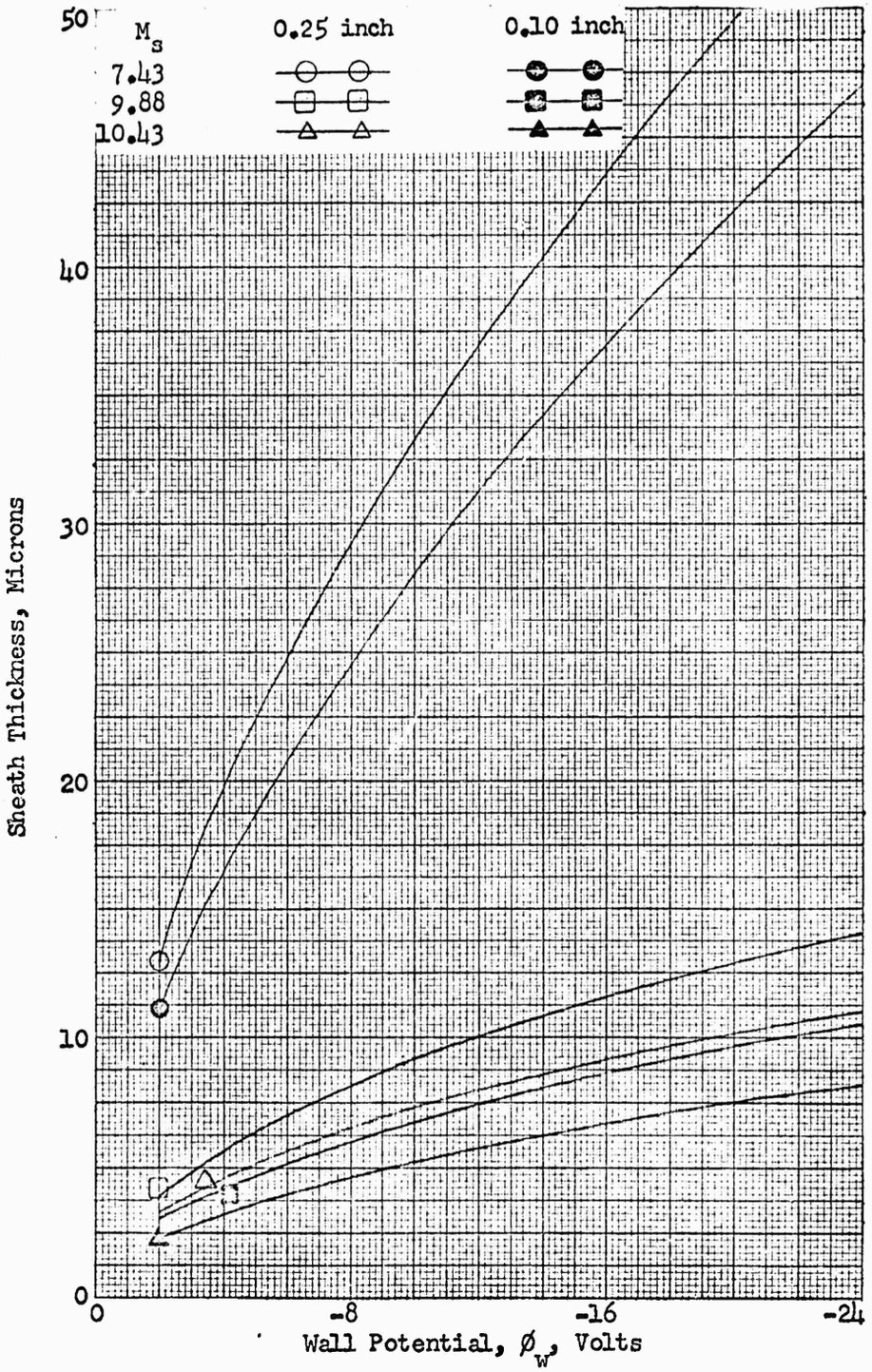

Figure 12a. Variation of δ_s with ϕ_w for the 0.25 and 0.10 inch probes at M_s = 7.43, 9.88 and 10.43.

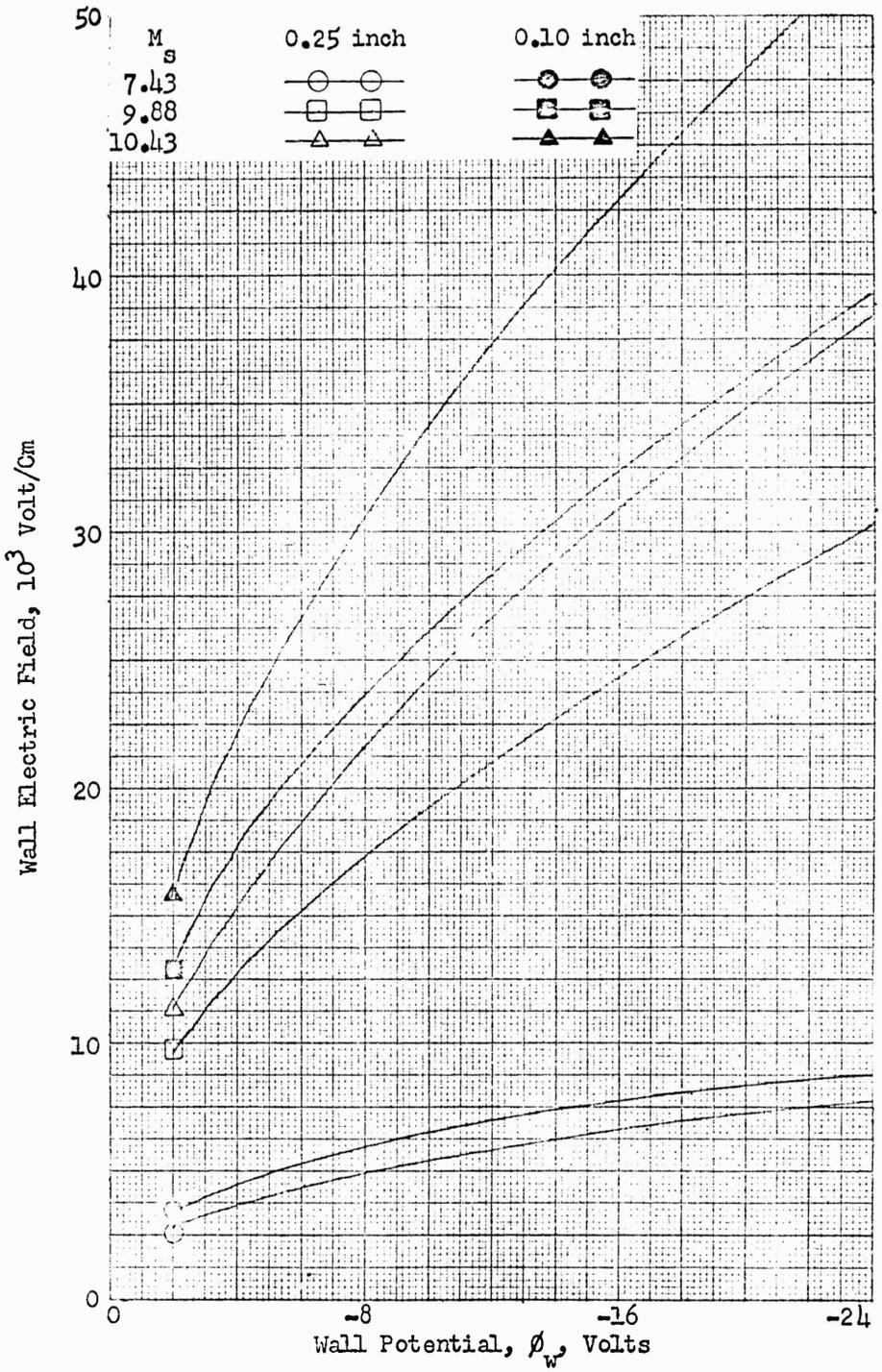

Figure 12b. Variation of ϕ_{yw} with ϕ_w for the 0.25 and 0.10 inch probes at M_s = 7.43, 9.88 and 10.43.

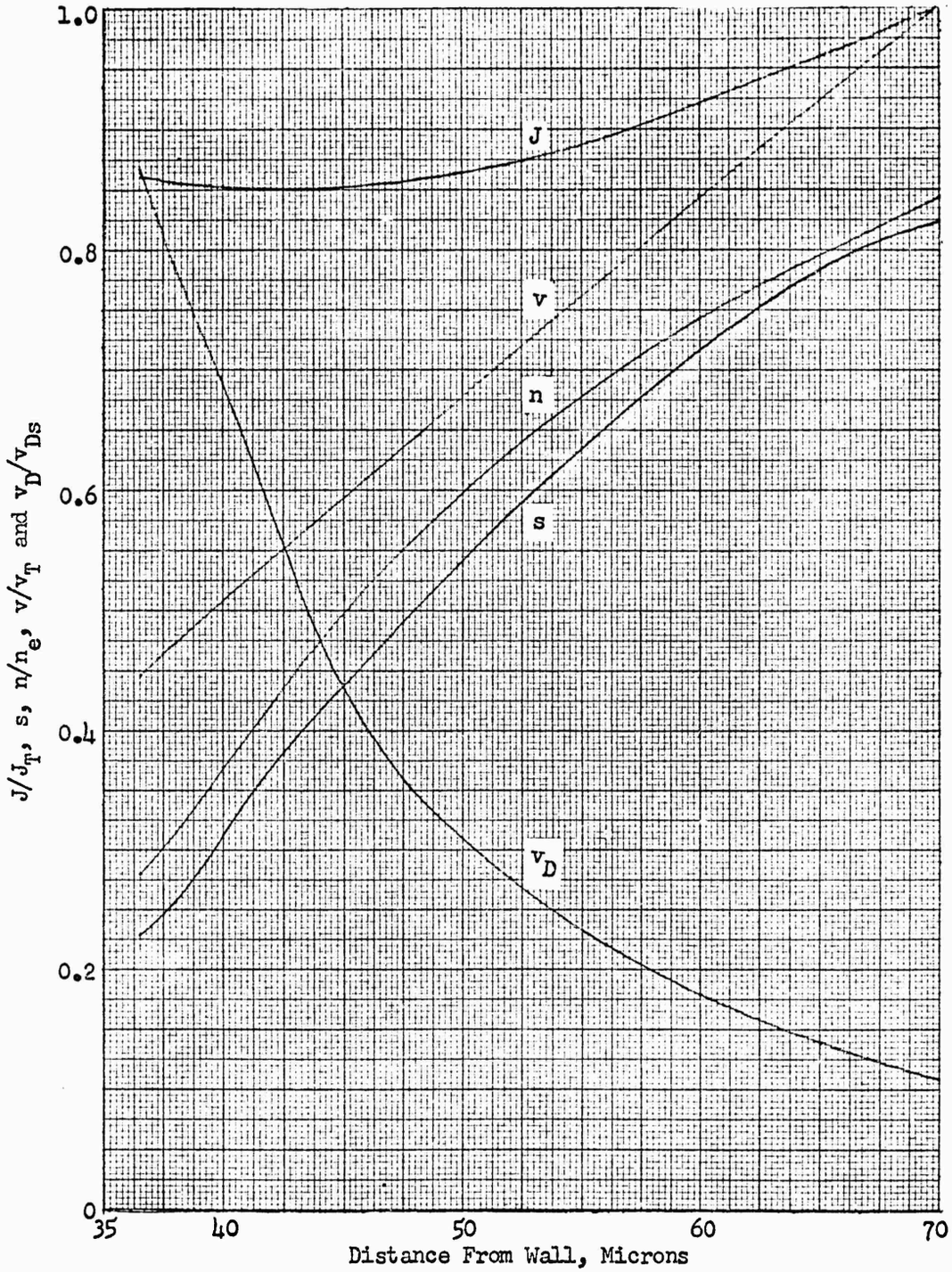

Figure 13a. Variation of J, s, n, v and v_D outside the sheath for ϕ_w = -11.5 volts on the 0.25 inch probes at M_s = 7.43. J_T = 2.65 ma/cm^2, n_e = 8.40 (10^{12})/cm^3, v_T = 1,780 cm/sec, v_{Ds} = 5,290 cm/sec. δ_s = 36.5 microns.

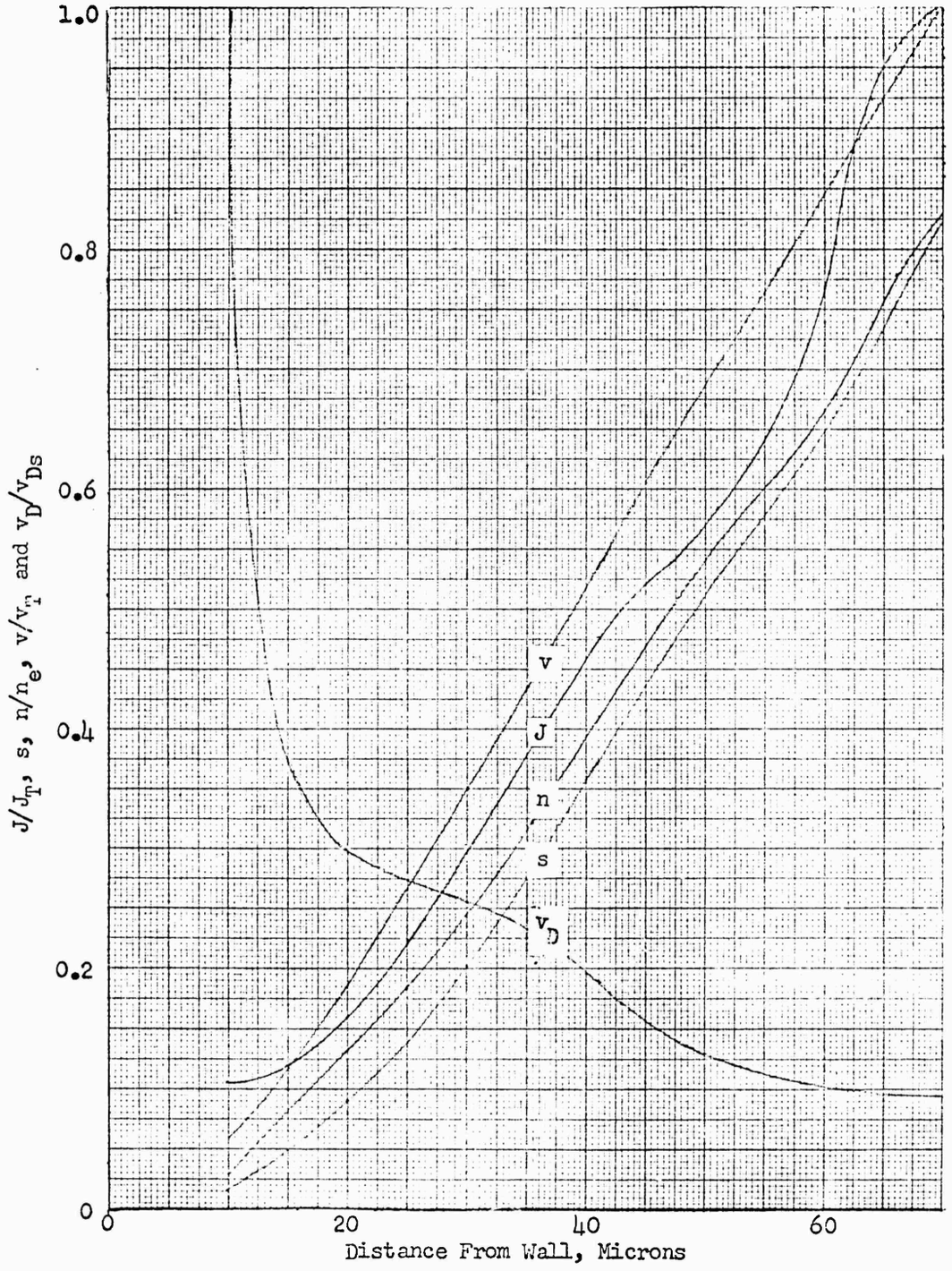

Figure 13b. Variation of J, s, n, v and v_D outside the sheath for ϕ_w = -11.5 volts on the 0.25 inch probes at M_s = 9.88. J_T = 436 ma/cm^2, n_e = 1.116 (10^{15})/cm^3, v_T=2,190 cm/sec, v_{Ds} = 8,800 cm/sec. δ_s = 9.85 microns.

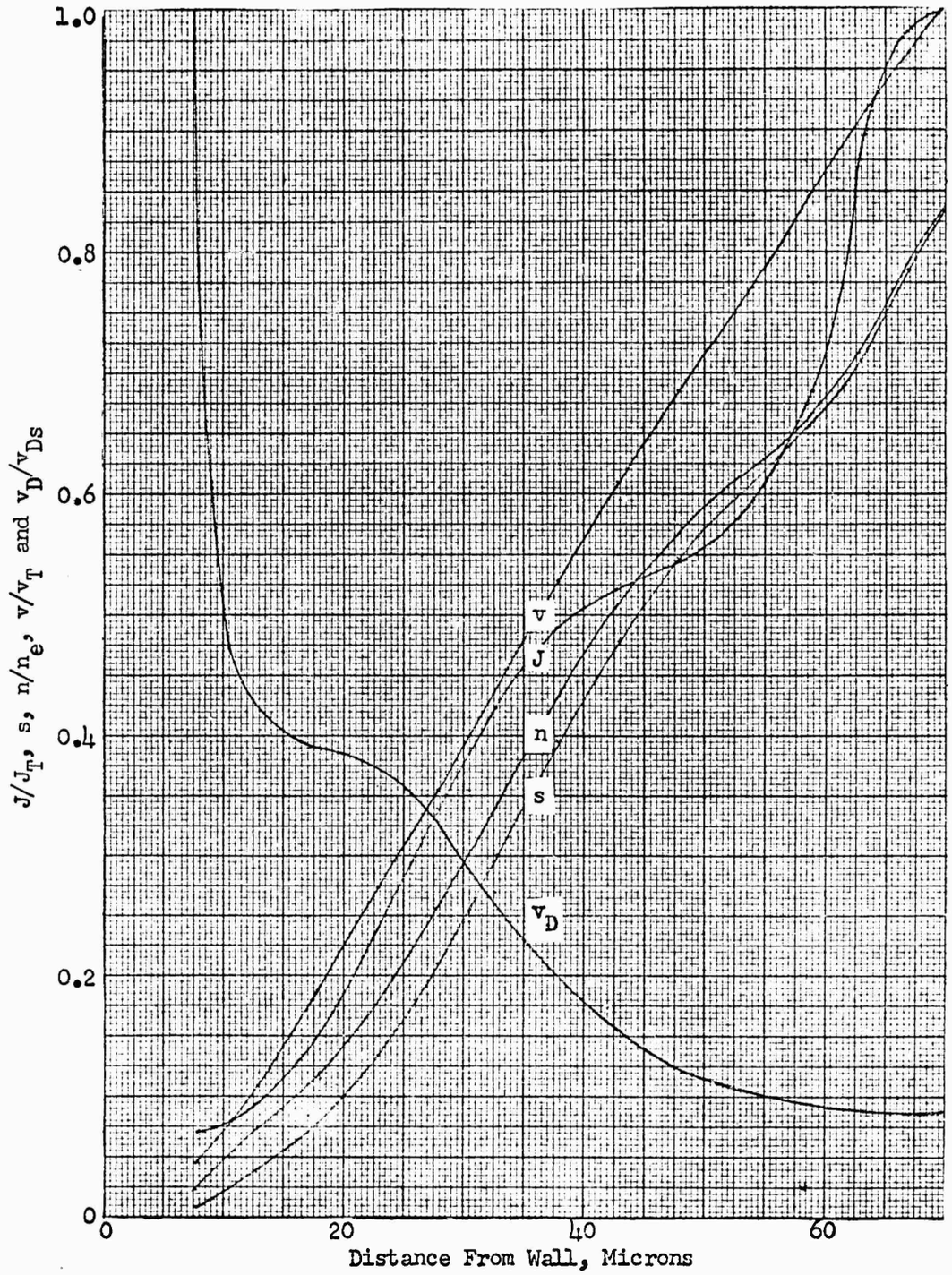

Figure 13c. Variation of J, s, n, v and v_D outside the sheath for ϕ_w = -11.5 volts on the 0.25 inch probes at M_s = 10.43. J_T = 986 ma/cm^2, n_e = 2.32 (10^{15})/cm^3, v_T = 2,460 cm/sec, v_{Ds} = 8,190 cm/sec. δ_s = 7.77 microns.

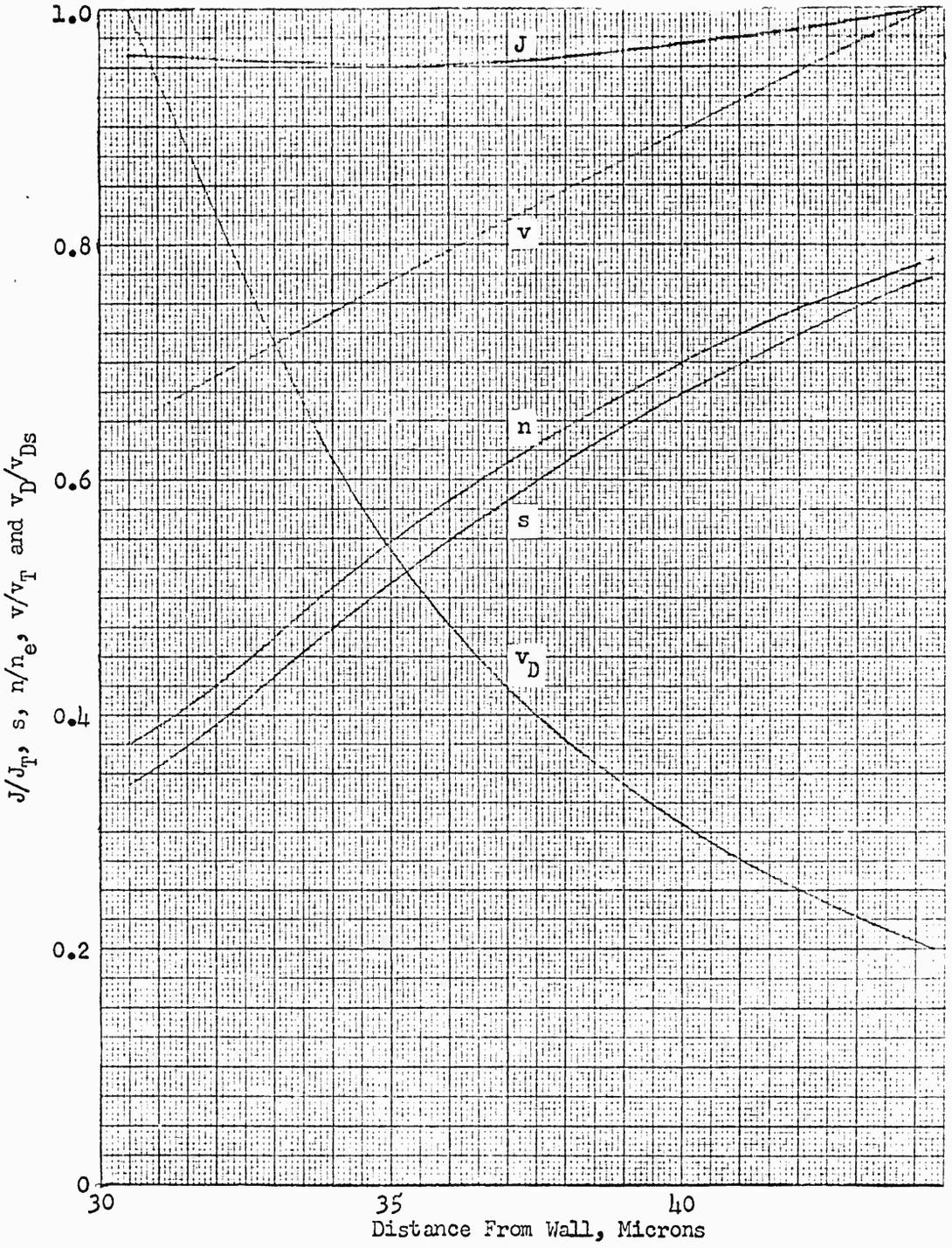

Figure 13d. Variation of J, s, n, v and v_D outside the sheath for ϕ_w = -11.5 volts on the 0.10 inch probes at M_s = 7.43. J_T = 4.38 ma/cm^2, n_e = 8.40 (10^{12})/cm^3, v_T = 2,820 cm/sec, v_{Ds} = 6,500 cm/sec. δ_s = 30.5 microns.

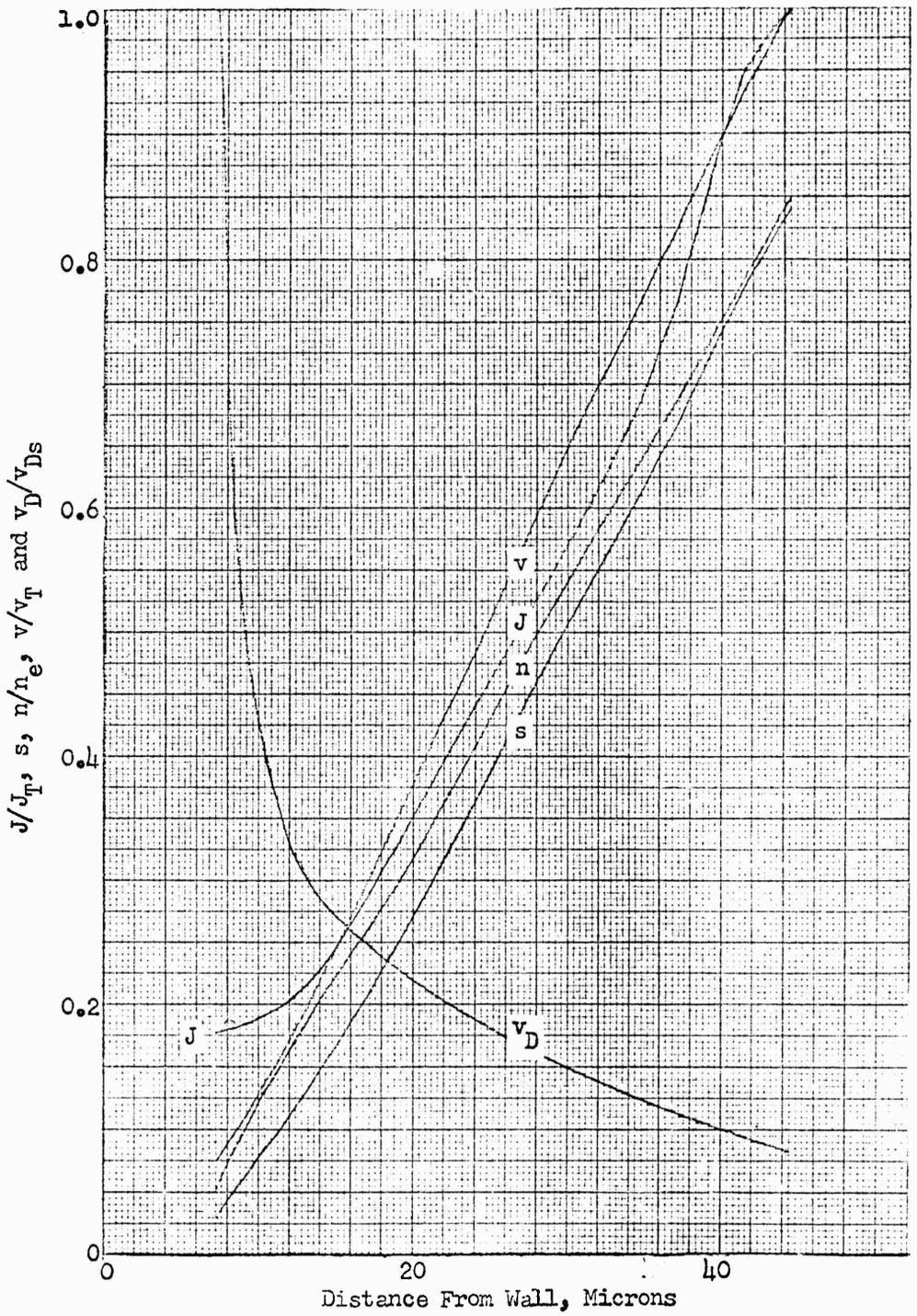

Figure 13e. Variation of J, s, n, v and v_D outside the sheath for ϕ_w = -11.5 volts on the 0.10 inch probes at M_s=9.88. J_T=684 ma/cm^2, n_e=1.116 (10^{15})/cm^3, v_T=3,480 cm/sec, v_{Ds} = 12,600 cm/sec. δ_s = 7.25 microns.

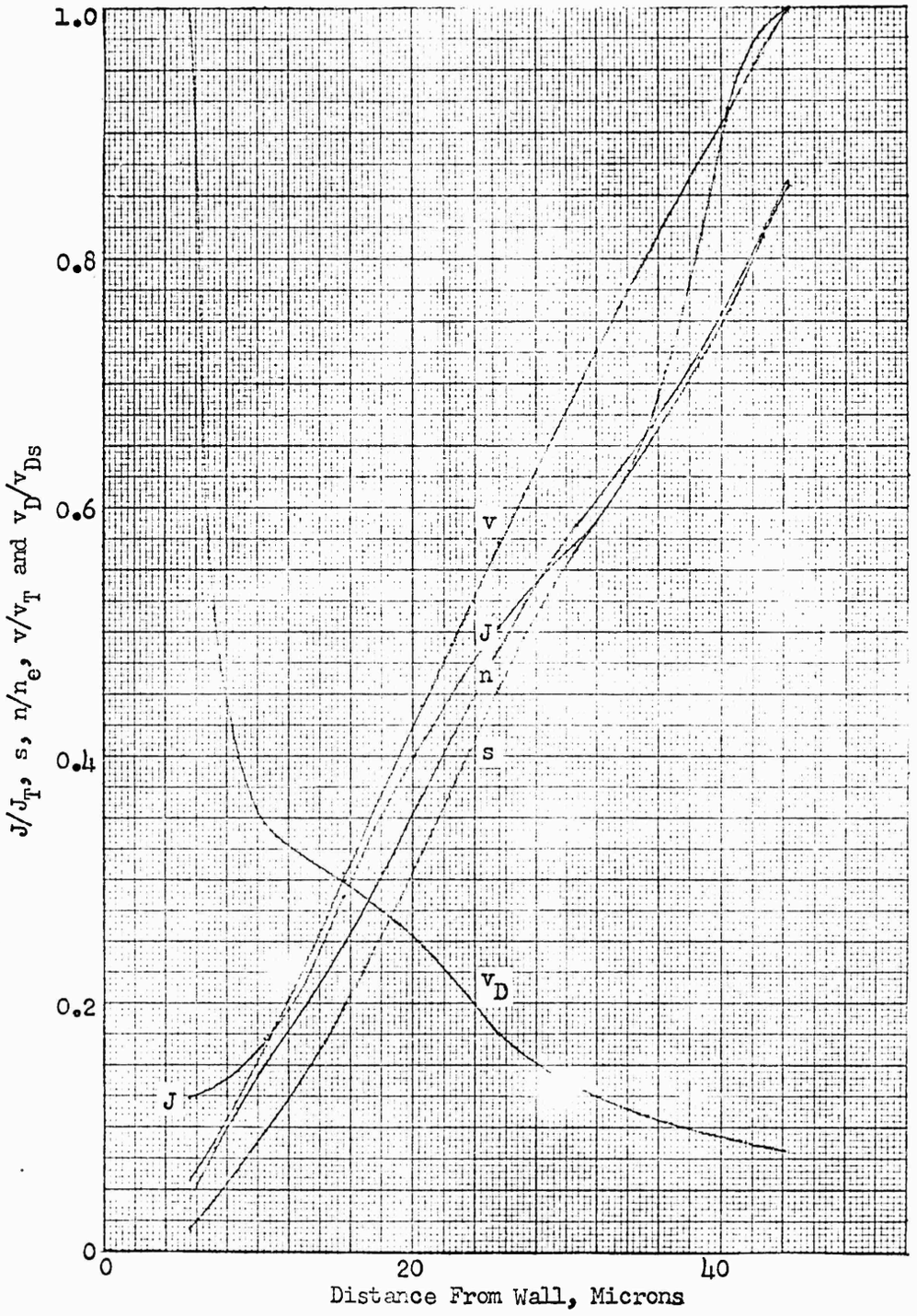

Figure 13f. Variation of J, s, n, v and v_D outside the sheath for ϕ_w = -11.5 volts on the 0.10 inch probes at M_s=10.43. J_T = 1.55 amp/cm^2, n_e= 2.32 (10^{15})/cm^3, v_T=3,880cm/sec, v_{Ds} = 11,900 cm/sec. δ_s = 5.61 microns.

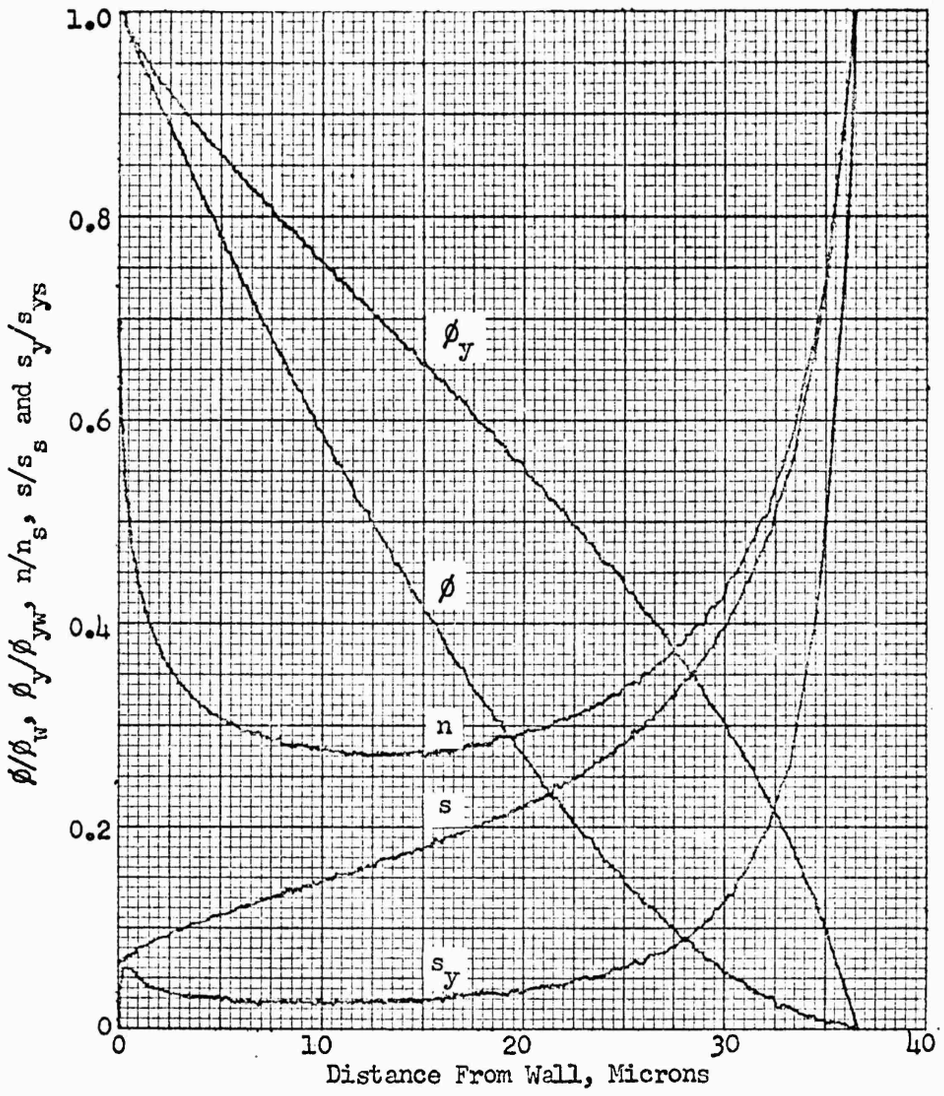

Figure 14a. Variation of ϕ, ϕ_y, n, s, s_y through the sheath for ϕ_w = -11.5 volts on the 0.25 inch probes at M_s = 7.43. ϕ_{ys} = 5,700 volt/cm, s_s = 0.229, n_s = 2.34 $(10^{12})/cm^3$, s_{ys} = 591/cm and δ_s = 36.5 microns.

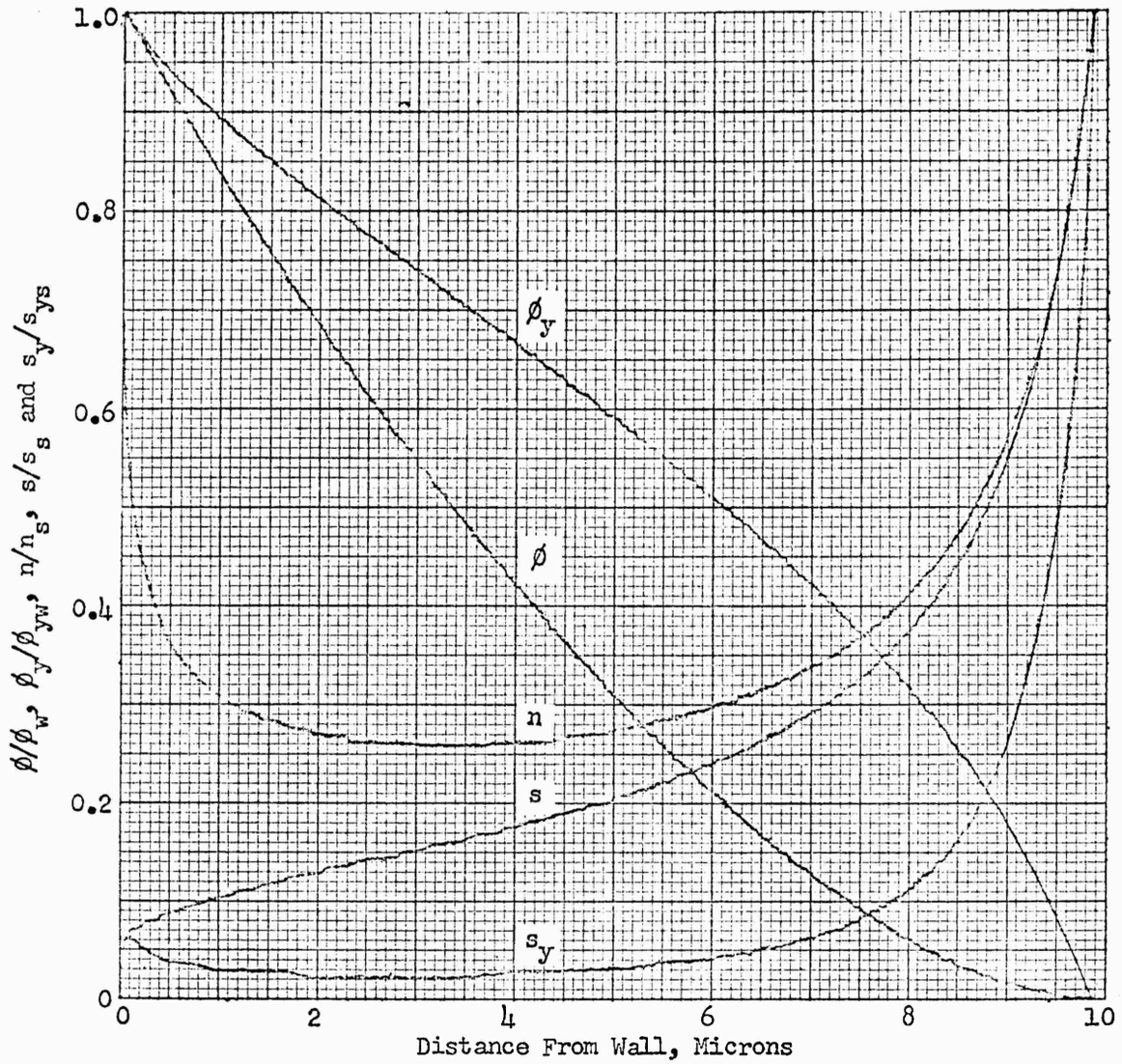

Figure 14b. Variation of ϕ, ϕ_y, n, s, s_y through the sheath for $\phi_w = -11.5$ volts on the 0.25 inch probes at $M_s = 9.88$. $\phi_{yw} = 20{,}700$ volt/cm, $n_s = 3.26\ (10^{13})/cm^3$, $s_s = 0.0144$, $s_{ys} = 145/cm$ and $\delta_s = 9.85$ microns.

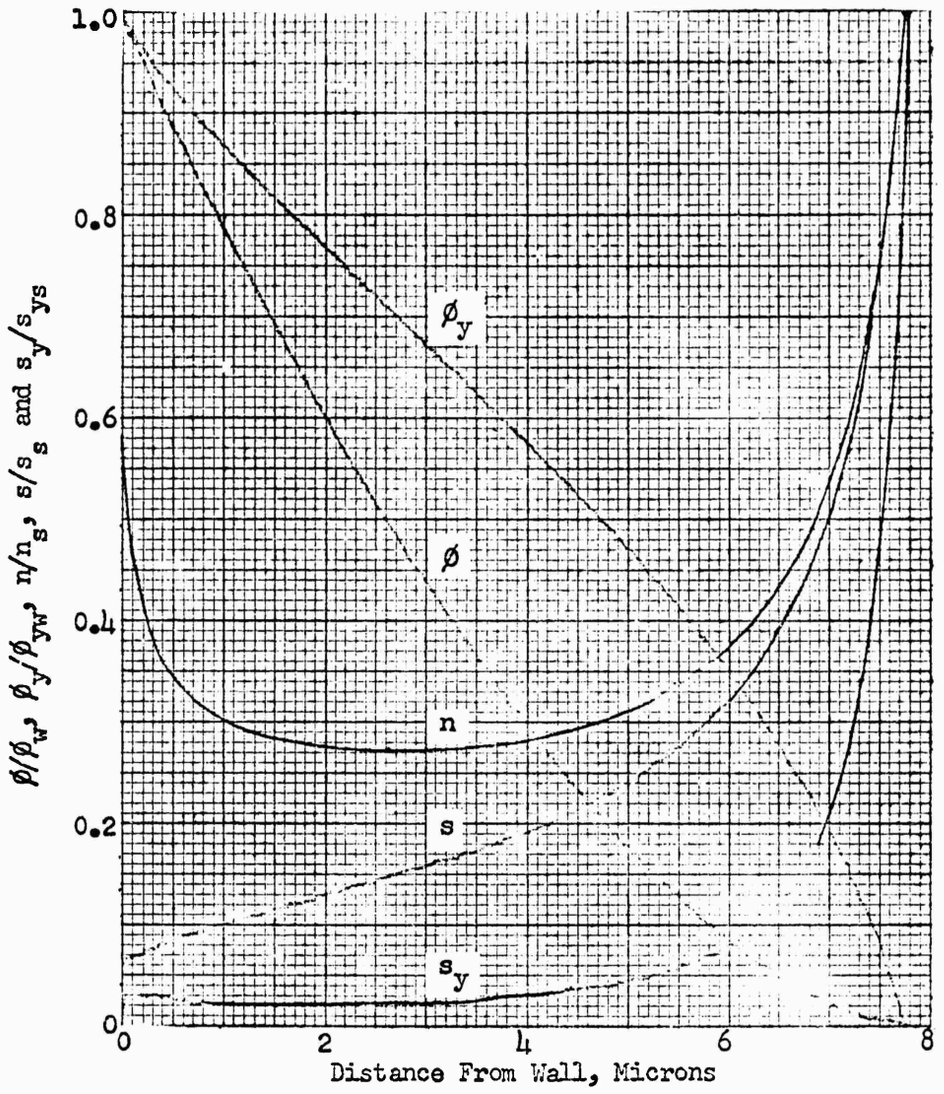

Figure 14c. Variation of ϕ, ϕ_y, n, s, s_y through the sheath for ϕ_w = -11.5 volts on the 0.25 inch probes at M_s = 10.43. ϕ_{yw} = 26,200 volt/cm, s_s = 0.00861, n_s = 5.18 $(10^{13})/cm^3$, s_{ys} = 118/cm and δ_s = 7.77 microns.

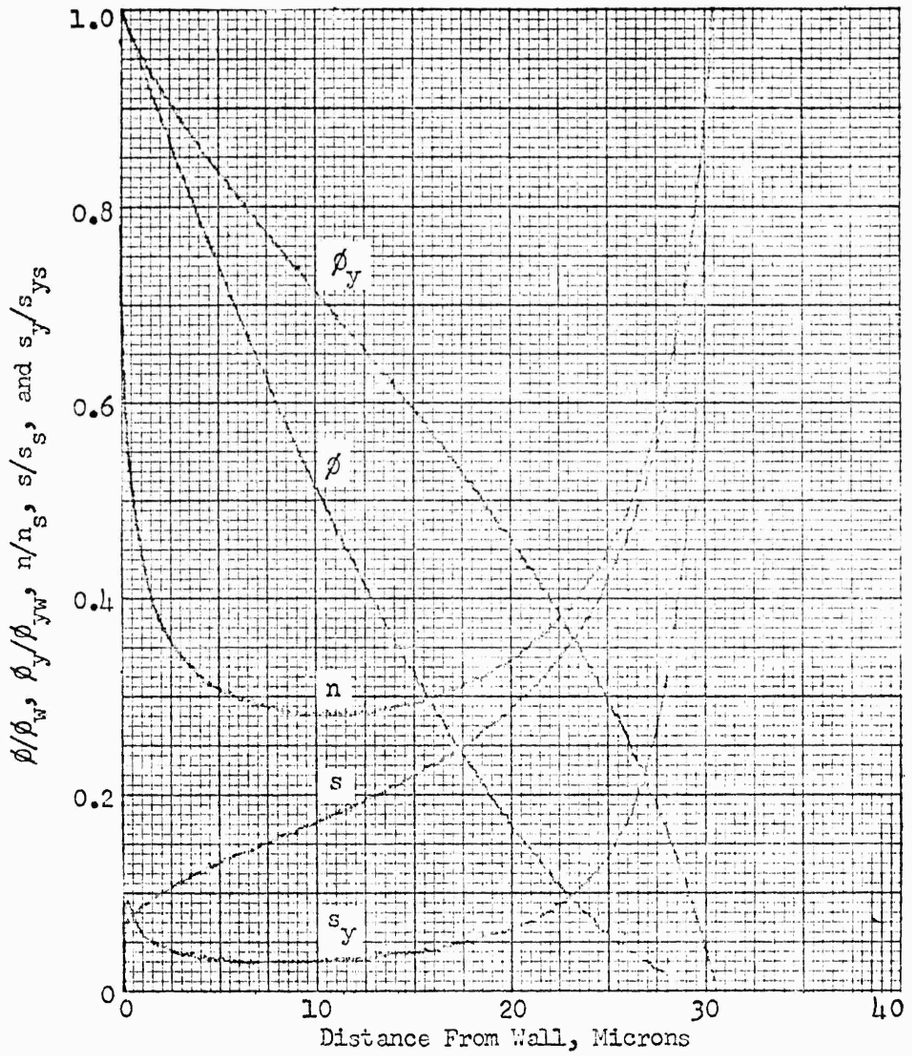

Figure 14d. Variation of ϕ, ϕ_y, n, s, s_y through the sheath for $\phi_w = -11.5$ volts on the 0.10 inch probes at $M_s = 7.43$. $\phi_{yw} = 6{,}700$ volt/cm, $n_s = 3.15\ (10^{12})/cm^3$, $s_s = 0.340$, $s_{ys} = 949/cm$ and $\delta_s = 30.5$ microns.

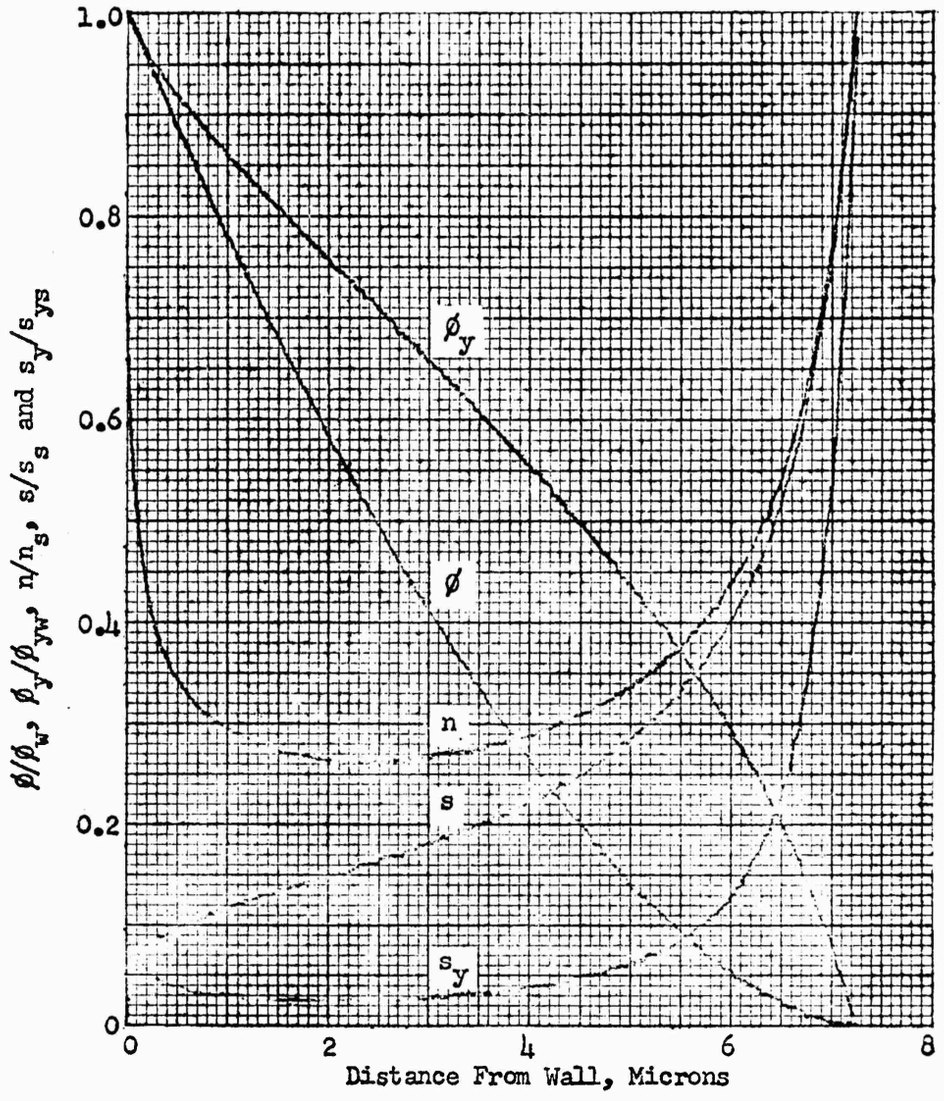

Figure 14e. Variation of ϕ, ϕ_y, n, s, s_y through the sheath for $\phi_w = -11.5$ volts on the 0.10 inch probes at $M_s = 9.88$. $\phi_{yw} = 28{,}000$ volt/cm, $s_s = 0.0279$, $n_s = 5.89\ (10^{15})/cm^3$, $s_{ys} = 367/cm$ and $\delta_s = 7.25$ microns.

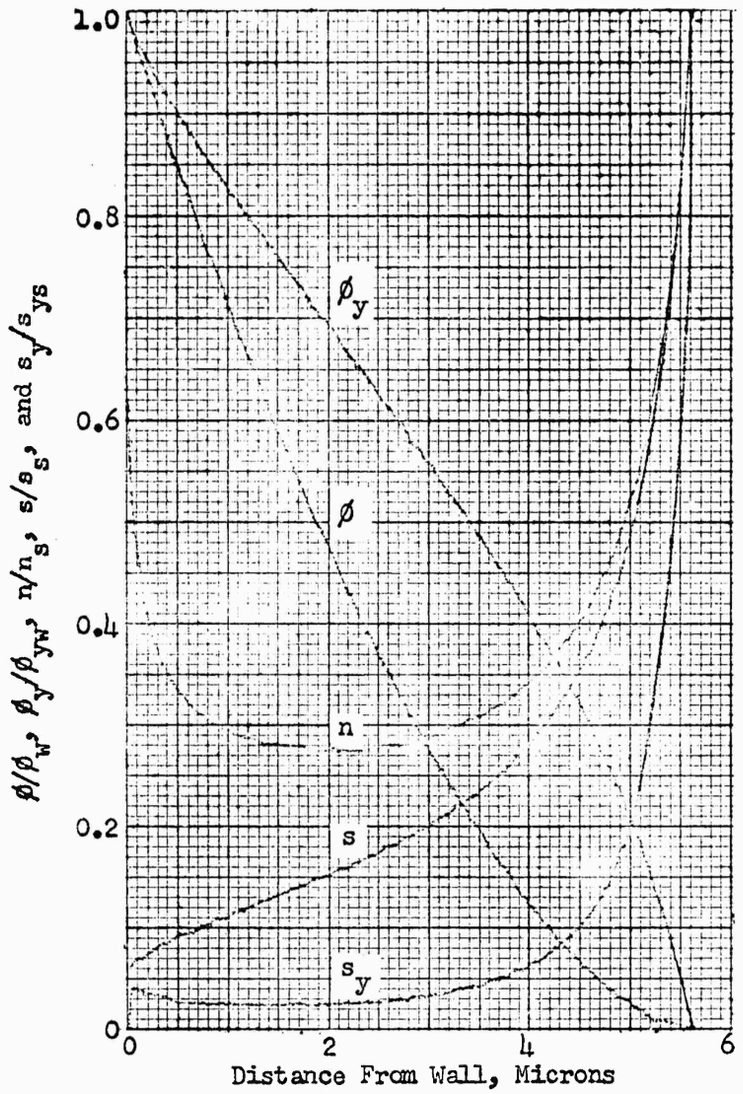

Figure 14f. Variation of ϕ, ϕ_y, n, s, s_y through sheath for $\phi_w = -11.5$ volts on the 0.10 inch probes at $M_s = 10.43$. $\phi_{yw} = 36{,}800$ volt/cm, $s_s = 0.0179$, $n_s = 9.94\ (10^{13})/cm^3$, $s_{ys} = 324/cm$ and $\delta_s = 5.61$ microns.

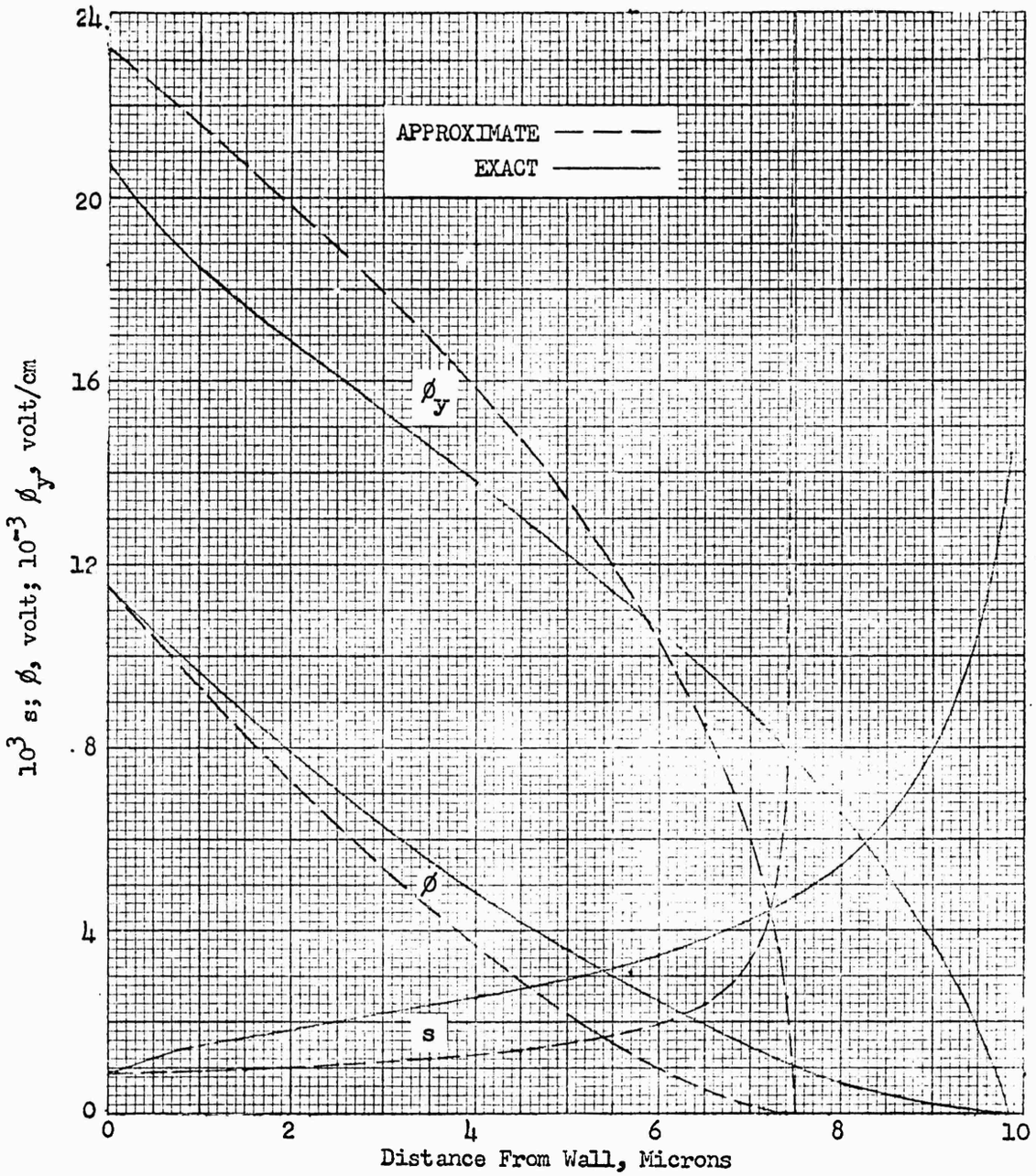

Figure 15. Comparison of the exact and approximate numerical solutions of ϕ, ϕ_y and s for ϕ_w = -11.5 volts at M_s = 9.88.

DISTRIBUTION

Commanding General
U.S. Army Materiel Command
Washington 25, D. C.
Attn: Lt. Col W. E. Mehlinger, AMCRD-DE-N

Commanding General
Defense Atomic Support Agency
Washington 25, D. C.
Attn: W. J. Otting

Office of Director
Defense Research & Engineering
Weapons Systems Evaluation Group
The Pentagon
Washington 25, D. C.

Commanding Officer
U.S. Army Munitions Command
Dover, New Jersey

Office of the Chief of Research & Development
Department of the Army
Washington 25, D. C.

DDC Headquarters (Defense Documentation Center)
Cameron Station, Bldg No. 5
5010 Duke Street
Alexandria, Virginia
Attn: TISIA (20 copies)

Ordnance Technical Intelligence Agency
Arlington Hall Station
Arlington 12, Virginia

Aerodynamics Laboratory
David Taylor Model Basin
Carderock, Md.
Attn: R. Craven

U.S. Naval Research Laboratory
Washington 25, D. C.

U.S. Air Force
Aeronautical Systems Division
Wright-Patterson Air Force Base, Ohio

U.S. Air Force
Air Force Cambridge Research Laboratories
Laurence G. Hanscom Field
Bedford, Massachusetts

National Aeronautics & Space
Administration
Ames Research Center
Moffett Field, Calif.

Armour Research Foundation
10 W. 35th Street
Chicago 16, Illinois

University of Chicago
Laboratories for Applied Sciences
Chicago 37, Illinois

Electronics Research Laboratories
Columbia University
New York 27, New York
Attn: Tech Library

Cornell Aeronautical Laboratory, Inc.
4455 Genesee Street
Buffalo 21, New York

Denver Research Institute
University of Denver
University Park
Denver 10, Colorado

Research Laboratory of Electronics
Massachusetts Institute of Technology
Cambridge 39, Mass.

Massachusetts Institute of Technology
Aerophysics Laboratory
Cambridge 39, Mass.

Massachusetts Institute of Technology
Lincoln Laboratory
P.O. Box 73
Lexington 73, Mass.

Purdue University
Lafayette, Indiana
Attn: Dr. Robert Goulard

Prof. J. H. deLeeuw
Institute of Aerophysics
University of Toronto,
Toronto 5, Canada

Syracuse University Research Corporation
University Station
Syracuse 10, New York

Aerojet-General Corporation
Azusa, Calif.

Aerospace Corporation
P.O. Box 95085
Los Angeles 45, Calif.
Attn: Library Technical Documents Group

Avco-Everett Research Laboratory
2385 Revere Beach Parkway
Everett, Mass.
Attn: N. H. Kemp
Attn: F. R. Riddell
Attn: J. D. Teare
Attn: E. L. Resler

Barnes Engineering Company
30 Commerce Road
Stamford, Connecticut

Battelle Defender
Battelle Memorial Institute
505 King Street
Columbus 1, Ohio

Bell Telephone Laboratories
Whippany Road
Whippany, New Jersey

Bendix Corporation
Bendix Systems Division
3300 Plymouth Road
Ann Arbor, Michigan

The Boeing Company
Aerospace Division
Seattle 24, Washington

Chance Vought Corporation
Dallas 22, Texas

Defense Research Corporation
4050 State Street
Santa Barbara, Calif.

Douglas Aircraft Company
3000 Ocean Park Boulevard
Santa Monica, Calif.

Electro-Optical Systems, Inc.
125 North Vinedo Avenue
Pasadena, Calif.

Prof. L. Talbot
Aerospace & Aeronautics Dept
University of California
Berkeley, Calif.

Ford Motor Company
Aeronutronic Division
Ford Road
Newport Beach, Calif.
Attn: Acquisitions Library

General Dynamics
Astronautics Division
San Diego 12, Calif.

General Dynamics
Convair Division
San Diego 12, Calif.

General Electric Company
Space Sciences Laboratory
Space Technology Center
King of Prussia, Penn.
Attn: Tech Library

General Electric Company, TEMPO
735 State Street
Santa Barbara, Calif.
Attn: Tech Library

General Motors Corporation
Defense Systems Division
Box T
Santa Barbara, Calif.
Attn: Tech Library

Geophysics Corporation of America
Burlington Road
Bedford, Mass.
Attn: Tech Library

Hughes Aircraft Company
Fullerton, Calif.

ITT Federal Laboratories
225 Santa Monica Blvd.
Santa Monica, Calif.

Dr. W. J. Pearce
Dept. of Electrical Engineering
Lehigh University
Bethlehem, Penn.

Lockheed Corporation
Missile and Space Divisions
Palo Alto, Calif.

Lockheed Corporation
Missiles and Space Divisions
Sunnyvale, Calif.

Martin Company
Denver Division
Mail #A-314
Denver 1, Colorado

North American Aviation, Inc.
International Airport
Los Angeles 45, Calif.
Attn: Technical Library

Radio Corporation of America
Moorestown, New Jersey
Attn: Tech Library

The RAND Corporation
1700 Main Street
Santa Monica, Calif.

Raytheon Company
Missile and Space Division
Santa Barbara, Calif.

Space Technology Laboratories, Inc.
P.O. Box 95001
Los Angeles 45, Calif.

Prof. D. L. Turcotte
Aeronautical Engineering Dept.
Cornell University
Ithaca, New York

Defense Atomic Support Agency
Electromagnetic Branch
Washington, D. C.
Attn: Major J D. Brown/C. Blank

Sylvania Electronics Products, Inc.
Electronic Defense Laboratories
Mountain View, Calif.

Documentation, Inc.
4827 Rugby Avenue
Bethesda, Md.
Attn: W. Kuebler

Prof. J. M. Burgers
Institute for Fluid Dynamics and Applied Mathematics
University of Maryland
College Park, Md. (6 copies)

Prof. A. W. Sherwood
Aeronautical Engineering Dept
University of Maryland
College Park, Maryland

Prof. John Weske
Aeronautical Engineering Dept
University of Maryland
College Park, Maryland

Prof. F. Biberstein, Head
Civil Engineering Dept.
Catholic University of America
Washington, D. C.

Office of the Chief of Research & Development
Department of the Army
Washington 25, D. C.
Attn: Director, Army Research
Attn: Atomic Office

Prof. S-I Pai
Institute for Fluid Dynamics and Applied Mathematics
University of Maryland
College Park, Maryland

DISTRIBUTION (Continued)

Aeronautical Engineering Dept
University of Minnesota
Minneapolis, Minn.

Aeronautical Engineering Dept
Calif. Institute of Technology
Pasadena, Calif.

Aeronautical Engineering Dept
Ohio State University
Columbus, Ohio

Aeronautical Engineering Dept
University of Michigan
Ann Arbor, Mich.
Attn: A. M. Kuethe

Massachusetts Institute of Technology
Cambridge 39, Mass.
Attn: J. A. Fay

Stanford Research Institute
Menlo Park, Calif.
Attn: Tech Library

INTERNAL

Horton, B. M./McEvoy, R. W., Lt. Col.
Apstein, M./Gerwin, H. L./Guarino, P. A./Kalmus, H. P.
Spates, J. E./Schwenk, C. C.
Hardin, C. D., Lab 100
Sommer, H., Lab 200
Hatcher, R. D., Lab 300
Hoff, R. S., Lab 400
Nilson, H. M., Lab 500
Flyer, I. N., Lab 600
Campagna, J. H./Apolenis, C. J., Div 700
DeMasi, R., Div 800
Landis, P. E., Lab 900
Seaton, J. W., 260
Curchack, H. D., 320
Gieske, H., 320
Haas, P., 230
Harris, F. T , 320
Morrison, C. A , 320
Reddan, M., 930
Pollin, I., 260 (20 copies)
Rosado, J., 260
Rotkin, I./Godfrey, T. B./Bryant, W. T.
Distad, M. F./McCoskey, R. E./Moorhead, J. G.
Tevelow, F. L., 320
Tompkins, J., 260
Ward, A. L., 930
HDL Library (5 copies)
Technical Reports Unit,800
Tech Info Off 010 (10 cps)

(Two pages of abstract cards follow.)

AD________ Accession No.________

Harry Diamond Laboratories, Washington 25, D. C.

THE STAGNATION-POINT LANGMUIR PROBE IN A SHOCK TUBE---THEORY AND MEASUREMENTS - Irvin Pollin

TR-1103, 28 June 1963, 58 pp text, 30 pp illus., AMCMS Code 5900.21.83021, HDL Proj 23800, UNCLASSIFIED Report

A model of the ion-electron flow in the stagnation region between the detached shock and the wall of a Langmuir-type probe is proposed for ionized air in a shock tube at ion mass fractions less than 10^{-4}. The probe consists of a collecting electrode located at the stagnation point of an axially symmetric blunt body. Based on the close agreement between numerical calculations and measurements of the probe wall ion current density, the proposed model gives an accurate description of the ion-electron flow in the stagnation point boundary layer for negative electrode potentials. The procedure is also indicated to be applicable in the stagnation region between the detached probe shock and the edge of the boundary layer. However, the ion and the electron number densities in the undisturbed incident flow ahead of the detached shock cannot be obtained unless it is possible to calculate the changes in the number densities across the shock.

Theory of Langmuir probes in shock tubes

Ion-electron measurements in shock tubes

Blunt body ion-electron distribution

AD________ Accession No.________

Harry Diamond Laboratories, Washington 25, D. C.

THE STAGNATION-POINT LANGMUIR PROBE IN A SHOCK TUBE---THEORY AND MEASUREMENTS - Irvin Pollin

TR-1103, 28 June 1963, 58 pp text, 30 pp illus., AMCMS Code 5900.21.83021, HDL Proj 23800, UNCLASSIFIED Report

A model of the ion-electron flow in the stagnation region between the detached shock and the wall of a Langmuir-type probe is proposed for ionized air in a shock tube at ion mass fractions less than 10^{-4}. The probe consists of a collecting electrode located at the stagnation point of an axially symmetric blunt body. Based on the close agreement between numerical calculations and measurements of the probe wall ion current density, the proposed model gives an accurate description of the ion-electron flow in the stagnation point boundary layer for negative electrode potentials. The procedure is also indicated to be applicable in the stagnation region between the detached probe shock and the edge of the boundary layer. However, the ion and the electron number densities in the undisturbed incident flow ahead of the detached shock cannot be obtained unless it is possible to calculate the changes in the number densities across the shock.

Theory of Langmuir probes in shock tubes

Ion-electron measurements in shock tubes

Blunt body ion-electron distribution

AD________ Accession No.________

Harry Diamond Laboratories, Washington 25, D. C.

THE STAGNATION-POINT LANGMUIR PROBE IN A SHOCK TUBE---THEORY AND MEASUREMENTS - Irvin Pollin

TR-1103, 28 June 1963, 58 pp text, 30 pp illus., AMCMS Code 5900.21.83021, HDL Proj 23800, UNCLASSIFIED Report

A model of the ion-electron flow in the stagnation region between the detached shock and the wall of a Langmuir-type probe is proposed for ionized air in a shock tube at ion mass fractions less than 10^{-4}. The probe consists of a collecting electrode located at the stagnation point of an axially symmetric blunt body. Based on the close agreement between numerical calculations and measurements of the probe wall ion current density, the proposed model gives an accurate description of the ion-electron flow in the stagnation point boundary layer for negative electrode potentials. The procedure is also indicated to be applicable in the stagnation region between the detached probe shock and the edge of the boundary layer. However, the ion and the electron number densities in the undisturbed incident flow ahead of the detached shock cannot be obtained unless it is possible to calculate the changes in the number densities across the shock.

Theory of Langmuir probes in shock tubes

Ion-electron measurements in shock tubes

Blunt body ion-electron distribution

AD________ Accession No.________

Harry Diamond Laboratories, Washington 25, D. C.

THE STAGNATION-POINT LANGMUIR PROBE IN A SHOCK TUBE---THEORY AND MEASUREMENTS - Irvin Pollin

TR-1103, 28 June 1963, 58 pp text, 30 pp illus., AMCMS Code 5900.21.83021, HDL Proj 23800, UNCLASSIFIED Report

A model of the ion-electron flow in the stagnation region between the detached shock and the wall of a Langmuir-type probe is proposed for ionized air in a shock tube at ion mass fractions less than 10^{-4}. The probe consists of a collecting electrode located at the stagnation point of an axially symmetric blunt body. Based on the close agreement between numerical calculations and measurements of the probe wall ion current density, the proposed model gives an accurate description of the ion-electron flow in the stagnation point boundary layer for negative electrode potentials. The procedure is also indicated to be applicable in the stagnation region between the detached probe shock and the edge of the boundary layer. However, the ion and the electron number densities in the undisturbed incident flow ahead of the detached shock cannot be obtained unless it is possible to calculate the changes in the number densities across the shock.

Theory of Langmuir probes in shock tubes

Ion-electron measurements in shock tubes

Blunt body ion-electron distribution

REMOVAL OF EACH CARD WILL BE NOTED ON INSIDE BACK COVER, AND REMOVED CARDS WILL BE TREATED AS REQUIRED BY THEIR SECURITY CLASSIFICATION.

AD__________ Accession No.__________

Harry Diamond Laboratories, Washington 25, D. C.

THE STAGNATION-POINT LANGMUIR PROBE IN A SHOCK TUBE---THEORY AND MEASUREMENTS - Irvin Pollin

TR-1103, 28 June 1963, 58 pp text, 30 pp illus., AMCMS Code 5900.21.83021, HDL Proj 23800, UNCLASSIFIED Report

A model of the ion-electron flow in the stagnation region between the detached shock and the wall of a Langmuir-type probe is proposed for ionized air in a shock tube at ion mass fractions less than 10^{-4}. The probe consists of a collecting electrode located at the stagnation point of an axially symmetric blunt body. Based on the close agreement between numerical calculations and measurements of the probe wall ion current density, the proposed model gives an accurate description of the ion-electron flow in the stagnation point boundary layer for negative electrode potentials. The procedure is also indicated to be applicable in the stagnation region between the detached probe shock and the edge of the boundary layer. However, the ion and the electron number densities in the undisturbed incident flow ahead of the detached shock cannot be obtained unless it is possible to calculate the changes in the number densities across the shock.

Theory of Langmuir probes in shock tubes

Ion-electron measurements in shock tubes

Blunt body ion-electron distribution

AD__________ Accession No.__________

Harry Diamond Laboratories, Washington 25, D. C.

THE STAGNATION-POINT LANGMUIR PROBE IN A SHOCK TUBE---THEORY AND MEASUREMENTS - Irvin Pollin

TR-1103, 28 June 1963, 58 pp text, 30 pp illus., AMCMS Code 5900.21.83021, HDL Proj 23800, UNCLASSIFIED Report

A model of the ion-electron flow in the stagnation region between the detached shock and the wall of a Langmuir-type probe is proposed for ionized air in a shock tube at ion mass fractions less than 10^{-4}. The probe consists of a collecting electrode located at the stagnation point of an axially symmetric blunt body. Based on the close agreement between numerical calculations and measurements of the probe wall ion current density, the proposed model gives an accurate description of the ion-electron flow in the stagnation point boundary layer for negative electrode potentials. The procedure is also indicated to be applicable in the stagnation region between the detached probe shock and the edge of the boundary layer. However, the ion and the electron number densities in the undisturbed incident flow ahead of the detached shock cannot be obtained unless it is possible to calculate the changes in the number densities across the shock.

Theory of Langmuir probes in shock tubes

Ion-electron measurements in shock tubes

Blunt body ion-electron distribution

AD__________ Accession No.__________

Harry Diamond Laboratories, Washington 25, D. C.

THE STAGNATION-POINT LANGMUIR PROBE IN A SHOCK TUBE---THEORY AND MEASUREMENTS - Irvin Pollin

TR-1103, 28 June 1963, 58 pp text, 30 pp illus., AMCMS Code 5900.21.83021, HDL Proj 23800, UNCLASSIFIED Report

A model of the ion-electron flow in the stagnation region between the detached shock and the wall of a Langmuir-type probe is proposed for ionized air in a shock tube at ion mass fractions less than 10^{-4}. The probe consists of a collecting electrode located at the stagnation point of an axially symmetric blunt body. Based on the close agreement between numerical calculations and measurements of the probe wall ion current density, the proposed model gives an accurate description of the ion-electron flow in the stagnation point boundary layer for negative electrode potentials. The procedure is also indicated to be applicable in the stagnation region between the detached probe shock and the edge of the boundary layer. However, the ion and the electron number densities in the undisturbed incident flow ahead of the detached shock cannot be obtained unless it is possible to calculate the changes in the number densities across the shock.

Theory of Langmuir probes in shock tubes

Ion-electron measurements in shock tubes

Blunt body ion-electron distribution

AD__________ Accession No.__________

Harry Diamond Laboratories, Washington 25, D. C.

THE STAGNATION-POINT LANGMUIR PROBE IN A SHOCK TUBE---THEORY AND MEASUREMENTS - Irvin Pollin

TR-1103, 28 June 1963, 58 pp text, 30 pp illus., AMCMS Code 5900.21.83021, HDL Proj 23800, UNCLASSIFIED Report

A model of the ion-electron flow in the stagnation region between the detached shock and the wall of a Langmuir-type probe is proposed for ionized air in a shock tube at ion mass fractions less than 10^{-4}. The probe consists of a collecting electrode located at the stagnation point of an axially symmetric blunt body. Based on the close agreement between numerical calculations and measurements of the probe wall ion current density, the proposed model gives an accurate description of the ion-electron flow in the stagnation point boundary layer for negative electrode potentials. The procedure is also indicated to be applicable in the stagnation region between the detached probe shock and the edge of the boundary layer. However, the ion and the electron number densities in the undisturbed incident flow ahead of the detached shock cannot be obtained unless it is possible to calculate the changes in the number densities across the shock.

Theory of Langmuir probes in shock tubes

Ion-electron measurements in shock tubes

Blunt body ion-electron distribution

REMOVAL OF EACH CARD WILL BE NOTED ON INSIDE BACK COVER, AND REMOVED CARDS WILL BE TREATED AS REQUIRED BY THEIR SECURITY CLASSIFICATION.